UNIONE EUROPEA
Fondo Sociale Europeo

Ministero dell'Università e della Ricerca

PON RICERCA E INNOVAZIONE 2014 - 2020

UNIVERSITÀ DEGLI STUDI FIRENZE
Da un secolo, oltre.

DOTTORATO DI RICERCA IN
Ingegneria Industriale

CICLO XXXVII - PON ex DM1061

Modellazione Multifisica CFD di Elettrolizzatori Alcalini: dallo Sviluppo Numerico ad Applicazioni Industriali

Multi-physics CFD Modeling of Alkaline Electrolyzers: from Numerical Development to Industrial Applications

Settore Scientifico Disciplinare
IIND-06/B

Dottorando
Dott. Marco Dreoni[1]

Supervisori
Prof. Alessandro Bianchini[1]
Dott. Francesco Balduzzi[1]
Ing. Francesco Maria Ferro[2]
Dott. Matthias Neben[3]

Coordinatore
Prof. Giovanni Ferrara[1]

Anni 2022/2024

[1] Dipartimento di Ingegneria Industriale, Università degli Studi di Firenze, Via di Santa Marta 3, 50139, Firenze, Italia
[2] McPhy Energy Italia Srl, Via Ayrton Senna 22, 56028, San Miniato, Italia
[3] McPhy Energy Deutschland GmbH, Schwartzkopffstraße 1, 15745 Wildau, Germania

UNIVERSITÀ
DEGLI STUDI
FIRENZE

PhD in
Industrial Engineering

CYCLE XXXVII

Multi-physics CFD Modeling of Alkaline Electrolyzers: from Numerical Development to Industrial Applications

Academic Discipline (SSD) IIND-06/B

Doctoral Candidate

Dr. Marco Dreoni

Supervisors

Prof. Alessandro Bianchini
Dr. Francesco Balduzzi
Ing. Francesco Maria Ferro
Dr. Matthias Neben

Coordinator
Prof. Giovanni Ferrara

Years 2022/2024

“l'eau décomposée en ses éléments constitutifs, (…) et décomposée, sans doute, par l'électricité, qui sera devenue alors une force puissante et maniable, car toutes les grandes découvertes, par une loi inexplicable, semblent concorder et se compléter au même moment. Oui, mes amis, je crois que l'eau sera un jour employée comme combustible, que l'hydrogène et l'oxygène, qui la constituent, utilisés isolément ou simultanément, fourniront une source de chaleur et de lumière inépuisables et d'une intensité que la houille ne saurait avoir. Un jour, les soutes des steamers et les tenders des locomotives, au lieu de charbon, seront chargés de ces deux gaz comprimés, qui brûleront dans les foyers avec une énorme puissance calorifique. Ainsi donc, rien à craindre. Tant que cette terre sera habitée, elle fournira aux besoins de ses habitants, et ils ne manqueront jamais ni de lumière ni de chaleur, pas plus qu'ils ne manqueront des productions des règnes végétal, minéral ou animal. Je crois donc que lorsque les gisements de houille seront épuisés, on chauffera et on se chauffera avec de l'eau. L'eau est le charbon de l'avenir.”

Jules Verne, “L'Île mystérieuse”

"the water decomposed into its constituent elements, (…) and decomposed, no doubt, by electricity, which will then have become a powerful and manageable force, for all the great discoveries, by an inexplicable law, seem to coincide and complement each other at the same time. Yes, my friends, I believe that water will one day be used as fuel, that hydrogen and oxygen, which constitute it, used separately or simultaneously, will provide an inexhaustible source of heat and light, with an intensity that coal could not have. One day, the holds of steamers and the tenders of locomotives, instead of coal, will be loaded with these two compressed gases, which will burn in the furnaces with enormous calorific power. So, nothing to fear. As long as this earth is inhabited, it will provide for the needs of its inhabitants, and they will never lack light or heat, any more than they will lack the products of the plant, mineral, or animal kingdoms. I therefore believe that when the coal deposits are exhausted, we will heat and warm ourselves with water. Water is the coal of the future."

Jules Verne's "The Mysterious Island"

Alla mia famiglia
Alle comunità che hanno la forza di rendere il mondo migliore

DECLARATION

I hereby declare that this submission is my own work and, to the best of my knowledge and belief, it contains no material previously published or written by another person, nor material which to a substantial extent has been accepted for the award of any other degree or diploma at University of Florence or any other educational institution, except where due references are provided in the thesis itself.

Any contribution made to the research by others, with whom I have been working at the University of Florence or elsewhere, is explicitly acknowledged in the thesis.

Marco Dreoni
31/12/2024

ACKNOWLEDGEMENTS

Ringrazio sinceramente quanti mi hanno sostenuto in questi ultimi 3 anni.

Ho avuto a mio fianco delle persone e dei maestri che, ciascuno nel proprio campo specifico e con le proprie modalità, mi hanno aiutato a portare avanti questo progetto.

Mi sento di ringraziare per primo il mio tutor, maestro e amico, Francesco Balduzzi, senza il quale difficilmente avrei potuto raggiungere i livelli di simulazione del lavoro presente. Un sensei per la CFD che è la matematica e la struttura su cui si basa il progetto di ricerca di questa tesi. Ho apprezzato tantissimo le tue modalità di accompagnamento come tutor nel mio percorso. Nel lasciarmi la libertà creativa di fare tentativi e di organizzare il lavoro. Ma soprattutto, Baldu, sei stato per me un grande amico, a cui non posso che augurare il meglio da ogni punto di vista, di carriera e personale. Grazie.

Grazie ad Ale e Giowe, ovvero i professori Bianchini e Ferrara: anche per voi nutro il massimo rispetto per la gestione di tutto il gruppo di ricerca pur mantenendo un clima informale e rilassato. Mi auguro in futuro di trovare dei capi al vostro livello, da tutti i punti di vista. Avete formato un gruppo di dottorandi e ricercatori che sono in primis un gruppo di amici, con i quali conversare e passare un bellissimo tempo insieme. Grazie a Luchino. Mi hai fatto sentire a casa al Linea, covo di sperimentali, lontani dal mio essere numerico. Il tuo cuore grande si percepisce in ogni dialogo. Grazie per le giornate di sci insieme. Grazie ai miei tutor aziendali di McPhy, sia dalla parte di Wildau che dalla parte di San Miniato e grazie a tutti i colleghi di tali sedi. In particolare, grazie a Francesco Ferro, Matthias, Sahil, Kevin ed Eleonora per il supporto nel lavoro.

Ringrazio Santa Marta e il laboratorio Linea, quali luoghi dove la cultura fiorisce.

Per la tesina di maturità ho portato la figura di Ulisse in Dante. Una figura che ha incoraggiato i propri compagni a superare i limiti umani, che, senza l'aiuto divino, è stata destinata al naufragio, che pur predicando l'importanza dei valori e della conoscenza ha deciso di intraprendere il proprio viaggio lasciando alle

spalle i propri cari. Qualunque sia il mio viaggio futuro, so che non sto lasciando indietro nessuno.

Sarò più breve da qui in avanti, “di quinci innanzi”, un po’ come Dante quando cerca di descrivere la visione di Dio, “così la neve al sol si disigilla”, e non ne abbiano a male tutti coloro che seguono.

Durante quei venerdì a pranzo da Aurelio, i lampredì, e durante le partite di ping pong del Linea, è stato forgiato tra noi un fortissimo legame. Quindi, grazie a tutti i colleghi REASE, in ordine di “apparizione e sparizione”, un grazie a Iacopo, al nipote di Stefano Bosi, a Ciampo, Paga, Sup, Ste, Pier, Popes, Omar, Rick (Prof. Fritto), Tubo, Albe, Cocks, Sandrino, Claretta, Andre, Crickets e Marco Tarchiani. Abbiamo passato dei bellissimi momenti insieme.

Venendo poi a ringraziamenti personali, sarò forse ancora più breve, in questa sede. Quindi, grazie ai miei genitori e a mia sorella che mi hanno sostenuto da vicino e da lontano. Grazie zia per i pranzi insieme. Grazie zio per i fumetti scaccia pensieri. Grazie a mia nonna per trasmettermi la tua forza e la tua indipendenza. Grazie ai miei nonni. Al “lascia scorrere” di nonno Enzo, consiglio personale che si contrappone al “pace e bene” che invece elargiva a tutti. Grazie ai miei amici storici e agli amici nuovi. Grazie a Giulia per essermi stata vicina all’inizio di questo percorso. Grazie ai gruppi di corsa, ballo, buddismo, WWF, che mi hanno concesso i momenti di piacere e di recupero delle energie mentali. Grazie a Floriane per essere stata la mia casa a Berlino. Meine Musikkultur wird nie mehr die gleiche sein, seit ich dich kennengelernt habe. Dein “Du kannst das, schaffst das und machst das”, dein “Los!” und mein “Forza!”. Unsere paar Berliner Kinld als Wegbier.

ABSTRACT

To date, the most industrially developed technology to produce green hydrogen is alkaline water electrolysis. Alkaline water electrolyzers are in fact suitable to cover the expected green hydrogen future demand, due to their maturity and low costs. For the necessary upscaling and large-scale production, it is however essential to have an optimized design of the cells. Cell performance is mainly linked to electrical and material characteristics, but, on the other hand, the evolution of gas bubbles on the electrodes contributes to ohmic resistance and is not always considered when designing the electrolyzer. Fluid-dynamics studies on this established technology have only started to come up in recent years, nevertheless it is still not evident how cell performance may be driven by flow characteristics. The requirements for CFD simulations are anyhow extremely challenging, since solving the gas bubbles' motion implies the solution of a two-phase flow characterized by very low Reynolds numbers and a high fraction of dispersed gas.

A clear definition of a CFD multi-physics model is also lacking in the literature, together with a deep understanding of the internal cell phenomena. Comprehensive models, accounting for different "physics", are needed to improve on design and efficiency of these devices and simulate how two-phase flow, electrochemistry and thermal behaviors mutually interact, allowing for geometry optimization and detection of critical areas, due to gas accumulation and hot spots. Furthermore, electrolyzer cells experimental setups are rare, making the validation of such models harder.

This PhD thesis tries to bridge such gaps proposing a multi-physics CFD model, of progressive complexity, validated towards a simplified electrochemical cell from the literature. The model is applied to two different industrial cells with different purposes: first, a cathodic half-cell of a zero-gap configuration electrolyzer is employed to present possible key performance metrics, for a more detailed fluid-dynamics optimization of the cell geometry; second, a complete traditional cell is modeled, accounting for the diaphragm characterization and thermal analysis, identifying critical areas of the geometry leading to gas accumulation or hot spots. Also, through tailored boundary

conditions, the simulation of any cell of the entire stack is made possible, without the computational costs associated with the full geometry.

Introduction of the gas through gas source better aligned with the experimental output, during validation. However, the minor gas dispersion found for the electrochemical case was considered valid, as operating conditions are much more different for real-case electrolyzers. So, electrochemical modeling was applied to the real-case cells, for more physical complexity and for the introduction of the bubble coverage effect. Sensitivity analyses showed how higher mass flow rates are generally linked to better bubble removal and increased performances. Finally, hot spots are mainly expected in areas of electrolyte stagnation, based on the thermal simulations results.

To sum up, the present thesis emphasizes the role of CFD as a key tool in advancing alkaline electrolyzers. It offers valuable insights into multi-physics phenomena and presents validated methodologies, serving as a foundation for enhancing electrolytic cells simulations and design. Therefore, the results contribute to academic knowledge while also tackling significant industrial challenges.

Keywords: CFD, alkaline water electrolyzers, numerical modeling, multi-physics, hydrogen

PROPOSITIONS

Motivation

- Building a comprehensive multi-physics CFD modeling of alkaline electrolyzers for geometry optimization and efficiency enhancement.

Original Contribution

- Definition of a CFD model able to account for two-phase flow, electrochemistry and thermal behaviors of electrolytic cells.
- Sound grid-independence study.
- A new current density definition linked to gas bubble coverage.
- Cell performance analysis from a fluid-dynamic point of view.

Open questions

- Assessing the effect of turbulent dispersion on bubbles and the impact of very large bubbles.
- Simulating transient conditions to analyze dynamic operational scenarios.
- Validating the model on a real electrolyzer cell experimental setup.

INDEX

LIST OF FIGURES

LIST OF TABLES

NOMENCLATURE

Acronyms

AEM	Anion Exchange Membrane
AWE	Alkaline Water Electrolyzer
CCUS	Carbon Capture Utilization and Storage
CFD	Computational Fluid Dynamics
CL	Catalyst Layer
DPM	Dispersed Phase Model
DRI	Direct Reduced Iron steel production
DVB	Divinylbenzene
EZ	Electrolyzer
GDL	Gas Diffusion Layer
IEA	International Energy Agency
IRENA	International Renewable Energy Agency
ISM	Ion Solvating Membrane
IPCC	Intergovernmental Panel on Climate Change
KPI	Key Performance Indicator
LHV	Lower Heating Value
LSCF	Lanthanum Strontium Cobalt Ferrite
LSM	Lanthanum Strontium Manganite
MEA	Membrane-Electrode Assembly
NNFC	No-Net-Flow Configuration
PBI	Polybenzimidazole
PEM	Proton Exchange Membrane
PEMFC	Proton Exchange Membrane Fuel Cell
PFSA	Perfluorosulfonic Acid
PIV	Particle Image Velocimetry
POBP	Polyoxindole Biphenylene
PPS	Polyphenylene Sulfide
RANS	Reynolds-Averaged Navier-Stokes

RSE	Reynolds Stress Equations
RSM	Reynolds Stress Model
SOEC	Solid Oxide Electrolyzer Cell
SST	Shear Stress Transport
STD	Standard turbulence model
UDS	User Defined Sources
USD	US Dollars
VF	Volume Fraction
VLB	Very Large Bubble
VOF	Volume Of Fluid
VPERGE	Vertical Plane Electrode Reactors with Gas Electrogeneration
YSZ	Yttria-Stabilized Zirconia

Greek symbols

$1/\alpha$	viscous resistance coefficient	[-]
α	volume fraction	[-]
β	constant of turbulent model	[-]
γ	charge transfer coefficient	[-]
Γ	velocity uniformity	[-]
ε	turbulent dissipation rate	[m^2/s^3]
ε_p	porosity	[-]
η	efficiency	[-]
η_F	faradaic efficiency	[-]
λ	thermal conductivity	[W/(m·K)]
μ	viscosity	[kg/(m·s)]
ρ	density	[kg/m^3]
σ	electrical conductivity	[S/m]
τ_r	relaxation time	[s]
$\overline{\overline{\phi}}_l$	Gibson and Launder coefficient	[-]
ϕ_k	constant of turbulent model	[-]
ϕ_ε	constant of turbulent model	[-]
ω	dissipation rate of turbulent kinetic energy	[1/s]
$\vec{\omega}$	angular velocity	[rad/s]
$\vec{\Omega}$	relative angular velocity gas-liquid	[rad/s]

Latin symbols

a, a_0, b	Davies correlation coefficients	[-]
A	electrode surface	[m^2]
A_f	solid phase surface	[m^2]
C_d	drag coefficient	[-]
C_{ij}	Forchheimer matrix	[-]
C_{lift}	lift coefficient	[-]
C_{vm}	virtual mass coefficient	[-]
C_{wl}	wall lubrication coefficient	[-]
C_ε	constant of turbulent model	[-]
C_μ	constant of turbulent model	[-]
C_ω	rotational drag coefficient	[-]
$C_{\omega 1,} C_{\omega 2}$	wall lubrication coefficients	[-]
C_2	inertial resistance coefficient	[-]
d_b	bubble diameter	[m]
d_{H2}	hydrogen mean bubble diameter	[µm]
d_{O2}	oxygen mean bubble diameter	[µm]
D_{ij}	Darcy matrix	[-]
$\overline{\overline{D}}$	strain tensor	[-]
e	specific internal energy	[J/kg]
e^-	electrons	[-]
F	Faraday constant	[A·s/mol]
$\vec{F}$	force	[N]
$\vec{F}_d$	drag force	[N]
$\vec{F}_{lift}$	lift force	[N]
$\vec{F}_{rot}$	rotational force	[N]
$\vec{F}_{td}$	turbulent dispersion force	[N]
$\vec{F}_{vm}$	virtual mass force	[N]
$\vec{F}_{wl}$	wall lubrication force	[N]
$\vec{g}$	gravitational acceleration	[m/ s^2]
G°	standard Gibbs free energy	[J/mol]
h	specific internal enthalpy	[J/kg]
H°	standard enthalpy of formation	[J/mol]
i	current density	[A/m^2]
i_0	exchange current density	[A/m^2]
i_1	maximum current density	[A/m^2]

I	current	[A]
I_g	gas bubble moment of inertia	[kg·m^2]
$\overline{\overline{I}}$	identity matrix	[-]
$\vec{J}$	diffusion flux	[J/(m^2·s)]
k	turbulent kinetic energy	[m^2/s^2]
K_g	turbulent dispersion coefficient	[-]
L	cell length	[m]
m	mass	[kg]
$\dot{m}$	mass flow or transfer between phases	[kg/s]
M	molecular mass	[kg/mol]
$\dot{M}$	mole flow	[kg/(mol·s)]
n	number of points	[-]
N	total number of chemical species	[-]
$\vec{n}_w$	unit vector perpendicular to the wall	[-]
p	pressure	[Pa]
p_{bar}	pressure in bar	[bar]
p_{gas}	partial pressure of gas	[Pa]
p_w	partial pressure of water	[Pa]
p_{w°	standard partial pressure of water	[Pa]
P_{heat}^{cell}	dissipated power	[W]
$\overline{\overline{P_l}}$	main shear production	[-]
R	ideal gas constant	[J/(mol·K)]
$\dot{R}$	volumetric rate of creation	[kg/(m^2·s)]
R^2	coefficient of determination	[-]
$\overline{\overline{R}}$	Reynolds stress tensor	[-]
R_b	bubble resistance	[ohm]
R_{circ}	circuit resistance	[ohm]
R_e	electrolyte resistance	[ohm]
R_{mem}	membrane resistance	[ohm]
Re	Reynolds number	[-]
S	mass source term	[kg/s]
$\dot{S}$	volumetric rate of creation (UDS)	[kg/(m^2·s)]
S°	standard entropy of formation	[J/mol·K]
S_F	Faraday energy	[W/m^3]
S_{gas}	volumetric source of gas	[kg/(m^3·s)]
S_h	heat source term	[W/m^3]
S_i	momentum equation source term	[Pa/m]

S_J	Joule energy	[W/m^3]
S_R	chemical reactions energy	[W/m^3]
S_ω	turbulent dissipation source term	[kg/(m^3·s^2)]
Sc	Schmidt number	[-]
t	time	[s]
T	temperature	[K]
T_b	bubbles-induced turbulence	[kg/(m·s^3)]
$\vec{T}$	torque	[N·m]
$\bar{\bar{T}}$	stress tensor	[-]
$\bar{u}$	average fluid velocity value	[m/s]
u_i	fluid velocity of ith point	[m/s]
U_{act}	activation overpotential	[V]
U_{cell}	cell potential	[V]
U_{conc}	concentration overpotential	[V]
U_{ohm}	ohmic overpotential	[V]
U_{rev}	cell reversible potential	[V]
U_{rev}°	cell standard reversible potential	[V]
U_{tn}	cell thermoneutral potential	[V]
U_{tn}°	cell standard thermoneutral potential	[V]
v'	stoichiometric coefficient of reactants	[-]
v''	stoichiometric coefficient of products	[-]
$\vec{v}$	velocity	[m/s]
$\overrightarrow{v'}$	turbulent fluctuation velocity	[m/s]
$\vec{v}_{dr}$	drift velocity	[m/s]
V	electric potential	[V]
V_{gas}	volume of gas	[m^3]
$\bar{V}_{rec}$	liquid recirculation	[-]
V_{tot}	total volume of the porous matrix	[m^3]
V_v	volume of voids	[m^3]
VF	volume fraction	[-]
x_0	initial position	[m]
Y_j	local mass fraction of jth species	[-]
z	electrons number	[-]
Z_j	charge number of the jth species	[-]

Subscripts

(aq)	aqueous state
(gas)	gasous state
a/c	anode/cathode
ave	average
g	gas phase
j	j^{th} chemical species
k	generic phase
l	liquid phase
m	mixture
max	maximum
min	minimum
out	outlet
r	r^{th} reaction
t	tangential
var	variable

Superscripts

T	transpose
$turb$	turbulent
$^\circ$	standard conditions
$*$	normalized

SYNOPSIS

The present thesis explores advanced computational fluid dynamics (CFD) modeling techniques to address complex simulations of alkaline electrolyzers. These devices are pivotal in sustainable hydrogen production, a cornerstone of renewable energy systems and industrial decarbonization efforts. The research spans model development, validation, and case studies, providing valuable insights into multiphase flow dynamics, electrochemical reactions, and thermal effects modeling methods for electrolyzers under various configurations and operating conditions.

Hydrogen, recognized as a clean and versatile energy carrier, plays an essential role in mitigating greenhouse gas emissions and facilitating the energy transition. However, the high costs and energy demands associated with water electrolysis present significant challenges. Today, alkaline water electrolyzers (AWEs) are the most mature and cost-effective technology for industrial-scale hydrogen production and their advancement relies on improving efficiency, durability, and scalability.

This thesis focuses on building a complex multi-physics CFD model to optimize cell geometries, enhance gas bubble management, integrating electrochemical and thermal physics to the two-phase simulation approach. Bridging gaps in existing literature, particularly regarding fluid-dynamics models in electrolytic cells, it aims to advance modeling methodologies while providing practical recommendations for industrial-scale applications. In fact, despite being alkaline electrolyzers a mature device on the market, their thorough study through CFD is only coming up in recent years. To understand the phenomena involved inside the cell, such a modeling framework is pivotal. On the other hand, a limit to CFD modeling is the almost total absence of experimental results for validation purposes.

Using ANSYS Fluent software environment, the available two-phase models and sub-models are evaluated on the specific case studies. Furthermore, systematic grid sensitivity analyses are conducted, based on a novel approach to define the mesh layer at the electrode, ensuring numerical accuracy and stability.

The thesis investigates three distinct cases:

- Literature test-case: a simplified model of a lab-scale cell from the literature [1] with low current density and ambient conditions to validate the numerical framework against experimental data.
- Zero-gap cathodic half-cell: taken from a 1 MW industrial-scale electrolyzer, with focus on optimizing geometry and enhancing hydrogen production efficiency.
- Traditional cell: a full-geometry cell from a traditional 50-kW alkaline electrolyzer with a semi-permeable diaphragm to analyze mutual thermal, electrochemical and fluid dynamic effects across different cells of the stack.

Each case study is tailored to address specific research questions, such as bubble dynamics, current density variations, and the impact of geometry on performance indicators like gas accumulation and velocity profiles.

After detailing the literature methodology for simulating alkaline cells, the modeling options available in Fluent software are assessed through a precise sensitivity analysis. Among the available multiphase models, the Eulerian model is chosen for its higher accuracy and suitability for simulating a two-phase flow where the gaseous phase is highly dispersed in the liquid phase, outperforming alternatives like the Volume of Fluid (VOF) model. After selecting the mathematical structure of the model, parameters such as interphase forces, gas introduction methods, and bubble size are evaluated. This initial sensitivity analysis is compared to the test-case cell from the literature, where the experimental setup and PIV output enabled the authors to have an idea of bubble behavior and size, and the velocity field inside the cell. Thanks to this study, the CFD framework developed for the present research could be validated. Flow visualization obtained during the experiments by Hreiz *et al.* [1] revealed that bubble curtains spread laterally as they moved upward, with bubble coalescence occurring near the electrodes both before and after detachment. Some bubbles, adhering to the electrodes, grew into Very Large Bubbles (VLBs).

To conduct the grid independence test for the meshing phase, a novel expression for the minimum necessary first layer thickness at the electrode is developed. In fact, a trade-off between the bubble diameter and the gas production layer has to be considered to ensure stable and physically meaningful simulations.

Using this case study as a reference, the initial approach focuses on introducing gas through a volumetric source at the electrodes. After defining the fluid dynamics model, the impacts of different source layer thicknesses and

bubble diameters are analyzed. A source layer approximately four times the bubble diameter provides the best agreement with experimental results. Moreover, the bubble size observed in experiments shows the best match with the velocity field contours, affirming the model's accuracy.

The authors attribute any discrepancies from the experimental case to two specific phenomena. First, the experiments reveal the presence of large bubbles, which locally introduce turbulence and enhance gas dispersion in the cell. Such large bubbles are not considered in the model and this can be a first source of discrepancy between the CFD and the experimental results. Second, the flow is assumed to be laminar due to its low velocity, excluding bubble dispersion caused by turbulence. However, for real electrolyzer cell applications with higher current densities, it is expected that bubbles will be significantly smaller, and coalescence and breakup phenomena less pronounced.

An alternative method of introducing gas via mass flow inlet at the electrode, as used in some literature studies, is also evaluated but produces higher velocity values, inconsistent with experimental observations. Finally, a third approach is introduced to enhance the physical complexity of the model, i.e. the use of Fluent electrochemical module, allowing to introduce the gas as a direct effect of the electrochemical reactions. Electrochemistry is incorporated by applying hydrogen and oxygen evolution reactions at the electrodes and imposing a current density as a wall boundary condition. Initially, this current density is assumed to be constant for simplicity.

The three gas introduction methods are validated against the experimental case taken from the literature [1]. More specifically, the gas velocity field obtained by Hreiz *et al.* thanks to a PIV methodology can be compared with the CFD results. The volumetric source method proves the most faithful, likely due to its greater gas dispersion compared to direct gas introduction at the wall. However, the electrochemical-driven gas introduction, being more physically complex and comprehensive, is chosen for application to the real cell geometries. Furthermore, for the electrolyzer cells greater gas dispersion is expected since the fluid already possesses intrinsic velocity, unlike the validation case where the velocity is solely due to gas buoyancy at the electrode.

The first step toward real electrolyzer cells involves applying the model to a quasi-2D geometry (2.5D), representing a rectangular sector of the cell with real operating conditions. Specifically, the model is applied to the cathodic half-cell sector of a McLyzer 200-30 electrolyzer. The aim is not to capture the exact cell behavior but to perform a sensitivity analysis on parameters like gas volume fraction within the cell and at the outlet, under varying current density and electrolyte mass flow rates. It is observed that higher mass flow rates reduce gas

volume fraction and gas accumulation. In particular, when the mass flow rate is doubled, the average outlet gas volume fraction decreases by approximately 40%, while halving the mass flow rate increases it by 60%. while higher current densities increased gas volume fraction. Conversely, when hydrogen production is lower, gas tends to remain closer to the electrode without diffusing throughout the cell. Higher current densities allow for a greater potential for the gas to disperse within the cell, mixing with the electrolyte farther from the electrode.

The main flow variables, including gas volume fraction and velocity, are analyzed at different cell heights. Additionally, the model is refined by making the wall current density a variable dependent on the local gas volume fraction, instead of assuming it to be constant. This adjustment accounted for the "bubble coverage" phenomenon, where areas with higher gas volumes exhibit higher local potential and lower local current density, reducing gas production. As expected, the model reveals greater gas production and velocity at the bottom of the cell compared to the top due to gas accumulation and buoyancy effects. For instance, constant current density simulations show a 20% higher gas volume fraction and 10% higher vertical gas velocity in the lower quarter of the cell, compared to variable current density simulations.

The next step involves applying the model to a real cathodic half-cell geometry. This includes the first attempt at optimizing cell design based on the developed model. For instance, it is observed that the gas collector causes significant gas accumulation in the upper part of the cell. Different geometric configurations are evaluated to identify the most efficient design. Fluid dynamic parameters are introduced to assess cell performance, considering both gas accumulation and flow uniformity. It is concluded that, while each parameter highlights different aspects of cell performance, some parameters, such as the average volume fraction at the electrode, are more critical in zero-gap designs than overall gas accumulation. This analysis identifies an optimal cell geometry, namely the one with the gas collector but without flow obstacles. Further sensitivity analyses are conducted by varying current density and inlet electrolyte flow rates, revealing that higher volume fraction values correlate with increased current densities but are less affected by electrolyte mass flow rate. At higher current densities, increased mass flow rates help manage gas volume inside the cell, mitigating gas accumulation. To avoid hot spots higher mass flow rates are advised. Flow uniformity improves with greater mass flow rates but declines at higher current densities. Finally, flow recirculation intensifies with lower mass flow rates and higher current densities. The findings align with studies from the literature.

Finally, the thermal cell behavior is added to the model to increase its physical complexity. The heat generated by chemical reactions and charge transfer resistances is included. More specifically, Faradaic, Joule and reaction heating are included in the model via User Defined Sources (UDS), directly linking electrochemical variables such as current density and overpotential to the thermal behaviour of the cell. This extended model is applied to a complete traditional electrolyzer cell, namely a PIEL H15. For the first time, both the anode and cathode are modeled, along with the diaphragm separating the cells. Including the diaphragm in the geometry enhances the flow recirculation, improving mixing and reducing thermal gradients for a more uniform temperature distribution. The cathode consistently shows higher gas volume fractions than the anode, attributed to the distinct densities of hydrogen and oxygen. Different behaviors at the anode are considered influenced by flow channeling, due to fluid-dynamic patterns in the lower cell regions.

By implementing appropriate boundary conditions, it becomes possible to simulate the behavior of three cells in the stack (the first, central, and last) without modeling the entire stack, thus avoiding high computational costs.

The thermal model analysis identifies hotspots within the cell proposing an optimized design to address a region prone to hazardous gas accumulation.

Simulations of the first, central, and last cells of the stack demonstrate significant differences in gas volume fractions and thermal behavior. Velocity non-uniformities in the half-cells indicate that slower flows are generally linked to higher temperatures. Hot spots, especially in areas of electrolyte stagnation, were more pronounced. Simulations under start-up conditions show an average reduction of 3 K at the anode and 1.5 K at the cathode compared to operating conditions.

The research provides a robust framework for understanding the interplay between fluid dynamics, electrochemistry, and heat transfer in alkaline electrolyzers. By tailoring modeling approaches to specific operational conditions, the study offers practical insights for optimizing electrolyzer designs. Key contributions include:

- A validated CFD approach incorporating a novel current density formulation, two-phase flow and thermal effects inside the cell.
- Recommendations for key performance parameters, to be studied to enhance the cell design and hydrogen production efficiency.

While the thesis successfully bridges several knowledge gaps, challenges remain, particularly in capturing turbulence effects and validating models against high-pressure operational data. Future research could explore:

- Advanced turbulence models to simulate bubble-induced flows more accurately.
- Assessing the impact of very large bubbles on the flow field.
- The integration of transient simulations to analyze dynamic operational scenarios.
- Collaborative studies combining experimental and numerical approaches to validate findings under diverse conditions.

This thesis highlights the potential of CFD as a pivotal tool for the advancement of alkaline electrolyzers. By providing insights into multi-physics phenomena and offering validated methodologies, it lays the groundwork for improving hydrogen production technologies.

INTRODUCTION

This thesis delves into advanced computational fluid dynamics (CFD) modeling techniques to address the complex challenges associated with simulating alkaline electrolyzers. These devices are critical for sustainable hydrogen production, a key element in renewable energy systems and industrial decarbonization initiatives.

The research focuses on developing a CFD model to optimize cell geometries, improve gas bubble management, and incorporate electrochemical and thermal interactions for more comprehensive multi-physics simulations. By bridging gaps in the current literature, this study aims to enhance simulation methodologies and provide practical insights for industrial applications and cell design optimization.

The thesis is structured as follows:

- Chapter 1 presents the background, motivation and literature review of the research. In particular, description of alkaline electrolyzers characteristics and geometry is provided. The literature review mainly explores the state-of-the-art of CFD approach when dealing with electrolyzers numerical simulation.
- Chapter 2 gives an overview of the physical and numerical theory involved in the modeling of electrolyzers, presenting the two-phase flow, porous, electrochemical and thermal models.
- Chapter 3 details the numerical choices and the methodology employed for the CFD multi-physics simulation.
- Chapter 4 provides an overview of the case-study cells and electrolyzers considered for the model validation and application.
- Chapter 5 reports the results of the initial model application to a lab-scale cell from the literature for validation purposes and sensitivity analyses on the modeling setup.

- Chapter 6 presents the outcomes of the model application to a quasi-2D sector of a cathodic cell from a 1-MW industrial-scale electrolyzer, for sensitivity analyses concerning current density and mass flow variations.
- Chapter 7 provides the findings of the model usage on the real-geometry cathodic cell from the 1-MW electrolyzer of Chapter 6, aiming at geometry optimization and performance assessment.
- Chapter 8 deals with the full model application to a complete geometry cell, anode-to-cathode including the diaphragm, from a 50-kW electrolyzer. The main results are presented in terms of gas volume fraction, fluid velocity and cell temperatures.
- Finally, a last chapter recaps the conclusions of the PhD research and findings.

1 ALKALINE ELECTROLYZERS: FUNDAMENTALS AND MODELING

1.1 Present and future energy challenges

One of the pressing challenges of the 21st century is tackling climate change, with the scientific consensus attributing its primary drivers to human activities. Never before in history has a species been capable of altering the planet's climate. Humans are achieving this by releasing ever-increasing amounts of greenhouse gases into the atmosphere.

As early as the late 19th century, Svante Arrhenius calculated the effects on the Earth's average surface temperature of the CO_2 amount in the atmosphere, increasing the evidence over the greenhouse effect. This is a natural phenomenon where specific gases trap infrared radiation, maintaining Earth's climate conditions that support life [2]. However, since the industrial revolution, humans have been emitting these gases in excess, transforming this natural beneficial process into a driver of global warming.

Rising global temperatures are leading to an increased frequency of severe phenomena such as floods, droughts, and geological instability, leading to mass migrations caused by flooded or uninhabitable regions. This has spurred political action, though current efforts remain inadequate. International organizations are issuing warnings and proposing solutions: the Intergovernmental Panel on Climate Change (IPCC) underscores the urgency of achieving net-zero greenhouse gas emissions by mid-century to limit global warming to below 3°C above pre-industrial levels. In 2015, 196 parties signed the Paris Agreement, which aims to limit global warming to below 2°C, with an ideal target of 1.5°C, compared to pre-industrial levels. In the years that followed, many countries set

targets to achieve carbon neutrality between 2030 and 2070, with 2050 being the most common and frequently announced goal across 69 countries [3].

To achieve these goals, societies need to transition from the current fossil-fuel-dominated energy system to renewable-energy based economies, as fossil fuels emit significant amounts of carbon dioxide (CO_2), a greenhouse gas, during combustion.

1.2 Why is green hydrogen necessary?

Renewable energy sources have however some drawbacks: they are inherently intermittent due to their reliance on weather conditions, causing imbalances between energy supply and demand and potential grid instability. Energy load predictions are essential to meet daily demands in both civil and industrial sectors, ensuring all energy-intensive activities are covered. Currently, base loads are primarily supported by large-scale thermoelectric plants powered by fossil fuels, particularly natural gas, and by nuclear fission. For renewables to cover base loads, surplus installation is required, leading to periods of excess energy production and need for energy storage mechanisms [4], [5]. This is where hydrogen emerges as an energy carrier, which means that its potential role has similarities with that of electricity. Both hydrogen and electricity can be produced by various energy sources and technologies. Both are versatile and can be used in many different applications. No greenhouse gases, particulates, sulphur oxides or ground level ozone are produced from the use of either hydrogen or electricity. If the hydrogen is used in a fuel cell, it emits nothing but water. However, both hydrogen and electricity can have a high CO_2 intensity upstream if produced from fossil fuels such as coal, oil or natural gas. This disadvantage can only be overcome by using renewables or nuclear as the initial energy input, or equipping fossil fuel plants with Carbon Capture, Utilization, and Storage (CCUS) [6]. The crucial difference between hydrogen and electricity is that hydrogen is a chemical energy carrier, composed of molecules and not only of electrons. This distinction underpins all the reasons why hydrogen might outcompete electricity in some situations (and vice versa). Chemical energy is attractive because it can be stored and transported in a stable way, as is done today with oil, coal, biomass and natural gas. Molecules can be stored for long periods, transported across the sea in ships, burned to produce high temperatures, and used in existing infrastructure and business models designed around fossil fuels. Because of its molecular nature, hydrogen can also be combined with other elements such as carbon and nitrogen to make hydrogen-

based fuels, the so-called liquid organic hydrogen carriers [7], that are easier to handle, and can be used as feedstock in industry, helping to reduce emissions.

Therefore, hydrogen represents a potential energy storage mechanism, either compressed in tanks, or liquid, or absorbed in the form of metal hydrides, complementing batteries and other storage systems. It offers advantages such as high specific energy and quick charging process, with lifetimes of 20 years for compressed hydrogen storage, longer than most of the batteries, and efficiencies between 90 and 95 % [8].

A drawback of hydrogen storage system is its limited round-trip efficiency. Unlike battery storage systems, which directly convert electrical energy into chemical energy during charging and reverse the process during discharging, hydrogen storage systems require additional devices for energy conversion. First, to produce green hydrogen (obtained via renewable-powered electrolysis), an electrolyzer (EZ) is necessary. For alkaline EZs, efficiencies range from 55% to 73% [9]. Once hydrogen is stored in a tank, another device, such as a polymer electrolyte membrane fuel cell (PEMFC), whose efficiency is approximately 46.5% [8], is needed to convert it back into electrical energy. Considering the entire process (production, storage, and conversion back to electricity), and accounting for storage losses, the overall efficiency ranges between 20% and 33%. In contrast, battery storage systems achieve round-trip efficiencies between 60% and 95%, making them 2 to 4.75 times more efficient than hydrogen systems, even when storage losses are excluded [8].

However, beyond its future potential in the energy sector, hydrogen is already produced in large quantities for industrial purposes. It is primarily employed in refineries and chemical industries for ammonia production and fertilizers, with a smaller share used in transportation, such as fuel for buses. Demand for hydrogen, which has grown more than threefold since 1975, continues to rise (Figure 1.1). In the chart of Figure 1.1 “Refining”, “Ammonia” and “Other pure” represent demand for specific applications that require hydrogen with only small levels of additives or contaminants tolerated. “Methanol”, “DRI” (Direct Reduced Iron steel production) and “Other mixed” represent demand for applications that use hydrogen as part of a mixture of gases, such as synthesis gas, for fuel or feedstock. Nearly all of the hydrogen is produced from fossil fuels, relying on steam reforming for around 96% of its production [10]. As a result, according to the International Energy Agency (IEA), current hydrogen production emits between 1.1 and 1.3 gigatons (Gt) of CO_2 annually, including upstream and midstream emissions from fossil fuel supply [11]. In 2022, global energy-related greenhouse gas emissions reached 41.3 Gt

of CO_2 equivalent [11]. Therefore, hydrogen production accounts for approximately 3% of global energy-related greenhouse gas emissions.

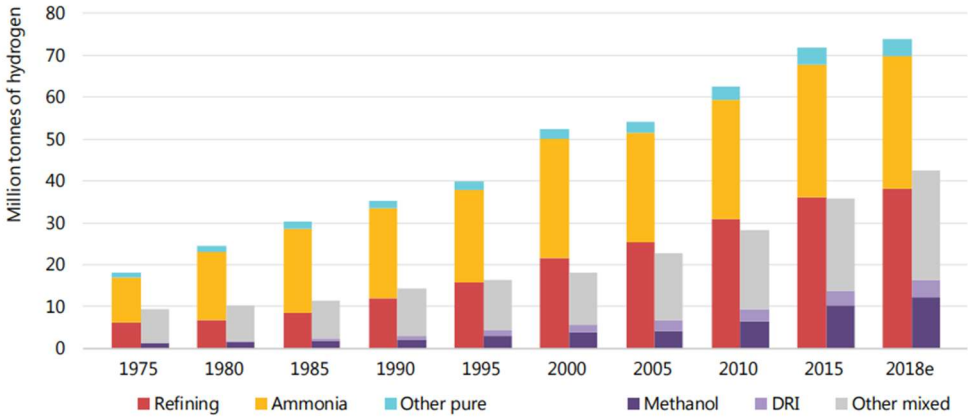

Figure 1.1: Global annual demand of hydrogen since 1975 [10]

Electrifying hydrogen production could significantly reduce these emissions. Other than that, hydrogen could enable less impactful steel production, contributing to the decarbonization of "hard-to-abate" sectors where electrification alone is insufficient. By 2030, the total installed electrolyzer capacity is projected to reach around 200 GW, assuming all current projects are completed [12]. However, this capacity is still well below the 860 GW needed by 2030 to align with a trajectory that would enable achieving net-zero emissions by 2050 [13]. The International Energy Agency (IEA) anticipates that electrolyzer capacity will need to expand to 3,600 GW by 2050 [13].

Today, the primary barrier for hydrogen production via electrolysis to gain prominence is cost, as hydrogen produced via steam reforming remains significantly cheaper, between 1 and 6 $/kg$H_2$, than hydrogen from renewable-sources electrolysis, 4-12 $/kg$H_2$ [14]. However, significant cost reductions for electrolytic hydrogen are expected if such devices become more used. The International Renewable Energy Agency (IRENA) projects that cost reductions of up to 60% could be achieved by 2030 through a combination of manufacturing scale, learning rates, technological improvements, and increased module size, following a similar trend to the price reduction of photovoltaic systems [15].

1.3 Hydrogen production through electrolysis

Hydrogen can be produced using various methods, such as using algae [16], biomass gasification [17], photocatalytic and photoelectrochemical water splitting [18], or thermochemical cycles with solar furnaces and metal/metal oxide cycles [19] [20]. However, the most promising method that aligns with the fluctuating production of renewable energy on a megawatt to gigawatt scale remains water electrolysis [21].

The concept of electrochemical water decomposition in an electrolysis cell has been known for over 230 years. The first hydrogen production via electricity was demonstrated in 1789 by van Troostwijk and Deiman, who used an electrostatic generator as a direct current source. Shortly after Volta's invention of the voltaic pile in 1800, Carlisle and Nicholson utilized this device to split water into hydrogen and oxygen. That same year, Ritter conducted similar experiments in Jena, Germany, while Cruickshank used a voltaic pile to electrochemically decompose NaCl into hydrogen and chlorine in the early 19th century [22]. Throughout the 20th century, various commercial alkaline electrolyzers were developed to produce hydrogen for ammonia fertilizers using low-cost hydroelectricity. However, as the 20th century progressed, the cost-effective production of hydrogen through steam methane reforming increasingly replaced water electrolysis, limiting its use to niche applications by the century's end. In the late 1960s, General Electric pioneered proton exchange membrane (PEM) electrolysis using a solid acidic fluorinated ionomer electrolyte. Due to high material costs, PEM technology initially found applications only in laboratories, military, and space programs. Around the same time, high-temperature electrolysis using solid oxide cells was explored by General Electric and Brookhaven National Laboratory. Despite technical advancements, membrane and solid oxide electrolysis technologies failed to achieve commercialization during this period. Renewed interest in water electrolysis emerged in the 1990s, driven by its potential as a green energy carrier for renewable energy sources like wind and solar power and as a fuel source for hydrogen-powered fuel cells, particularly in automotive applications.

Currently, the main kinds of EZs industrially available are alkaline water electrolyzers (AWEs) and proton exchange membrane (PEMs), while solid oxides alkaline electrolyzers (SOECs) and anion exchange membrane (AEM) technologies are still in R&D phase. Table 1.1 and

Table 1.2 presents the main characteristics and materials of the above-mentioned electrolyzers.

Table 1.1: Comparison of the available water electrolyzer technologies (PEM e AWE from [9], SOEC from [21], AEM from [23], with specifications from [24], [25], [26])

Specification	AWE	PEM	SOEC	AEM
Technology maturity	Mature	Commercial	R&D	R&D
Temperature, °C	60-80	50-80	900-1000	40-60
Pressure, bar	1-200	1-50	<30	<35
Current density, A/cm^2	0.2-0.7	0.6-2.0	0.3-1.0	0.2-2
Cell potential, V	1.5-2.6	1.4-2.3	0.95–1.3	1.8–2.2 [24]
Cell voltage efficiency, %	58-77	57-83	81-86	39.7 [24]
Stack energy consumption, kWh$_e$/Nm$^3_{H2}$	3.8-4.4	4.53-7.3	2.5-3.5	4.8-5.2 [24]
System efficiency, %	55-73	55-75	65-70 [26]	80-90 [26]
Hydrogen production per stack, Nm^3/h	1.5-3880	0.22-5000	<10	0.25-1 [24]
Stack lifetime, hours	<90,000	<60,000	<20,000	<5,000
Load variation, %	15-100	0-100	-	5-100
Gas purity, %	99.999	99.999	99.9 [25]	99.9-99.9999

Table 1.2: Materials for the four types of electrolyzers (from [26]).

Component	AWE	PEM	SOEC	AEM
Electrolyte	Liquid: NaOH/KOH 20-30 wt%	Solid: PFSA membranes	Solid: Yttria-stabilized Zirconia (YSZ)	Solid: DVB polymer support with KOH or $NaHCO_3$
Separator	ZrO_2 stabilized with PPS mesh	Solid electrolyte (above)	Solid electrolyte (above)	Solid electrolyte (above)
Anode/ catalyst	Nickel coated perforated stainless steel	Iridium oxide	Perovskite-type (e.g. LSCF, LSM)	High surface area Nickel or NiFeCo alloys
Cathode/ catalyst	Nickel coated perforated stainless steel	Platinum nanoparticles on carbon black	Ni/YSZ	High surface area Nickel

Among the four types of electrolyzers described above, AWEs are mature, cost-effective technologies, particularly promising for large-scale green hydrogen production. With installation costs ranging from 500 to 1000 USD/kW ([27], [28]) and the ability to absorb fluctuating outputs from renewable energy, AWEs are well-suited for dynamic operations. Advances in AWE technology mainly focus on the catalyst material and on the membrane material [23], with anion exchange membranes (AEMs) and ion solvating membranes (ISMs) being at research and development stage but expected to represent the future trend for alkaline water electrolyzers ([29], [30], [23], [31]). In particular, ISMs are an emerging alternative to traditional AEMs in alkaline EZs. Unlike AEMs, which typically rely on ion-exchange side chains to conduct anions (OH^-), ISMs operate by being imbibed with an aqueous alkaline electrolyte, such as KOH, and have shown promise in terms of higher conductivity and stability in harsh alkaline environments. Recent developments in ISMs, including the use of materials such as polybenzimidazole (PBI) and polyoxindole biphenylene (POBP), have led to membranes that can endure high pH and extended operational durations [30].

1.4 Alkaline water electrolyzers (AWEs)

Alkaline water electrolyzers are the most mature type of industrial EZs in use today. Such technology is known for its reliability, maturity, and cost-effectiveness. The main components of this device, namely electrolyte, electrodes and diaphragm, are discussed in the following subsections.

1.4.1 The electrolyte

The most commonly used electrolyte for alkaline water electrolysis is an aqueous potassium hydroxide (KOH) solution containing 20-30% by weight of KOH [32]. At these concentrations, the specific conductivity is optimal within the operating temperature range of 50-80 °C. A more cost-effective alternative would be a diluted sodium hydroxide (NaOH) solution, which has however a lower conductivity: at a temperature of 50 °C, KOH provides a specific conductivity of approximately 95 S/m, whereas NaOH reaches a value of around 65 S/m [32]. Another factor to consider is the solubility of the gases produced within the electrolyte, as it impacts the purity of the resulting gas product. In general, gas solubility decreases with increasing electrolyte concentration due to the salting-out effect. In general terms, salting out is the phenomenon observed when the solubility of a non-electrolyte compound in water decreases

with an increase in the concentration of a salt [33]. NaOH exhibits a slightly greater salting-out effect compared to KOH. As a result, gas solubility is higher in a KOH solution.

1.4.2 The electrodes

Electrochemical reactions occur at the interface between the electrode surface and the electrolyte. At the cathode, hydrogen molecules are formed and accumulate on the electrode surface until a bubble detaches, following hydrogen evolution reaction of Eq. 1.1. At the anode, hydroxyl ions release their electrons and react to form water and oxygen, following oxygen evolution reaction of Eq. 1.2. Oxygen molecules accumulate in gas bubbles and rise along the anodic surface.

Cathode: $$2H_2O_{\ (l)} + 2e^- \rightarrow H_{2\ (g)} + 2OH^-_{\ (aq)} \quad 1.1$$

Anode: $$2OH^-_{\ (aq)} \rightarrow \tfrac{1}{2}O_{2\ (g)} + H_2O_{\ (l)} + 2e^- \quad 1.2$$

The electrode surface, along with the catalyst, plays a crucial role in interacting with water, reaction intermediates, and the molecular hydrogen and oxygen formed. As a result, electrode reactions are significantly influenced by the physical and chemical properties of their surfaces.

Electrodes must be electrically conductive to enable electron exchange with water or hydroxyl ions. They need a large interface area between the catalyst and the electrolyte and should provide suitable sites for gas bubble nucleation while facilitating bubble detachment.

The anode and cathode materials in these systems are typically made from nickel-plated steel and steel, respectively. Large surface areas are achieved using sintered structures, finned bodies, screens, perforated plates, or flat plates with electro-roughened surfaces. In alkaline cells, nickel is the most commonly used catalyst. Instead of solid nickel electrodes, nickel-plated mild steel is often employed [26].

1.4.3 The diaphragm

The electrodes in alkaline electrolyzers are separated by a thin porous sheet, commonly referred to as a diaphragm or separator, which is permeable to the

solution. This diaphragm is not electronically conductive, preventing electrical short circuits between the electrodes and allowing minimal distances between them. Ionic conductivity is facilitated by the alkaline aqueous solution that penetrates the diaphragm's pores [23].

The diaphragm's primary function is to prevent the mixing of hydrogen and oxygen gases produced at the cathode and anode, respectively. Additionally, the separator material must resist corrosion by the electrolyte in the presence of hydrogen or oxygen gases and remain structurally stable throughout the cell's operational life to prevent its pores from collapsing.

To minimize the cell's ionic resistance, the separator is made as a thin sheet, with its thickness determined by mechanical strength and gas passage constraints. Historically, asbestos was commonly used as a separator material in alkaline cells due to its effective gas separation, low cost, and high chemical stability. However, asbestos has been removed from commercial devices due to health risks.

Experimental materials such as potassium titanate have been used in some alkaline cells. Currently, most commercial EZs use Zirfon UTP 500® separators, which consist of a hydrophilic polyphenylene sulphide fabric coated with a polymer-zirconium oxide mixture. More recently, there has been growing interest in composite membranes based on polysulfone and mineral fillers [23]. These membranes have demonstrated superior performance compared to commercially available products, with the added advantage of enabling higher operating temperatures.

1.5 Conventional and zero-gap configurations

The original design of alkaline electrolyzers features solid electrodes immersed in an aqueous solution. In this configuration, a certain gap between the electrodes and the separator/diaphragm is required to allow for the proper movement of bubbles and electrolyte. Gas bubbles form on the electrode surface during the reaction and need space to escape; otherwise, their build up can obstruct ion transport to the electrode surface.

However, increasing the distance between the electrodes also increases resistance, which limits charge transport. Since hydrogen production is directly proportional to current density, this conventional design requires large electrode surface areas to generate significant hydrogen amounts, compensating for the lower current density. The zero-gap alkaline electrolysis configuration was first proposed in 1967 by Costa and Grimes [23]. By using mesh electrodes directly in contact with a microporous gas separator, research

demonstrated a substantial increase in current density, achieving up to 500 mA/cm² [34].

In the zero-gap design, electrodes are placed on either side of a membrane that conducts hydroxide ions and separates gases. Unlike traditional systems that use solid metal plates, this setup employs porous electrodes. The zero-gap configuration reduces the space between the electrodes to the thickness of the membrane (<0.5 mm), compared to the >2 mm typical of traditional setups [34]. This significantly reduces the ohmic resistance of the electrolyte between the electrodes. Additionally, in the zero-gap setup, gas bubbles are released from the back of the electrodes rather than between them, further lowering cell resistance. The two configurations are presented in Figure 1.2.

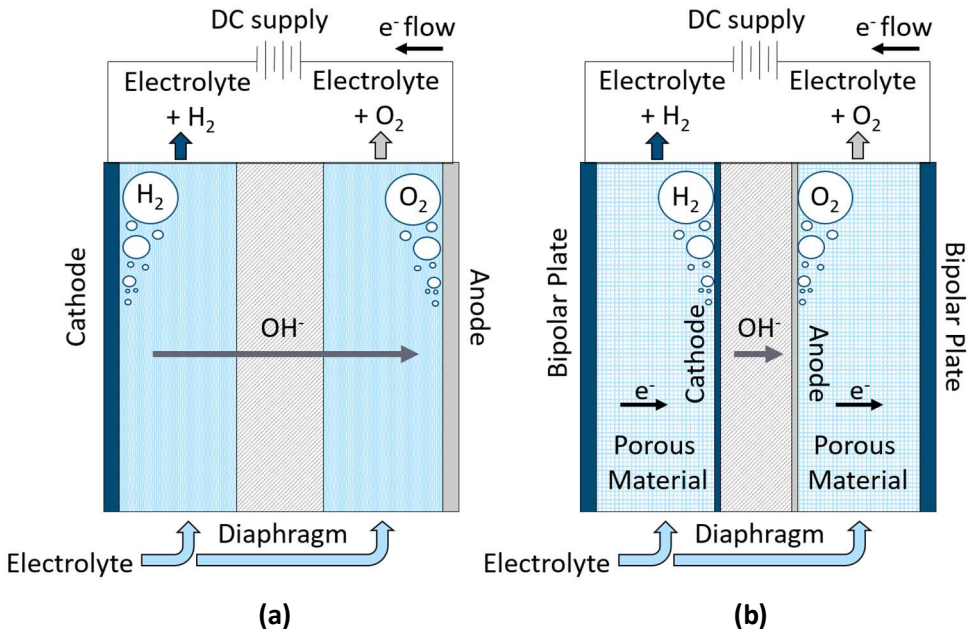

Figure 1.2: **(a)** Traditional and **(b)** zero-gap configurations of alkaline water electrolyzers.

With equal hydrogen production, the reduced overpotential in the zero-gap design decreases electrical consumption, improving efficiency and significantly enhancing cell performance. This combines the advantages of alkaline electrolysis, such as the avoidance of noble metals, with the high efficiencies associated with the more expensive PEM configuration. The design also offers a more compact system for the same level of hydrogen production. Consequently, most manufacturers today have adopted the zero-gap design.

However, the zero-gap configuration has some drawbacks, such as the need for dual electrolyte circuits, fluid circulation pumps, and electrolyte/gas separators.

Porous electrodes, such as nickel mesh/foam, are commonly employed [26]. Stainless steel coated with protective layers can also be used on the cathodic side, though it may corrode under high potentials in the presence of oxygen.

After this brief overview about the EZs components and geometries, the next subsections focus on the cells modeling techniques and insights coming from the literature. Accurate cell characterization is essential for improving efficiency. The studies reviewed provide the foundation upon which the present research was conducted.

1.6 AWEs modeling for optimized performance

Addressing challenges related to reducing energy consumption, costs, and maintenance while enhancing the efficiency and durability of AWE is crucial for advancing electrolysis. In this context, precise physical modeling plays a significant role. One of the most commonly used models is the one proposed by Ulleberg [35], which offers a mathematical representation of the polarization curve with empirically fitted parameters. However, such models typically do not account for geometric factors or effects influenced by the overall cell design. Additionally, thermal effects are often modeled using a simplified lumped thermal capacitance approach.

The efficiency of AWEs is influenced by both static factors, such as temperature and pressure, and dynamic factors, including electrolyte flow and gas evolution. Research indicates that bubbles generated during electrolysis play a dual role: they locally enhance turbulence, improving the transport of active species, but also reduce the effective electrode surface area, increasing the ohmic overpotential and energy loss. At higher current densities, the bubble layer significantly reduces conductivity, as discussed by Angulo *et al.* [36] and Zarghami *et al.* [37].

An additional challenge involves optimizing two-phase flow hydrodynamics within the cell. Gas accumulation can hinder performance by increasing electrolyte resistivity and causing localized hot spots, which can damage materials and shorten cell lifespan. Studies, such as those by Gao *et al.*, have shown that low velocities lead to bubble stagnation, higher local gas volume fractions, and decreased current densities [38]. Uniform electrolyte flow and proper gas removal mechanisms are critical for mitigating these effects and enhancing cell performance. With this in mind, to model the gas behavior, Rajora

and Haverkort provided analytical relations for velocity and gas volume fraction profiles near the electrode [39]. In this context, Aldas *et al.* thoroughly reviewed the literature concerning the influence of the main physical parameters on the bubble coverage of an electrode, showing how electrolyte velocities and current densities impact the gas volume fraction [40].

Shifting to the thermal discussion, the operation of an alkaline electrolyzer cells is significantly influenced by temperature, which impacts efficiency, voltage requirements, and overall performance. In particular, as temperature increases, the required cell voltage for electrolysis decreases. This reduction in voltage at higher temperatures leads to improved energy efficiency of the EZ, as also showed by the simulations by Gao *et al.* [38]. Muhsen *et al.* also studied the impact of temperature on the current density, correlating it to other parameters such as electrode-diaphragm gap [41]. They found out that, among the other factors analyzed, temperature ranked second, contributing for 29 % to the current variation, thus highlighting its crucial role in shaping the system's behavior. On the other hand, local high temperature values, or hot spots, are to be avoided, since they can compromise the material resistance. Norazahar *et al.* highlight that in PEM electrolysis hot spots at the anode, influenced by the quality and supply of water, can cause mechanical and chemical degradation, potentially leading to membrane drying due to excessive gas volume fraction. This phenomenon can significantly reduce cell lifespan [42]. While extensive studies on membrane degradation in PEM electrolysis exist, there remains a notable gap in such research for alkaline water electrolysis. The occurrence of hot spots is linked to the maldistribution of two-phase flow and current density. In [42] a large zone of lower liquid superficial velocities appears near the beginning of the channels. This zone coincides with the location of high gas volume fraction. Thus, the high extent of gas holdup appears to reduce the flow of the liquid phase, leading in turn to hot spots.

Optical techniques for electrolysis-modeling support often fail due to high gas fraction, making Computational Fluid Dynamics (CFD) essential. Furthermore, CFD is necessary to consider the influence of the cell geometry and for design optimization. However, consensus on suitable CFD models and methods for simulating cell hydrodynamics is lacking, given limited validation against experimental data.

A review of the relevant literature on the main CFD approaches in the literature will be provided in the next subsection. However, more detailed literature review will be explored throughout the theoretical description of Chapter 2, when dealing with the specific subjects under investigation.

1.7 CFD modeling approach: literature review

The choice of the multiphase settings, sub-models and interfacial forces is crucial to ensure the accuracy of a CFD approach for such complex applications as alkaline electrolyzers.

Concerning the fluid-dynamics model to be employed in case of biphasic flow liquid-gas, two are the main ones used in the literature, i.e., Euler-Euler and Euler-Lagrange. The former describes both phases with transport equations on a globally fixed coordinate system and the notion of volume fraction for each phase is introduced. The latter considers the electrolyte solution as a continuum phase and the bubbles as a discrete phase. In particular, the continuous phase is treated by solving the time-averaged Navier-Stokes equations, whereas Newton equation of motion is solved for each particle of the dispersed phase individually by tracking the particles.

Through investigation of the literature, a few recent CFD works were identified, with different numerical approaches.

In most of the analysed papers, an Euler-Euler model was used, with various flow conditions, mainly simulating lab-scale cells: on one side, a laminar model was employed by Le Bideau *et al.* [43] and Abdelouahed *et al.* [44]; on the other side, a turbulent regime was considered by Zarghami *et al.* [37], using Reynolds Stress Equations (RSE), and by El-Askary *et al.* [45], who employed a k- ε (STD) model, as recommended by Mat *et al.* in [46]. A turbulent, or bubble, dispersion force was introduced by most of the cited authors to account for the diffusion of the gas inside the cell, apart from Abdelouahed *et al.* [44], who considered a negative lift coefficient.

An Euler-Lagrange model was instead used by Hreiz *et al.* [1], and Mandin *et al.* [47] with introduction of bubbles at injection points using the Dispersed Phase Model (DPM). In that case, the flow regime was set as laminar and no dispersion forces were employed.

3D industrial-electrolyzer cells modeling is still rare in the literature ([38], [48], [49], [50]). Lee *et al*. developed a CFD analysis method for an AWE powered by renewable energy using COMSOL and considering the cell as isothermal [49]. Hawkes *et al.* used a 3D CFD electrochemical model to study a high-temperature electrolysis stack of solid oxide fuel cell (SOFC) using the commercial code Fluent [51]. Olesen *et al.* developed a PEM 3D model that accounts for compressible, two-phase flow including species, heat, and charge transport in the anode and membrane [52]. Still, a full alkaline EZ stack CFD analysis could not be found by the authors during the literature review.

Literature highlights the need for full-scale experimental validation to refine fluid dynamic models and address critical parameters such as gas bubble size distribution, especially under pressurized conditions.

Despite its maturity, AWE technology requires further optimization to maximize efficiency and reduce costs. The bubble dynamics and thermal effects must be carefully studied and managed to minimize energy losses. Advanced CFD simulations can provide insights into these phenomena, allowing for the design of more effective and robust electrolyzers.

Another challenge that water electrolysis faces is linked to safety risks associated with gas crossover or hydrogen leaking. The presence of hydrogen and oxygen in AWE systems presents a considerable explosion hazard, particularly when gas crossover occurs, leading to the formation of highly explosive mixtures. This risk is further amplified under high-pressure conditions, emphasizing the need for advanced control systems to regulate gas pressure and electrolyte flow. Moreover, due to its small molecular size and high diffusivity, hydrogen is highly susceptible to leakage, creating significant safety concerns. Being colorless and odorless, hydrogen leaks are challenging to detect, necessitating the use of advanced detection systems and strict safety protocols. This topic has been covered widely in the works conducted by [53] and [54], with particular focus on AWE cells. From this perspective, progressing in simulation technology could also be beneficial for dedicated risk studies.

In conclusion, a well-assessed methodology has not been developed yet, due to the novelty of the topic. Therefore, further studies are necessary to assess accuracy and predictive capabilities of multiphase models for this specific application. The present thesis tries to bridge this numerical gap.

2 PHYSICAL AND NUMERICAL THEORY

This chapter outlines the physical and CFD modeling theory, from two-phase fluid dynamics to electrochemical and thermal models, on which the research is based. The methodological framework described is tailored to the cases under investigation, to meet the unique demands of each scenario, as discussed in the subsequent chapters.

The following sections will provide a comprehensive overview of the available models and methodologies, highlighting choices made in the existing literature wherever applicable. It is worth noting that studies addressing such cases, particularly those employing Fluent software, remain relatively scarce in the current research field.

2.1 Two-phase flow

Electrolyzer cells exhibit a two-phase flow comprising a liquid electrolyte and gas bubbles generated at the electrodes. Multiphase fluid dynamics has been extensively studied over the past century. One of the earliest efforts to incorporate two-phase phenomena into modeling was by Lockhart and Martinelli [55], who developed an empirical correlation to predict the pressure drop in two-phase flows based on the pressure drops of the individual phases. Subsequent studies sought to enhance this correlation by accounting for the flow regime of each phase. Years later, Ishii [56] introduced one of the most widely recognized two-phase flow models, which was later employed to construct a flow regime map as a function of individual gas and liquid velocities.

Further research has improved understanding the influence of two-phase flow regimes on transport properties.

In computational fluid dynamics (CFD) simulations, two main approaches are commonly employed to model such flows. The Euler-Lagrange method treats the electrolyte as a continuous phase and gas bubbles as discrete entities, while the Euler-Euler method represents both phases as interpenetrating continua.

More broadly, fluid motion can be described using two reference systems: fixed or moving. The Lagrangian approach focuses on individual particles within the continuum, tracking their motion over time. In contrast, the Eulerian approach describes fluid motion from a fixed spatial point, observing how different particles pass through this point over time.

From the Eulerian point of view, the observer is attached to a fixed or inertial reference and identifies the velocity (or pressure) field at each time step, without having information about the motion of individual fluid particles. This type of motion specification relies on the mathematical concept of a field, meaning that the flow properties (velocity, density, pressure) are defined as functions of space, i.e., the position vector x, and time t. For example, the velocity of the fluid would be expressed as $\vec{v} = \vec{v}(x, t)$. With this approach, it can be useful to define a control volume to observe the fluid in a portion of space. A control volume is a geometric entity, distinct from the mass it contains, through which fluid flows. The Navier-Stokes equations are typically formulated in this reference frame.

In contrast, the Lagrangian approach describes motion by focusing on individual fluid particles rather than a specific control volume. In this framework, flow properties are determined for each fluid particle, with its center of mass located at the initial position x_0, and varying over time t. The velocity of the fluid is expressed as $\vec{v} = \vec{v}(x_0, t)$. The Maxey and Riley equation represents the force balance acting on an individual particle within this reference frame.

In ANSYS Fluent, three Euler–Euler multiphase models are available: the volume of fluid (VOF) model, the mixture model, and the Eulerian model. Unlike the first two, the Eulerian model solves a separate set of continuity equations for each phase, with coupling achieved through pressure and interphase interaction coefficients. Given the dispersed nature of the bubbles, the two-phase Eulerian model was selected. A brief overview of the mathematical framework is provided in the following section to support the interpretation of the results.

2.1.1 Euler-Lagrange Model

The Euler-Lagrange model is a Lagrangian approach applied to discrete phases, treating the electrolyte as a continuous phase and gas bubbles as a discrete phase. The fluid phase is modeled as a continuum by solving the Navier-Stokes equations, while the trajectories of the discrete particles are tracked within the computed flow field. This model allows for the exchange of momentum, mass, and energy between the dispersed and fluid phases. It has been utilized in studies conducted by Mandin *et al.* [47] and Hreiz *et al.* [1].

In the Euler-Lagrange approach, the trajectory of a particle in the discrete phase is predicted by integrating the force balance on the particle, which is written in a Lagrangian reference frame. Specifically, Eq. 2.1 represents the momentum continuity equation:

$$m_g \frac{d\vec{v}_g}{dt} = m_g \frac{\vec{g}(\rho_g - \rho_l)}{\rho_g} + m_g \frac{\rho_l}{\rho_g}(\vec{v}_l \nabla \vec{v}_l) + \vec{F}_d + \vec{F}_{lift,Saf} + \vec{F}_{lift,Mag} + \vec{F}_{vm} + \vec{F}_{rot}, \tag{2.1}$$

where m_g is the particle mass, $\vec{v}_l$ is the velocity of the fluid phase, $\vec{v}_g$ is the velocity of the particle, ρ_l and ρ_g are the liquid and gas density respectively, $\vec{F}_{lift,Saf}$ is the lift force due to shear (Saffman force), $\vec{F}_{lift,Mag}$ is the Magnus lift force that occurs when the particle is rotating in a fluid, $\vec{F}_{vm}$ refers to the virtual mass force, $\vec{F}_{rot}$ to forces that arise due to the rotation of the reference system and $\vec{F}_d$ is the drag force, defined as in Eq. 2.2:

$$\vec{F}_d = m_g \frac{\vec{v}_l - \vec{v}_g}{\tau_r}, \tag{2.2}$$

where τ_r is the relaxation time for the particles, defined as:

$$\tau_r = \frac{\rho_g d_b^2}{18\mu} \frac{24}{C_d Re}, \tag{2.3}$$

where μ is the molecular viscosity of the fluid, d_b is the bubble diameter, and Re is the Reynolds number:

$$Re = \frac{\rho d_b |\vec{v}_g - \vec{v}_l|}{\mu}, \quad 2.4$$

Along with the equation for the conservation of momentum, the conservation of angular momentum for the particle is also solved. Rotation can indeed have a significant influence on the trajectory of a particle moving in a fluid, with the impact being even more pronounced for larger particles with higher moments of inertia, Eq. 2.5:

$$I_g \frac{d\vec{\omega}_g}{dt} = \frac{\rho_l}{2} \left(\frac{d_b}{2}\right)^5 C_\omega |\vec{\Omega}| \cdot \vec{\Omega} = \vec{T}, \quad 2.5$$

where I_g is the moment of inertia, $\vec{\omega}_g$ is the angular velocity of the particle, ρ_l is the fluid density, d_b is the bubble diameter, C_ω is the rotational drag coefficient, $\vec{T}$ is the torque applied to a particle in the fluid domain, and $\vec{\Omega}$ is the relative angular velocity, Eq. 2.6, between the particle and the fluid:

$$\vec{\Omega} = \frac{1}{2} \nabla \times \vec{v}_l - \vec{\omega}_g. \quad 2.6$$

The moment of inertia I_g for a spherical particle is given by Eq. 2.7:

$$I_g = \frac{\pi}{60} \rho_g d_b^5. \quad 2.7$$

2.1.2 Euler-Euler Model

In the Euler-Euler approach, each phase is mathematically represented as a continuous, overlapping entity. To account for the fact that the volume of one phase cannot overlap with that of another, the concept of phase volume fraction is introduced. These volume fractions are treated as continuous functions of space and time, with their sum equal to one. Conservation equations are solved for each phase, supplemented by constitutive relations derived from empirical data to close the system. In ANSYS Fluent, three Euler-Euler multiphase models

are available: the Volume of Fluid (VOF) model, the Mixture model, and the Eulerian model.

2.1.2.1 VOF Model

The VOF (Volume of Fluid) model is a surface-tracking method applied to a fixed Eulerian mesh. It is designed for immiscible fluids where tracking the interface between phases is essential. The VOF model is well-suited for flows with a clearly defined phase interface, provided the interface curvature radius is significantly larger than the mesh size. The formulation explicitly captures the interface within the domain, ensuring that the two phases neither overlap nor mix. In this approach, a single set of momentum equations is shared by the fluids, while the volume fraction of each fluid is tracked in every computational cell across the domain. However, this model is not ideal for simulating flow within an electrolytic cell, due to the dispersed conditions of the gas.

2.1.2.2 Mixture Model

The mixture model is a simplified multiphase model. It can be used to model a homogeneous multiphase flow, treating the fluid as a gas-liquid mixture. The model solves the continuity equation, Eq. 2.8, for the mixture and specifies relative velocities to describe the dispersed phases. The mixture model has been employed by researchers such as Dahlkild *et al.* [57], Wedin and Dahlkild [58], and Schillings *et al.* [59].

$$\frac{\partial(\rho_m)}{\partial t} + \nabla \cdot (\rho_m \vec{v}_m) = 0, \tag{2.8}$$

where $\vec{v}_m$ is the mass-weighted velocity, Eq. 2.9, and ρ_m is the mixture density, Eq. 2.10:

$$\vec{v}_m = \frac{\sum_{k=1}^{n} \alpha_k \rho_k \vec{v}_k}{\rho_m} = \frac{\alpha_g \rho_g \vec{v}_g + \alpha_l \rho_l \vec{v}_l}{\rho_m}, \tag{2.9}$$

$$\rho_m = \sum_{k=1}^{n} \alpha_k \rho_k = \alpha_g \rho_g + \alpha_l \rho_l \ , \tag{2.10}$$

where α_k is the volume fraction of phase k.
The momentum equation in the mixture model can be described as:

$$\begin{gathered}\frac{\rho_m \partial \vec{v}_m}{\partial t} + \nabla \cdot (\rho_m \vec{v}_m \vec{v}_m) = \\ -\nabla p + \nabla \cdot [\mu_m (\nabla \vec{v}_m + \nabla \vec{v}_m^T)] + \rho_m \vec{g} + \vec{F} - \\ \nabla \cdot (\alpha_g \rho_g \vec{v}_{dr,g} \vec{v}_{dr,g} + \alpha_l \rho_l \vec{v}_{dr,l} \vec{v}_{dr,l}),\end{gathered} \tag{2.11}$$

where $\vec{F}$ is a body force, and μ_m is the viscosity of the mixture, while $\vec{v}_{dr,l}$ and $\vec{v}_{dr,g}$ are the liquid and gas drift velocities, respectively.

$$\mu_m = \sum_{k=1}^{n} \alpha_k \mu_k = \alpha_g \mu_g + \alpha_l \mu_l, \tag{2.12}$$

$$\vec{v}_{dr,g} = \vec{v}_g - \vec{v}_m, \tag{2.13}$$

$$\vec{v}_{dr,l} = \vec{v}_l - \vec{v}_m. \tag{2.14}$$

2.1.2.3 Eulerian Model

The Eulerian model is the most complex of the multiphase models. It solves a set of continuity equations for each phase. The coupling is achieved through pressure and interphase exchange coefficients. The Eulerian model has been used to model the behavior within electrolyzers by Aldas *et al.* [40], Mat *et al.* [46], and Le Bideau *et al.* [43].

Thus, in the examined two-phase case, the system is solved in the Eulerian model by setting the equations for both the liquid and gas phases. The mass continuity equations for the two-phase Eulerian model can be written for each phase as displayed in Eq. 2.15 and 2.16, with subscript “l” referring to the liquid phase and subscript “g” to the gas phase [60]:

$$\frac{\partial}{\partial t}(\alpha_l \rho_l) + \nabla \cdot (\alpha_l \rho_l \vec{v}_l) = (\dot{m}_{gl} - \dot{m}_{lg}) + S_l, \tag{2.15}$$

$$\frac{\partial}{\partial t}(\alpha_g \rho_g) + \nabla \cdot (\alpha_g \rho_g \vec{v}_g) = (\dot{m}_{lg} - \dot{m}_{gl}) + S_g, \tag{2.16}$$

where α_k, ρ_k, $\vec{v}_k, S_k$ are, respectively, the volume fraction, the density, the velocity, and the mass source term of phase "k", while $\dot{m}_{lg}$ and $\dot{m}_{gl}$ indicate the mass transfer from the liquid phase to the gas phase and vice versa.

Equations 2.17 and 2.18 represent the momentum continuity equations for each phase [60]:

$$\begin{aligned}&\frac{\partial}{\partial t}(\alpha_l\rho_l\vec{v}_l)+\nabla\cdot(\alpha_l\rho_l\vec{v}_l\vec{v}_l)=\\&-\alpha_l\nabla p+\nabla\cdot\left(\alpha_l\overline{\overline{T_l}}\right)+\alpha_l\rho_l\vec{g}+\\&\left(\vec{F}_{d,gl}+\dot{m}_{gl}\vec{v}_{gl}+\dot{m}_{lg}\vec{v}_{lg}\right)+\\&\left(\vec{F}_l+\vec{F}_{lift,l}+\vec{F}_{wl,l}+\vec{F}_{vm,l}+\vec{F}_{td,l}\right),\end{aligned} \tag{2.17}$$

$$\begin{aligned}&\frac{\partial}{\partial t}(\alpha_g\rho_g\vec{v}_g)+\nabla\cdot(\alpha_g\rho_g\vec{v}_g\vec{v}_g)=\\&-\alpha_g\nabla p+\nabla\cdot\left(\alpha_g\overline{\overline{T_g}}\right)+\alpha_g\rho_g\vec{g}\\&+\left(\vec{F}_{d,lg}+\dot{m}_{lg}\vec{v}_{lg}+\dot{m}_{gl}\vec{v}_{gl}\right)+\\&\left(\vec{F}_g+\vec{F}_{lift,g}+\vec{F}_{wl,g}+\vec{F}_{vm,g}+\vec{F}_{td,g}\right),\end{aligned} \tag{2.18}$$

where p is the pressure shared between the two phases, $\vec{F}_l$ and $\vec{F}_g$ are external body forces, $\vec{F}_{d,lg}=-\vec{F}_{d,lg}$ is the drag force and $\vec{v}_{lg}=-\vec{v}_{gl}$ is the interphase velocity $\vec{F}_{lift,}$ and $\vec{F}_{lif}$ are the lift forces, $\vec{F}_{wl,l}$ and $\vec{F}_{wl,g}$ are the wall lubrication forces, $\vec{F}_{vm,l}$ and $\vec{F}_{vm,g}$ are the virtual mass forces, and $\vec{F}_{td,l}$ and $\vec{F}_{td,g}$ are the turbulent dispersion forces. Finally, $\overline{\overline{T_l}}$ and $\overline{\overline{T_g}}$ are the stress tensors, Eq. 2.19 and 2.20 including both viscous and turbulent tensions [60]:

$$\overline{\overline{T_l}}=2\ \mu_l\left(\overline{\overline{D_l}}-\frac{1}{3}tr(\overline{\overline{D_l}})\bar{\bar{I}}\right)-\rho_l\overline{\overline{R_l}}, \tag{2.19}$$

$$\overline{\overline{T_g}}=2\ \mu_g\left(\overline{\overline{D_g}}-\frac{1}{3}tr(\overline{\overline{D_g}})\bar{\bar{I}}\right)-\rho_g\overline{\overline{R_g}}, \tag{2.20}$$

where $\overline{\overline{D_l}}$ and $\overline{\overline{D_g}}$ are the strain tensors, defined as in Eq. 2.21 and 2.22, and $\overline{\overline{R_l}}$ and $\overline{\overline{R_g}}$ are Reynolds stress tensors, defined as in Eq. 2.23 and 2.24 [60]:

$$\overline{\overline{D_l}} = 0.5(\nabla \vec{v}_l + (\nabla \vec{v}_l)^T), \quad 2.21$$

$$\overline{\overline{D_g}} = 0.5(\nabla \vec{v}_g + (\nabla \vec{v}_g)^T), \quad 2.22$$

$$\overline{\overline{R_l}} = < \overrightarrow{v'}_l \overrightarrow{v'}_l >, \quad 2.23$$

$$\overline{\overline{R_g}} = < \overrightarrow{v'}_g \overrightarrow{v'}_g >, \quad 2.24$$

with operator <> indicating a Reynolds average operation.

2.1.2.4 Species transport equation

Coming to the species transport equation, Fluent predicts the local mass fraction of each species Y_j, through the solution of a convection-diffusion equation for the j[th] species. This conservation equation takes the general form of Eq. 2.25 [60]:

$$\frac{\partial(\rho_k Y_j)}{\partial t} + \nabla \cdot (\rho_k \vec{v}_k Y_j) = -\nabla \cdot (\vec{J}_j) + \dot{R}_j + \dot{S}_j, \quad 2.25$$

where R_j is the net rate of production of species by chemical reaction and $\dot{S}_j$ is the rate of creation by addition from the dispersed phase plus any user-defined sources (UDS). Finally, $\vec{J}_j$ represents the diffusion flux of the j[th] species, which arises due to gradients of concentration and temperature.

2.1.2.5 Forces

The force that most significantly influences the movement of bubbles inside the cell is the buoyancy force due to a significant difference in density between the electrolyte and gaseous hydrogen. Among interface forces exchanged between the gas and liquid phases, the main ones generally employed to implement the Eulerian model are drag, lift, wall lubrication, virtual mass, surface tension and turbulent dispersion forces. The drag force, Eq. 2.26, represents the liquid resistance of gas bubbles to the movement, acting in the

opposite direction of the bubble-liquid slip velocity, and expressed as follows [60]:

$$\vec{F}_d = -\frac{3}{4}\frac{C_d \alpha_g \rho_l}{d_b}\left|\vec{v}_g - \vec{v}_l\right|(\vec{v}_g - \vec{v}_l), \qquad 2.26$$

where C_d is the drag coefficient, whose expression depends on the specific model employed.

For multiphase flows, the lift force acting on bubbles in the secondary phase can be included in the model. This force arises due to the pressure difference on the sides of the gas bubbles, caused by velocity gradients in the primary phase's flow field, consistent with Bernoulli's equation. The lift force, displayed in Eq. 2.27, becomes more significant for larger bubbles [60]:

$$\vec{F}_{lift} = -C_{lift}\rho_l \alpha_g (\vec{v}_l - \vec{v}_g) \times (\nabla \times \vec{v}_l). \qquad 2.27$$

The lift force is relatively small compared to the drag force and is often omitted in simulations, as seen in the study by Zarghami *et al.* [37]. Conversely, researchers like Le Bideau *et al.* [43] and Schillings *et al.* [59] chose to include this contribution, employing the Saffman-Mei lift coefficient C_{lift}. When the lift force is significant (such as in scenarios where phases separate rapidly) its inclusion becomes essential. For example, in the investigation by Garcia-Navarro *et al.* [61], the lift force was critical for accurately determining the bubble's radius and angle at detachment, as its contribution could not be neglected.

The wall lubrication force in liquid-gas bubbly flows accounts for the effects of wall lubrication forces on the secondary phases (bubbles). This force typically acts to push the gas phase away from the electrode surfaces, helping to maintain separation and reducing bubble accumulation near the walls. It is calculated by the software as Eq. 2.28 [60]:

$$\vec{F}_{wl} = C_{wl}\alpha_g \rho_l \left|(\vec{v}_g - \vec{v}_l)_t\right|^2 \vec{n}_w, \qquad 2.28$$

where C_{wl} is the wall lubrication coefficient, $(\vec{v}_g - \vec{v}_l)_t$ the relative velocity component tangential to the wall surface, and $\vec{n}_w$ the unit vector perpendicular to the wall.

The virtual mass force is a phenomenon in two-phase flows that arises when the secondary phase accelerates relative to the primary phase. This force, calculated by Eq. 2.29 [60], is significant in scenarios where there is a considerable density difference between the two phases. It represents the

additional inertia that needs to be accounted for as the accelerating secondary phase displaces part of the primary phase. This force is particularly relevant in systems involving large bubbles or particles moving in a lighter fluid, where such density contrasts amplify its effects. It can be expressed as:

$$\vec{F}_{vm} = C_{vm}\alpha_g\rho_l\left(\frac{d\vec{v}_g}{dt} - \frac{d\vec{v}_l}{dt}\right), \qquad 2.29$$

where C_{vm} is the virtual mass coefficient, chosen equal to 0.5 in case of spherical shape hypothesis for the gas bubbles. Studies like Zarghami *et al.* [37] observed that including virtual mass forces in the model led to spurious effects on gas fraction profiles, making the results time-dependent. Consequently, they decided to exclude these forces. Simulations of gas generation near the electrode surface often predict that the produced bubbles remain confined near the wall, forming a bubble curtain with a nearly constant vertical thickness. This approach fails to reproduce the bubble curtain's diffusion or the presence of bubbles in the channel's center, which contradicts experimental observations.

The ability of CFD models to predict the width of the hydrogen bubble curtain (a crucial flow characteristic) is a key measure of the model's accuracy and reliability. According to Mandin *et al.* [47], and Abdelouahed *et al.* [44], when bubble dispersion or lateral migration terms are absent, CFD simulations generally fail to reproduce the bubble curtain's vertical spreading. Since the mechanisms driving bubble curtain diffusion remain poorly understood, researchers have introduced various empirical terms to capture these effects: pseudo-turbulence terms in relative velocity equations (Dahlkild *et al.* [57]; Wedin and Dahlkild [58]; Ipek *et al.* [62]) bubble diffusion terms in continuity equations (Mat *et al.* [46]; Aldas *et al.* [40]), lift force terms in momentum balance equations (Abdelouahed *et al.* [44]), and constant horizontal volumetric force terms (Mandin *et al.* [47]). Abdelouahed *et al.* [44] used a lift force term in the momentum balance equations with a negative coefficient, possibly accounting for complex hydrodynamic effects not included in the Euler-Euler framework, as suggested by Hreiz *et al.* [1] and Mandin *et al.* [47], to mimic experimental bubble dispersion, introduced a constant horizontal volumetric force in the gas momentum balance. However, Hreiz *et al.* [1] criticized this method for its lack of physical significance and generality. Boissoneau *et al.* [63] observed turbulence induced by bubbles in the upper part of the electrochemical cell. Aldas *et al.* [40], using a fully laminar model, found that it underestimated gas volume fraction distribution compared to experiments, concluding that local weak turbulence must be accounted for. Turbulent fluctuations introduce randomness to relative phase velocities, distorting bubble

trajectories due to the random motion of continuous phase vortices. This phenomenon can be modeled as a turbulent dispersion force acting on the gas phase, representing interphase momentum transfer due to turbulent eddies. The turbulent dispersion force, combined with the drag force (which captures mean interphase momentum exchange), provides the instantaneous drag force. It tends to flatten volume fraction distribution. This force accounts for the interaction of turbulent fluctuations with phase distribution, contributing to a more realistic simulation of gas-liquid flows. By redistributing bubbles across the flow domain, it helps address inaccuracies like the confinement of bubbles near walls observed in simpler models.

Zarghami *et al.* [37] define the turbulent dispersion force as follows in Eq. 2.30:

$$\vec{F}_{td} = -\frac{3}{4}\frac{C_d}{d_b}\alpha_g|\vec{v}_g - \vec{v}_l|\frac{\mu_l^{turb}}{Sc}\left(\frac{1}{\alpha_g}+\frac{1}{\alpha_l}\right)\nabla\alpha_g, \tag{2.30}$$

$$Sc = 0.9, \tag{2.31}$$

where Sc of Eq. 2.30, is the turbulent dispersion coefficient of Schmidt and μ_l^{turb} the turbulent viscosity.

Le Bideau *et al.* [43] simulate turbulence-like behavior within a laminar flow framework by introducing the term of Eq. 2.32:

$$\vec{F}_{td} = -\alpha_g\rho\frac{K_g}{d_b}|\vec{v}_g - \vec{v}_l|\nabla\alpha_g. \tag{2.32}$$

where K_g of Eq.2.32, is the turbulent dispersion coefficient of Schmidt and μ_l^{turb} the turbulent viscosity.

Hreiz *et al.* [1], on the other hand, consider unnecessary to introduce additional or "artificial" terms for lateral bubble migration in the model. Instead, their approach employs an Euler-Lagrange framework that treats bubble generation as an injection occurring at a distance equal to the bubble radius from the electrode surface. By using this configuration, their simulations successfully replicate, with good agreement to experimental results, both the dispersion of bubble curtains and the presence of bubbles in the central part of the channel. However, they also demonstrate that the numerical outcomes are highly sensitive to the initial positioning of the bubble. This sensitivity highlights the

importance of accurate modeling of initial bubble placement in predicting realistic flow dynamics.

2.1.2.6 Turbulence

Regarding flow conditions, many studies employ laminar flow assumptions. For example, Le Bideau *et al.* [43] observed Reynolds numbers between 240 and 480, while Abdelouahed *et al.* [44] and Ramirez *et al.* [64] also utilized laminar conditions. In these analyses, the Reynolds stress tensor is set to zero since velocity fluctuations are absent. On the other hand, some studies consider turbulent flow regimes, such as those by Rodriguez and Amores [27] and Zarghami *et al.* [37]. Zarghami *et al.* recorded a Reynolds number of 7600, whereas the transition from laminar to turbulent flow is typically identified at a critical Reynolds number of 2100. Rodriguez and Amores [27] employed a $k-\varepsilon$ turbulence model. This model, like the $k-\omega$ model, uses the Boussinesq hypothesis to relate the Reynolds stress tensor to mean velocity gradients, as in Eq. 2.33:

$$-\rho_l \overline{\overline{R}}_l = -\rho_l < \overrightarrow{v'}_l \overrightarrow{v'}_l >= 2\mu_l^{turb} \overline{\overline{D}}_l - \tfrac{2}{3}\rho_l k \bar{\bar{I}} \ , \qquad 2.33$$

where, $\overline{\overline{R}}_l$ is the Reynolds stress tensor, k the turbulent kinetic energy and μ_l^{turb} is the eddy viscosity, defined as Eq. 2.34:

$$\mu_l^{turb} = \ \rho_l C_\mu \ k^2/\varepsilon, \qquad 2.34$$

where C_μ is a constant of the turbulent model and ε is the turbulent energy dissipation rate, defined as:

$$\varepsilon = \frac{\mu_l^{turb}}{\rho_l} < \frac{\partial v_i'}{\partial x_j} \frac{\partial v_j'}{\partial x_i} >, \qquad 2.35$$

This approach simplifies the complex behavior of turbulence by linking it to average flow properties. The $k-\varepsilon$ model, to determine the turbulent viscosity μ_l^{turb}, solves two additional transport equations: one for the turbulent kinetic energy k and one for the turbulent energy dissipation rate ε. Such transport equations are expressed as follows in Eq. 2.36 and 2.37:

$$\rho_l \frac{\partial k}{\partial t} - \nabla \left[\left(\mu_l + \frac{\mu_l^{turb}}{\phi_k} \right) \nabla k \right] + \rho_l \vec{v}_l \nabla k = \frac{1}{2} \mu_l^{turb} (\nabla \vec{v}_l + \nabla \vec{v}_l{}^T)^2 - \rho_l \varepsilon + T_b, , \quad 2.36$$

$$\rho_l \frac{\partial \varepsilon}{\partial t} - \nabla \left[\left(\mu + \frac{\mu_l^{turb}}{\phi_\varepsilon} \right) \nabla \varepsilon \right] + \rho_l \vec{v}_l \nabla \varepsilon = \frac{1}{2} C_{\varepsilon 1} \frac{\varepsilon}{k} \mu_l^{turb} (\nabla \vec{v}_l + \nabla \vec{v}_l{}^T)^2 - \rho_l C_{\varepsilon 2} \frac{\varepsilon^2}{k} + \frac{\varepsilon}{k} C_\varepsilon T_b \, , \quad 2.37$$

where $C_\varepsilon = 0.25$, $C_{\varepsilon 1} = 1.44$, $C_{\varepsilon 2} = 1.92$, ϕ_k and ϕ_ε are constants of the turbulence model. The term T_b is related to turbulence induced by bubbles.

In the $k - \omega$ turbulence model, along with the transport equation for turbulent kinetic energy, instead of the transport equation for the rate of dissipation, the transport equation for the specific turbulent dissipation rate, denoted by ω, is used. Such equation is written as follows in Eq. 2.38:

$$\rho_l \frac{\partial \omega}{\partial t} - \nabla \left[\left(\mu + \frac{\mu_l^{turb}}{\phi_\omega} \right) \nabla \varepsilon \right] + \rho_l \vec{u}_l \nabla \omega = \frac{1}{2} \alpha \frac{\omega}{k} \mu_l^{turb} (\nabla \vec{v}_l + \nabla \vec{v}_l{}^T)^2 - \beta \rho_l \omega^2 + S_\omega, , \quad 2.38$$

where $\beta = 0.075$, S_ω represents the turbulence dissipation source terms and ω is defined as in Eq. 2.39:

$$\omega = C_\mu \frac{\varepsilon}{k}, \quad 2.39$$

with constant $C_\mu = 0.09$. The SST (Shear Stress Transport) model combines the $k - \omega$ and $k - \varepsilon$ turbulence models in such a way that the first is used in the inner region of the boundary layer, while the second is used in the free-stream regions where shear stresses are absent.

Following a different approach, Zarghami *et al.* [37] used the RSM (Reynolds Stress Model) for their study. The RSM, also called the second moment closure model, is the most comprehensive approach to turbulence modeling. Turbulent viscosity models such as $k - \varepsilon$ and $k - \omega$ have significant limitations in complex flows. This is because these models assume that turbulent viscosity μ_l^{turb} is a scalar, isotropic quantity. Therefore, in flows with a high degree of anisotropy,

high curvature of flow lines, flow separation, recirculating flow regions, or flows influenced by rotational effects, these models do not provide satisfactory results. In such flows, the RSM offers better accuracy, as it accounts for the more complex interactions of turbulent stresses. In this model, in addition to the transport equation for the turbulent dissipation rate, the transport equation for the Reynolds stress tensor is also solved, as follows in Eq. 2.40:

$$\frac{\partial\left(\alpha_l\rho_l\overline{\overline{R_l}}\right)}{\partial t}+\nabla\cdot\left(\alpha_l\rho_l\vec{v}_l\times\overline{\overline{R_l}}\right)= \\ \nabla\cdot\left(\alpha_l(\mu_l^{mol}+C_s\mu_l^{turb})\nabla\times\overline{\overline{R_l}}\right)+\alpha_l\rho_l\left(\bar{\bar{P}}_l+\bar{\bar{\phi}}_l-\tfrac{2}{3}\varepsilon_l\bar{\bar{I}}\right), \tag{2.40}$$

$$\bar{\bar{P}}_l=-2\overline{\overline{R_l}}\cdot\overline{\overline{D}}_l, \tag{2.41}$$

where $\bar{\bar{P}}_l$ of Eq. 2.41 indicates the production due to main shear and $\bar{\bar{\phi}}_l$ the pressure-deformation model formulated by Gibson and Launder [65].

2.2 Porous model

In case of zero-gap configurations, as already described in Section 1.5, the electrolyte flows through an elastic porous matrix, which allows for the conduction of electrons from the bipolar plates to the actual electrodes. Thus, the description of porous modeling is necessary.

The most common laws employed to model the behaviour of a single-phase liquid through a porous material are Darcy and Forchheimer equations [66]. Darcy equation (Eq. 2.42) can be applied in laminar conditions and relates the pressure gradient through the medium ∇p to the superficial velocity vector $\vec{v}_D$ also called Darcy's velocity [66]:

$$\overrightarrow{v_D}=-\frac{k}{\mu}\nabla p, \tag{2.42}$$

where k is the permeability of the porous medium (m²) and μ the dynamic viscosity of the fluid.

Forchheimer equation (Eq.2.43) introduces an inertial term to Darcy equation, more suitable for turbulent conditions [66]:

$$\nabla p = -(\alpha_F \mu \overrightarrow{v_D} + \beta_F \rho |\overrightarrow{v_D}| \overrightarrow{v_D}), \quad 2.43$$

where α_F is the reciprocal of k and β_F is an empirical coefficient, called Forchheimer inertial term, that quantifies the inertial resistance in the porous medium.

2.3 Electrochemical model

The electrode kinetics of an electrolyzer cell can be modeled using empirical current-voltage relationships, the polarization curve [35]. Such curve is the characteristic graph of the electrolyzer, showing the variation of its cell potential in relation to current density. The basic equation of electrolysis to express the cell potential is:

$$U_{cell} = U_{rev} + U_{act} + U_{ohm} + U_{conc} \quad 2.44$$

where U_{rev} is the reversible potential of the cell, U_{act} is the activation overpotential, U_{conc} is the concentration overpotential and U_{ohm} is the ohmic component, related to the electrical resistances. Each polarization represents a source of loss in efficiency.

U_{rev} can be obtained through Nernst equation, as in [67], with a thermodynamic approach including thermal and barometric effects:

$$U_{rev} = U^0{}_{rev} + \frac{RT}{nF} ln \left((p_{gas} - p_w)^{1.5} \frac{p_{w^\circ}}{p_w} \right), \quad 2.45$$

where $U^0{}_{rev}$ is the reversible potential in standard conditions, and $p_{gas}, p_w, p_{w^\circ}$ are respectively the partial pressures of the gas, of water vapor and of water vapor at standard temperature.

For the activation overpotential of anode and cathode $U_{ac}{}_{a/c}$, Tafel equation can be employed [68]:

$$U_{\mathrm{act}_{a/c}} = \frac{RT}{nF\gamma_{a/c}} ln \left(\frac{i}{i_{0}{}_{a/c}} \right), \quad 2.46$$

where $i_{0_{a/c}}$ are the exchange current densities for anode and cathode and $\gamma_{a/c}$ are anode and cathode transfer-charge coefficients, which are dependent on material and temperature.

Ohmic component U_{ohm} is related to the single resistances that can be found inside the cell, including electrodes, membrane and the gas trapped inside the electrolyte, that works as an insulator [68]. According to Zeng and Zhang, the ohmic overpotential could even constitute the main contribution to the total energy loss of the electrolyzer cell [69]. Ohmic overpotential can be described using Eq. 2.47 [70]:

$$U_{ohm} = R_e + R_{mem} + R_b + R_{circ}, \qquad 2.47$$

where R_e is the electrolyte resistance, R_{mem} is the membrane resistance, R_b is the resistance linked to the gas bubbles and R_{circ} is the resistance linked to the electric circuit. Although R_{circ} and R_{mem} remain constant and can be reduced by optimizing the membrane and wire connections, R_b is not constant.

R_{mem} represents the term related to the diaphragm for the traditional cell design and to the porous, conducive material for the zero-gap design, as can be evaluated from Figure 1.2.

Bubbles adhering to the electrode surface disrupt the electric field, causing a high bubble resistance and resulting in a significant ohmic voltage drop [71]. This phenomenon is also called bubble coverage. Furthermore, the dispersion of these bubbles in the electrolyte increases the electrolyte resistance R_e by reducing its conductivity. As the number of bubbles generated at the electrode grows, bubble resistance rises, leading to greater energy consumption. Therefore, minimizing the gas volume and bubble residence time at the electrode is crucial for maintaining high current densities in water electrolysis [70]. Bubbles have in fact a double effect: the ones attached to the electrode contribute to reducing the effective area for the reaction, whereas the ones detached from electrode increase electrolyte resistivity [72]. Aldas *et al.* [40] thoroughly reviewed the literature concerning the influence of the main physical parameters on the bubble coverage of an electrode, showing how electrolyte velocities and current densities impact the gas volume fraction.

Concentration overpotential becomes significant at higher current densities than those of the industrial electrolyzers considered in this thesis. From a commercial perspective, exploring operation at current densities exceeding the typical range could be beneficial. In such cases, incorporating U_{conc} into the model would be essential. A potential definition of U_{conc} can be found in [73]:

$$U_{conc} = \frac{RT}{nF} ln\left(1 - \frac{i}{i_1}\right), \quad 2.48$$

where i_1 is the maximum rate of current density.

The efficiency of an alkaline electrolyzer can be described in terms of its electrical efficiency and overall efficiency. Electrical efficiency is defined as the ratio of the electrical energy used in the electrolysis process to the lower heating value (LHV) of the hydrogen gas produced. Overall efficiency, on the other hand, accounts for all energy losses during the electrolysis process, including heat losses and other auxiliary energy requirements. As a result, overall efficiency is typically lower than electrical efficiency and is influenced by factors such as operating temperature, pressure, current density, and water input purity. Faradaic efficiency η can be defined as in Eq. 2.49 [68]:

$$\eta = \frac{U_{rev}}{U_{cell}}. \quad 2.49$$

Faradaic efficiency is an important performance metric used to assess the effectiveness of an electrolyzer in converting electrical energy into the desired chemical reaction. According to Angulo *et al.* [36], bubbles removal through ultrasonic field leads to a possible decrease of the cell potential by 10-25%, thereby increasing the faradaic efficiency. These percentages give an idea of the impact of the gas accumulation inside the cell on its performance.

To find the gas generation at the electrodes, based on the applied current density, Faraday's Law is employed, expressed as in Eq. 2.50 [74]:

$$\dot{M} = i \cdot A/(F \cdot z), \quad 2.50$$

where $\dot{M}$ represents the mole flow of hydrogen, or oxygen, and z is the number of electrons involved in the electrochemical reactions, equal to 2 for hydrogen evolution reaction at cathode and 4 for oxygen evolution reaction at anode, as evident from Eq. 1.1 and 1.2.

The standard equation for electrode current density used in this context is the one presented by Mat *et al.* [46] and Aldas *et al.* [40].

$$i = i_o \cdot (1 - VF) \cdot exp(-F\Delta V/2RT), \quad 2.51$$

where i_o is the exchange current density, VF the volume fraction, F is the Faraday constant, ΔV the overpotential, R the ideal gas constant and T the temperature in K.

Concerning the CFD framework employed by Fluent software program, electrochemical reactions can be introduced by activating the available electrochemical module. By doing so, a mixture material, composed of the liquid and gas species of interest, can be created. Furthermore, hydrogen and oxygen evolution reactions can be imposed at the electrode walls, together with the current density, as boundary condition. For the specific case of the electrolyzer cell, the electrolyte can be defined as one of the liquid species of the liquid-gas mixture, with its material properties, e.g. density, viscosity, electrical conductivity, together with the dissolved gases and the hydroxyl ions.

The software program employs the inputs given by the user for the electrochemical reactions to solve the charge-transfer reaction of Eq. 2.52 for all the species present in the model, gas and liquid [60]:

$$\sum_{j=1}^{N} v'_{j,r} Y_j^{Z_j} \leftrightarrow \sum_{j=1}^{N} v''_{j,r} Y_j^{Z_j} + \left(\sum_{j=1}^{N} \left(v''_{j,r} - v'_{j,r} \right) Z_j \right) e^{-}, \qquad 2.52$$

where Y_j represents the liquid or gas species j, N is the total number of species, $v'_{j,r}$ and $v''_{j,r}$ are the stoichiometric coefficients of the jth species as reactant and product in the reaction r respectively, Z_j is the charge number of the jth species, e^{-} represents the electrons. Fluent makes use of the reaction at a phase level, for liquid and gas species, independently.

To calculate the volume of hydrogen and oxygen produced, Faraday's law (Eq. 2.50) is applied by the software program, employing the local value of current density defined as a constant or as a function by the user.

2.4 Thermal model

The decomposition of water is an endothermic process with a significant energy demand, as indicated by the standard enthalpy change associated with the electrolysis reaction, ΔH° = 286 kJ/mol (equivalent to 39.7 kWh/kg of H_2) [75]. At standard conditions (1 atm and 25 °C), the minimum energy required to decompose water corresponds to the change in Gibbs free energy (ΔG° = 237 kJ/mol). This energy requirement can also be expressed in terms of voltage:

$$\frac{\Delta G^{\circ}}{z_{H2}F} = \frac{237{,}000\ J}{2 \cdot 96{,}485\ C} = 1.23\ V = U^{\circ}_{rev}, \quad 2.53$$

where U°_{rev} is the reversible potential, representing the minimum energy required in the form of electricity to drive water electrolysis. The additional energy needed to reach ΔH°, the total energy demand, with corresponding voltage known as the thermoneutral potential, U°_{tn} in Eq.2.54, can be supplied as heat, $T \cdot \Delta H^{\circ}$ in Eq.2.55, if the system operates at a sufficiently high temperature:

$$\frac{\Delta H^{\circ}}{z_{H2}F} = \frac{286{,}000\ J}{2 \cdot 96{,}485\ C} = 1.48\ V = U^{\circ}{}_{tn}, \quad 2.54$$

$$T \cdot\ \Delta S^{\circ} = \Delta H^{\circ} - \Delta G^{\circ}, \quad 2.55$$

where ΔS° represents the entropy change associated with the electrolysis reaction, the total energy demand, ΔH°, varies slightly with temperature. It decreases from 286 kJ/mol at 25 °C to 283 kJ/mol at 100 °C (corresponding to a thermoneutral voltage of 1.47 V) and further to 278 kJ/mol (1.44 V) at 250 °C [76]. As temperature increases, the entropy term, $T \cdot \Delta S^{\circ}$, becomes more significant due to the entropy increase during water decomposition. This allows a greater portion of the energy to be supplied as heat, reducing the minimum electrical energy required. Consequently, the reversible potential, U°_{rev}, decreases with rising temperature, dropping from 1.23 V at 25 °C to 1.17 V at 100 °C, and further to 1.05 V at 250 °C [76].

The operating cell potential, U_{cell},, exceeds the reversible potential, U°_{rev}, due to inefficiencies such as overpotentials and resistive losses, which reduce overall efficiency. Cell potentials in advanced alkaline electrolyzers range from less than 1.8 V [77] to above 2 V. Benghamen *et al.* reported a range of 1.5 to 2.6 V for alkaline electrolyzers operating up to 200 bar [9]. These values significantly surpass the thermoneutral voltage, causing heat release during electrolysis despite its inherently endothermic nature. This waste heat, directly proportional to the difference between the actual cell potential and the thermoneutral voltage, supports maintaining the electrolysis temperature. Power dissipated as heat was characterized as in Equation 2.56, by Diéguez *et al.* [75] and Sakas *et al.* [78], following the modeling in [35]:

$$P_{cell}^{heat} = I \cdot (U_{cell} - U_{tn}), \qquad 2.56$$

where P_{cell}^{heat} is the power dissipated as heat in a water electrolysis cell working with an electric current I and a difference of potential U_{cell} between anode and cathode.

3 MULTI-PHYSICS CFD MODELING APPROACH

To perform the multi-physics simulations, ANSYS Fluent R23.1 software program was employed. In this chapter the main modeling approaches are presented, detailing which of the models described in Chapter 2 were used and under which conditions.

3.1 Eulerian model

The present research employed the Eulerian model to solve the two-phase flow. The choice is justified by the fact that electrochemical cells are characterized by a very dispersed gas. The model is described in Section 2.1.2.3.

3.1.1 Forces and turbulence

As already said in Section 2.1.2.5, the primary forces acting on the fluid of an electrochemical cell are buoyancy, drag, lift, wall lubrication, virtual mass, surface tension and turbulent dispersion. Among the possible expressions of the drag coefficient of Eq. 2.26, C_d, Ishii-Zuber approach in non-deformable conditions was employed for the simulations, chosen because more suitable for the bubbly flow and more stable from a numerical point of view, following the indications in [79]. According to Ishii-Zuber, C_d can be expressed as in Eq. 3.1 [60]:

$$C_d = \frac{24}{Re}(1 + 0.15Re^{0.687}), \qquad 3.1$$

where Re is the Reynolds number, calculated in Eq. 3.2 [60]:

$$Re = \frac{\rho_l d_b |\vec{v}_g - \vec{v}_l|}{\mu_l}, \quad 3.2$$

where μ_l is the liquid dynamic viscosity.

For what concerns the lift force, assuming that bubbles are spherical, of small size, and non-deformable, this was neglected for all the analyzed scenarios, as also indicated by the solver's guidelines [60].

Wall lubrication force was mainly implemented using the Antal *et al.* [80] model.

Finally, being the case studies mostly laminar, it was decided to omit the turbulence dispersion force. Even when introduced as user defined function, its influence was in fact found to be negligible.

The described choices are general and shared by all the case-studies. Specific details concerning the forces can be found chapter by chapter, in the modeling hypothesis sections.

The flow inside the cells is mostly laminar, apart from the case of the 1-MW electrolyzer cell, which was chosen turbulent with $k-\omega$ SST model, due to high velocities inside the cell. The turbulent modeling is described in Section 2.1.2.6.

3.1.2 Gas introduction approaches

In existing literature, CFD models commonly rely on source terms or mass-flow inlet techniques to introduce hydrogen and oxygen gas into electrochemical cells. Several studies have adopted these approaches. A mass source term was employed by Xue *et al.* [48], by Le Bideau *et al.* [43], who considered the first layer of cells adjacent to the electrode wall for introducing the gas, and by Zarghami *et al.* [37], whose layer of gas generation was taken as thick as the bubble diameter.

The volumetric source term of gas generated S_{gas} in Eq. 3.3 is directly correlated to the current density through Faraday's law (Eq. 2.50):

$$S_{gas} = i/(F \cdot z \cdot L), \quad 3.3$$

where i is the current density, $F = 96{,}487\ \mathrm{As/mol}$ is the Faraday constant and L is the length of the production layer at electrode.

Hreiz *et al.* [1] in their study consider bubble generation as an injection slightly displaced from the electrode surface. This displacement was set equal to

the bubble radius. Since their investigation uses a Lagrangian approach, the bubbles are treated as mass points in the Dispersed Phase Model (DPM), making this technique more appropriate and reasonable, as the initial position of the bubbles corresponds to their center. On the other hand, Mat *et. al* [46] and Aldas *et. al* [40] applied a boundary condition as mass-flow inlet for the gas generation, using Faraday's law to calculate the normal velocity of gas at electrodes. Finally, Rodríguez and Amores employed a segregated approach, with imposition of current density to reproduce the electrochemical behavior and a mass flux at electrodes for the fluid-dynamics modeling [27]. The main limitation of such approaches is the inherent uniformity of the gas generated that cannot consider the local bubble coverage effect, i.e. the gas curtain on the electrode constituting an electrical resistance for the cell.

Finally, as already discussed in Section 2.3, introduction of gas can be obtained through electrolysis reactions (Eq. 1.1 and 1.2) specified at the electrodes. The gas quantity is determined by the solver based on the current density, which is set as a boundary condition at anode and cathode, making use of Faraday's law (Eq. 2.50).

Compared to other methods of gas introduction, the last approach offers key advantages, such as enabling the analysis of various electrical parameters and variables (e.g., the potential field inside the cell). Additionally, it allows for a more straightforward relationship between the local current density and the gas volume fraction, considering their mutual interactions, as highlighted in Eq. 2.51.

3.1.3 Bubble diameter

The bubble diameter is generally required as an input parameter for the analysis. Therefore, a representative size of the bubbles must be prescribed to numerically solve the problem. In the Eulerian framework, bubble diameter is employed by the software to calculate the Reynolds number and the drag force.

The distribution of bubble sizes on the electrode depends on factors such as nucleation sites, surface wettability, and others. Various experimental studies ([1], [44], [63]; [71]) have shown that three main phenomena influence changes in bubble size: changes in hydrostatic pressure applied to the bubbles during their rise, the incorporation of dissolved gases in the electrolyte, and bubble coalescence. The first phenomenon is neglected as it is significant only when the operating pressure is very low. The second phenomenon is generally also neglected. Regarding bubble coalescence, flow visualizations reported by Abdelouahed *et al.* [44] and Hreiz *et al.* [1] have shown that this primarily occurs near the electrodes, but the ionic strength of the electrolyte significantly limits

this phenomenon. As a result, a significant number of bubbles retain their initial size. Therefore, this phenomenon is considered negligible, and it is assumed that there is no coalescence or bubble break-up. At higher current densities these phenomena are even less frequent. In fact, in such conditions, gas bubbles are generated more rapidly, leading to smaller, more dispersed bubbles with reduced surface instability, which minimizes the risk of breakage. Furthermore, the frequent detachment of bubbles limits coalescence, as they have insufficient time to grow and merge with nearby bubbles [81], [82], [23]. Haug *et al.* [81] measured the average bubble size as a function of current density for an alkaline water electrolyzer at 80°C with a 30% KOH aqueous solution as the electrolyte, under atmospheric pressure conditions. They demonstrated that the average bubble size at the cathode is a function of current density. For current densities between 100 and 300 A/m², the bubble diameter increases from 170 µm to 220 µm, then decreases to a constant value of 100 µm for current densities ≥1000 A/m². Operational conditions also play a fundamental role in determining the bubble diameter. In this regard, in [83], the average diameter is related to operating pressures up to 200 bar, operating at voltages of 2-3 V and currents of 0.1-0.2 A. To describe this trend analytically, the following Eq. 3.4 and 3.5 were developed [83]:

$$d_{H2} = 31.073\ p_{bar}^{-0.319}, \tag{3.4}$$

$$d_{O2} = 40.34\ p_{bar}^{-0.28}, \tag{3.5}$$

where d_{H2} and d_{O2} are the mean bubble diameters in µm for hydrogen and oxygen gas and p_{bar} is the pressure in bar.

3.2 Porosity coefficients calibration

In Computational Fluid Dynamics (CFD), when dealing with porous media, the source term that depends on porosity is typically introduced into the momentum equations to account for the additional resistance caused by the interaction between the fluid and the solid matrix. In Fluent environment the porous model is based on Forchheimer Eq. 2.43. When defining a cell zone as porous the resulting pressure loss in the flow is determined, based on the inputs provided, and added to the momentum equations, as a sink S_i for each dimension (x, y, z) [60]:

$$S_i = -(\sum_{j=1}^{3} D_{ij}\mu\, v_i + \sum_{j=1}^{3} C_{ij}\frac{1}{2}\rho|v_i|\, v_i), \tag{3.6}$$

where D_{ij} and C_{ij} are Darcy and Forchheimer prescribed matrices.

If the porous medium is uniform in the three dimensions, Eq. 3.6 is simplified to Eq. 3.7 [60]:

$$S_i = -(\frac{\mu}{\alpha} v_i + C_2\frac{1}{2}\rho|v|v_i), \tag{3.7}$$

where $1/\alpha$ is the viscous resistance coefficient and C_2 the inertial resistance coefficient. Knowing the pressure drop through the porous medium, the porous parameters can be calibrated, based on Davies Eq. 3.8 and introduced as input to the model. In particular, the coefficient values can be obtained through calibration of the Davies correlation coefficients a, a_0, b [66]:

$$\frac{dp}{dx} = -\frac{d(\Delta p)}{dx} = a(A_f\rho_f)^2(1-\varepsilon_P)^{1.5}[1+a_0(1-\varepsilon_P)^3]\mu v + b\frac{A_f\rho_f(1-\varepsilon_P)}{{\varepsilon_P}^3}\rho v^2, \tag{3.8}$$

where ε_P is the porosity of the matrix defined as in Eq. 3.9:

$$\varepsilon_P = V_v/V_{tot}, \tag{3.9}$$

where V_v represents the volume of voids and V_{tot} is the total volume of the porous matrix.

3.3 Current density function

Being the overpotential of Eq. 2.51 not accessible in the developed model, a novel function for the current density was built. As shown in Eq. 3.10, the electrical quantity i_{var} is applied to the electrodes so that it is not constant but variable, cell by cell, depending on the local gas volume fraction VF on the electrode wall, with the aim of replicating the phenomenon of bubble coverage:

$$i_{var} = i_{ave} \cdot (1 - VF)/(1 - VF_{ave}), \quad 3.10$$

where i_{ave} is the average electrode current density, imposed as a known data, and VF_{ave} the average electrode volume fraction, calculated instead by the software for each iteration. With such a function, the current density evolves iteration after iteration for each cell of the electrode wall. During the first iteration, when gas has not formed yet, the gas volume fraction is null and the variable current density, is equal to the average current density, imposed as known data, for all the wall cells. The software generates the gas phase, based on this first value of current density, through Faraday's Law, and on the electrochemical reactions imposed. When the gas starts to be produced, each wall cell presents a gas fraction, thus a value of local gas VF, which varies i_{var} function locally, iteration after iteration. The aim of this function is to maintain the overall average current density and gas production, as expected, based on the known current applied, by varying it locally, depending on the gas accumulated on the electrode. In fact, a reduced local current density is expected where the gas is more highly present, hence i_{var} decreases with the height of the cell, while having a constant average current density, dependent on the current applied.

The new approach proposed by the authors is a trade-off between the imposition of a constant current density at the electrode, and Eq. 2.51. This electrochemical method for gas generation is useful when the potential field cannot be solved for any reason (e.g. the lack of data).

No similar approach could be found in the literature when simulating an alkaline electrolyzer cell using CFD. The main approaches are, as already said, the use of a constant current density, as in [1], [48], [84] and [37], while [45], [40] and [38] employ the Butler Volmer or Tafel equations to derive the current density from the cell potential.

3.4 Thermal sources

For the present numerical study, the thermal modeling lies on the energy equation, Eq. 3.11, used by Fluent solver for both phases [60]:

$$\frac{\partial}{\partial t}\left(\rho\left(e + \frac{v^2}{2}\right)\right) + \nabla \cdot \left(pv\left(h + \frac{v^2}{2}\right)\right) \quad 3.11$$

$$= \nabla \cdot \left(\lambda \nabla T - \sum_j h_j \vec{J}_j + \bar{\bar{T}} \cdot \vec{v} \right) + S_h,$$

where e denotes the specific internal energy, h represents the specific internal enthalpy, $\vec{J}_j$ refers to the diffusion flux of species j, $\bar{\bar{T}}$ indicates the stress tensor, λ is the thermal conductivity and S_h accounts for heat sources.

Three primary energy sources were considered for the thermal modeling, which constitute the term S_h of Eq. 3.11.

The first energy source is the energy from chemical reactions, which mainly arises from the enthalpy change during the water-splitting reaction, Eq. 3.12 [60]:

$$S_R = \sum_j H_j^{\circ} \frac{\dot{R}_j}{M_j}, \qquad 3.12$$

where H_j° is the enthalpy of formation, $\dot{R}_j$ volumetric rate of creation and M_j the molecular weight of species j. The chemical reaction energy is particularly linked to the enthalpy change of the electrolysis process, during which heat is generated because of the exothermic nature of the reaction. This heat generation varies based on operating conditions like temperature and pressure and is influenced by cell efficiency.

The second energy source is Joule energy, which is related to the overpotentials at the electrodes, Eq. 3.13, obtained from [60]:

$$S_J = i^2/\sigma, \qquad 3.13$$

where σ is the electrical conductivity. Joule heating (or resistive heating) is generated due to the electrical resistance within the electrolyzer and typically plays a dominant role in thermal management due to its dependence on current flow and resistance.

Finally, the model includes the Faradaic energy, generated throughout the cell due to resistance encountered by charge carriers, Eq. 3.14 [60]:

$$S_F = i\Delta V, \qquad 3.14$$

where ΔV is the total cell overpotential. Faradaic heating arises from the energy dissipated during electrochemical reactions, thus it is closely linked to the current density and efficiency of the electrochemical reactions.

To provide an idea of the order of magnitude of such heating components, Joule heating can be up to several hundred W/m^2 and it is significantly important at higher current densities, due to its dependence on this variable squared.

4 CASE-STUDY CELLS

The CFD modeling was evaluated on different cells with growing complexity and broader multi-physics approach at each step. The methodological framework described in Chapters 2 and 3 was tailored to the cases under investigation, to meet the unique demands of each scenario:

- Literature test-case: the first study involved a simplified test-case cell characterized by extremely low current densities. Under these conditions, a streamlined modeling approach was considered sufficient. Since the system operates at ambient temperature and pressure, thermal analysis was deemed unnecessary, as temperature effects are negligible. Furthermore, constant current density imposition was applied. In fact, Eq. 3.10 was considered not necessary, due to the low current densities and consequent low gas accumulation and coverage at the electrodes.
- 1-MW EZ cell: the second application involved the cathodic half-cell of a 1 MW electrolyzer. For this case, thermal effects were not prioritized, as the emphasis lay on improving the design to enhance efficiency. Additionally, the novel, more detailed method for defining current density, Eq. 2.51, was introduced to capture bubble coverage effects.
- 50-kW EZ cell: the final simulation consisted in a 50-kW electrolyzer cell, and the mutual interaction between the two cells, connected by a semi-permeable diaphragm, was examined. The diaphragm allows liquid flow while blocking gas transfer, leading to a temperature gradient between the cells. Thermal effects became critical in this setup and could no longer be neglected. This required incorporating thermal modeling to capture the temperature distribution accurately.

The single cases will be outlined in the following subsections.

4.1 Literature test-case

The test case analyzed in this study is based on the work by Hreiz *et al.* [1], which examined the two-phase flow hydrodynamics in Vertical Plane Electrode Reactors with Gas Electrogeneration (VPERGEs) through experimental investigations and CFD analysis. The reactor operates in a No-Net-Flow Configuration (NNFC), where the liquid's free surface prevents overall liquid movement. Instead, the electrolyte circulates, while gas bubbles generated at the electrodes rise, creating upward motion along the electrodes and downward motion in the central region, forming two recirculation loops (Figure 4.1 (a)). The cell has been machined out of PMMA to allow flow visualization.

In this setup, the side plates act as anodes, producing oxygen bubbles. The electrolyte, a 0.5 M NaOH solution prepared with deionized water, is maintained at 20°C during experiments. The anodes, spaced 6 mm apart to form a narrow gap, have a submerged depth of 58 mm. Each nickel anode measures 30 mm in width and 38 mm in height and is positioned 10 mm below the liquid's free surface, fixed to supports (Figure 4.1 (c)). It is composed of seven nickel pieces bonded with epoxy resin and electrically insulated from one another by a 250 µm thick polycarbonate sheet. The reactor remained uncovered, allowing the formed gases to be freely released into the surrounding atmosphere. This cell design provides identical current density distributions over the anodes, ensuring symmetrical flow and potential conditions, which facilitates the understanding and analysis of the hydrodynamic behavior in the reactor.

Three average current densities were applied by Hreiz *et al.* [1] at the anodes: 65, 130, and 260 A/m², corresponding to the ones applied by Abdelouahed *et al.* at the cathode in a previous study [44], which was taken as a reference. For each experimental case, the applied cell voltage (supplied by a DC power source) was determined through trial and error to ensure that the average current density reached the target value.

This reactor was chosen over traditional electrolysis cells due to its excellent visualization of bubbles, making it an ideal case for study. Flow visualizations were performed using a high-speed camera to capture images from the front side of the cell. A bright LED light was used to continuously illuminate the cell from behind, with an acquisition rate of 40 frames per second. The experiments were completed within two minutes to minimize electrolyte heating due to the Joule effect, thereby limiting thermally induced convection and alterations in the medium's physicochemical properties.

Hreiz *et al.* employed a Particle Image Velocimetry (PIV) algorithm, with the dispersed bubbles acting as tracers, to calculate the gas phase's mean velocity field, providing a benchmark for validating numerical models.

It is important to note that no laser sheet was used during photo acquisition, as required in conventional PIV techniques, since laser reflections on bubble interfaces and electrode surfaces would hinder accurate velocity measurements. Instead, the calculated velocity fields represent bubble velocities, as no attempt was made to measure the liquid phase separately. Additionally, void fraction distribution was not determined through image processing due to potential measurement errors, such as bubble shadowing near the electrodes.

Flow visualization revealed that bubble curtains spread laterally as they moved upward, with bubble coalescence occurring near the electrodes both before and after detachment. However, coalescence was not a dominant phenomenon. Some bubbles however adhered to the electrodes and grew into Very Large Bubbles (VLBs).

By leveraging PIV results, the accuracy of numerical simulations could be assessed, offering valuable insights into gas-phase behavior.

The study on this test-case cell focuses specifically on the region between the anodes, where only oxygen is produced, excluding the cathode regions which are present but far from the anodes.

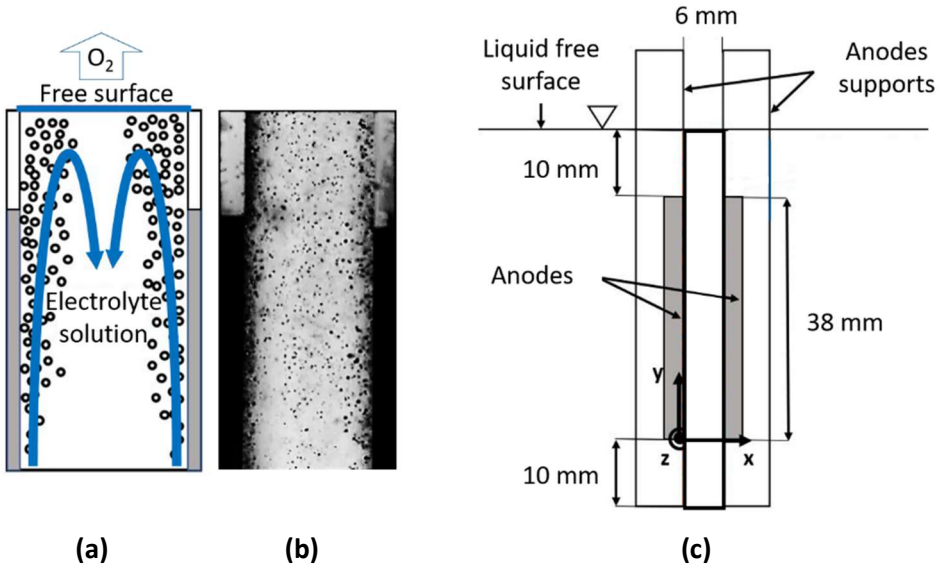

Figure 4.1: **(a)** Test-case cell two-phase behavior, **(b)** high-resolution image of bubbles [1] and **(c)** cell geometry.

Table 4.1 details the key properties of the aqueous solution (primary phase) and oxygen (secondary phase) as implemented in the software, reflecting values from Hreiz *et al.* [1].

Table 4.1: Material characteristics of primary and secondary phases.

Materials	Density [kg/m]	Viscosity [kg/m·s]
Electrolyte solution	1020	1.10e-3
Oxygen	1.30	1.91e-5

4.2 1-MW EZ cell

A 1-MW alkaline water electrolyzer designed for a nominal hydrogen production of 200 Nm^3/h at 30 bar gauge pressure was selected for the second analysis, namely the McLyzer 200-30. The cell has a zero-gap configuration featuring an anode and cathode directly placed on a diaphragm made of polyphenylene sulfide (PPS), which facilitates hydroxide ion transport while being impermeable to gases. Bipolar plates positioned on either side of the cell serve as the contact points for electrical current. Through a porous conductive layer, electrons reach the cathode, where hydrogen gas and hydroxide ions are formed via the hydrogen evolution reaction (Eq. 1.1). These ions migrate toward the anode under the influence of the electric potential, where oxygen is produced by the oxygen evolution reaction (Eq. 1.2), completing the circuit as electrons return to the anodic bipolar plate.

The disk-shaped cell operates with a 28 wt% KOH aqueous electrolyte, which enters through a bottom pipe and flows upward. Gas produced in the half-cells is collected at the top via a gas collector, while both the gas and electrolyte exit through an upper pipe. Figure 4.2 illustrates the functional scheme and key components of the system.

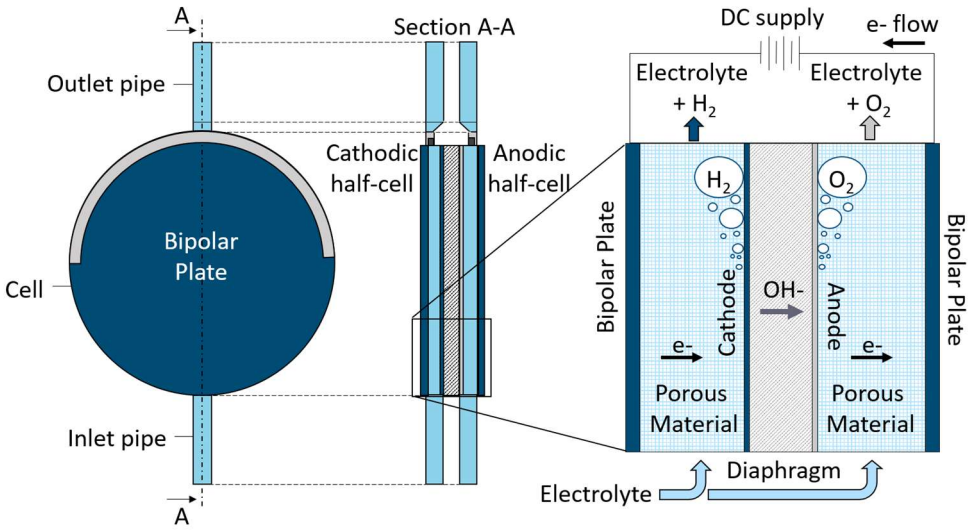

Figure 4.2: 1-MW EZ cell scheme.

This electrolyzer was chosen for its operating conditions, characterized by high current density and significant electrode volume fractions, making it a compelling case study. Working current density is between 5000 A/m^2 and 10,000 A/m^2. The system operates within a temperature range of 60-80 °C. These factors contribute to its suitability for analyzing performance under demanding conditions. Geometry optimization was also performed on this case.

4.3 50-kW EZ cell

As final case-study electrolyzer, a traditional-geometry cell was chosen, namely the PIEL H15, whose stack is capable of producing hydrogen at a maximum rate of 10 Nm³/h and operating at a pressure of 9 bar, at a power of 50 kW. The design incorporates conventional cells, where the anode and cathode are situated on opposite sides of the cell, separated by a central diaphragm that facilitates hydroxide ion transport. At the cathode, hydrogen and hydroxide ions are generated through the hydrogen evolution reaction, represented by Eq. 1.1. The diaphragm, in polyphenylene sulfide (PPS), is selectively permeable to liquids, enabling ions to migrate toward the anode under the influence of the applied potential field. Simultaneously, the oxygen evolution reaction occurs at the anode, producing oxygen and completing the electrical circuit as electrons return to the cathode, as detailed in Eq. 1.2.

The cell features a disk-shaped design, where the electrolyte, a 20 wt% aqueous NaOH solution, enters through a bottom pipe and flows upward through two separate half-cells. The gases generated in each half-cell are collected at the top through separate outlet pipes. Figure 3.3 provides a scheme of the cell highlighting the main components.

This cell was chosen for its straightforward and compact geometry, making it suitable for analysis. Nominal applied current density ranges from 1000 to 5000 A/m^2, with operating temperatures between 50 °C and 70 °C.

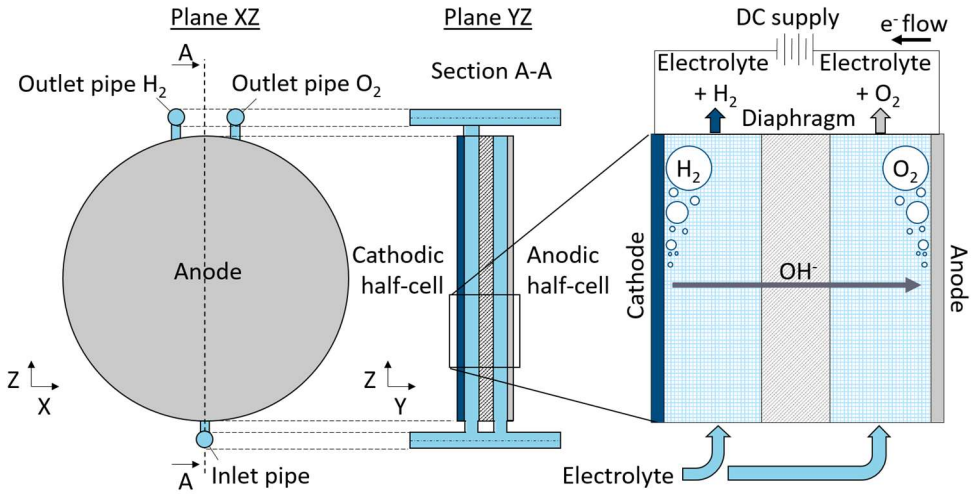

Figure 4.3: 50-kW EZ cell scheme.

4.4 Case-study electrolyzers recap

Table 4.2 and Table 4.3 detail for both case-study electrolyzers respectively the stack working conditions and materials.

Table 4.2: Working conditions of the two case-study AWEs.

Working conditions	McLyzer 200-30	PIEL H15
Operating pressure	30 bar	9 bar
Hydrogen production	200 Nm^3/h	5 Nm^3/h
Nominal power	1 MW	60 kW

Table 4.3: Materials of the two case-study AWEs.

Materials	McLyzer 200-30	PIEL H15
Electrolyte	KOH 28 wt%	NaOH 20 wt%
Electrodes	Nickel	Steel AISI 304
Diaphragm	Polyphenylene sulfide (PPS)	Polyphenylene sulfide (PPS)
Porous material	Aluminum	None

5 LITERATURE TEST-CASE: MODEL SENSITIVITY ANALYSIS AND VALIDATION

The first research activity aimed at providing a sensitivity analysis on the models and sub-models existing in ANSYS Fluent 2023 R2 for the CFD simulation of an electrochemical cell. Furthermore, the influence of bubbles diameter and source layer thickness was discussed. The model was later validated against the test-case cell from the literature described in Section 4.1, evaluating the impact of three different gas introduction methods.

5.1 Geometry and mesh

The geometry of the test-case cell described in Section 4.1 was created using Design Modeler software program, which is part of ANSYS suite, and tailored to match the specific study-case domain. To enhance stability, the domain's bottom section was extended 10 mm below the anode segments, as highlighted in Figure 5.1, where the numerical domain is specified.

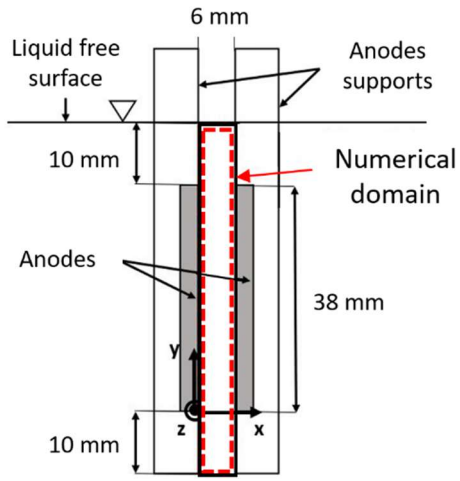

Figure 5.1: Test-case cell geometry and numerical domain.

To assess the numerical error associated with spatial resolution, a grid sensitivity analysis was conducted. The mesh resolution was determined based on the requirements of the two-phase model, specifically the ability to capture the gas bubbles size. According to Picardi *et al.* [85] the optimal ratio between the bubble diameter and grid size is $1/\sqrt{2}$. However, the present thesis proposes a novel way to build the mesh of electrochemical cells to conduct accurate simulations. In fact, a novel approach for the minimum grid resolution was employed, starting from the concept that simulations involving two-phase flows require a careful balance between the gas bubble size and the gas production layer thickness. This balance is essential for achieving a minimum grid thickness, L_{min}, at the electrode, ensuring that the simulations remain stable and physically meaningful. The relationship governing this trade-off is represented by Eq. 5.1:

$$L_{min} = MAX(d_b\ ; V_{gas}/A), \tag{5.1}$$

where d_b is the bubble diameter, V_{gas} the volume of gas generated in the first layer of cells at the electrode, and A the electrode surface area.

For this study, the minimum required layer size at the electrode was calculated to be 100 µm, being such the chosen size of the bubbles, as better highlighted in the following subsection. In this case, due to the low operational current densities, the gas production layer size was calculated in the order of 8 µm. Therefore, three mesh cases were considered, a “Coarse” one, with

minimum layer thickness of 200 µm and a total of 150,000 elements, a "Medium" case, of 130 µm and a total of 300,000 elements, and a "Fine" case, with minimum layer thickness of 100 µm and a total of 350,000 elements. Eventually, the average case was chosen, ensuring the robustness of the results. The gas vertical velocity trend for the three cases is displayed in Figure 5.2.

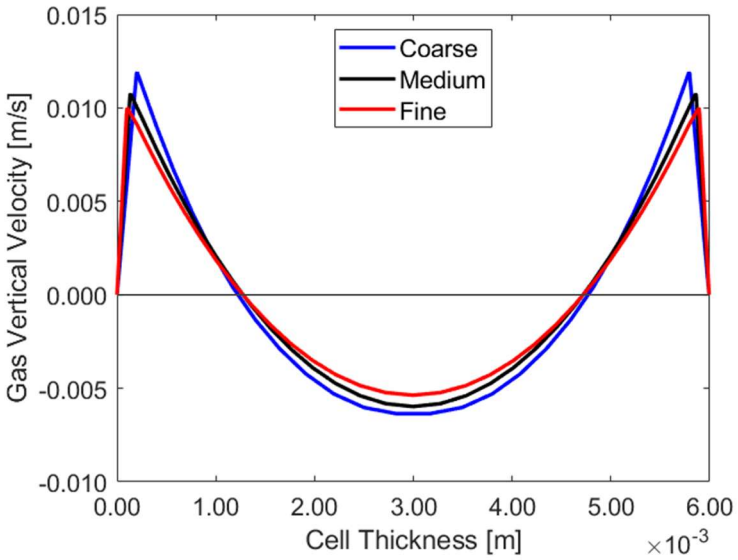

Figure 5.2: Test-case cell mesh sensitivity analysis.

In Figure 5.3 a mesh detail of the test-case cell domain is displayed. The inlet and outlet zones, preceding and following the cell, are visible from the image.

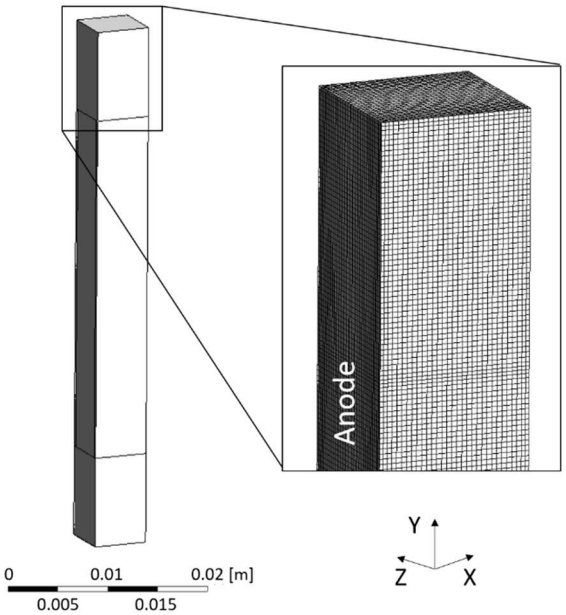

Figure 5.3: Test-case cell mesh detail.

5.2 Modeling hypotheses

The two-phase Eulerian model was adopted to account for the dispersed nature of the bubbles, with the following assumptions:

- Pressure is uniform and set to atmospheric value for both phases.
- The flow is characterized as Newtonian, incompressible, and viscous.
- The system is considered isothermal, with a temperature of 20 °C, consistent with the experimental conditions [1].
- Due to the low flow velocities, the flow is laminar, and pressure gradients are negligible.
- Bubbles are treated as constant in size, spherical in shape, with a diameter of 0.1 mm, to match the average size as found by the experimental measurements [1]. For the sensitivity analysis other diameter values were taken into account, but always kept constant during the simulation. In the Eulerian framework, bubble diameter is employed by the software to calculate the Reynolds number and the drag force.
- Bubble coalescence and breakage phenomena are neglected.
- A stationary no-slip wall is assigned to the anodes, and a degassing condition used as outlet boundary condition.

5.2.1 Forces

As described in Section 2.1.2.5, the force which mostly influences the motion of the bubbles inside the cell is the buoyancy force, due to the high difference of density between the electrolyte and the oxygen, respectively 1020 kg/m³ and 1.30 kg/m³. The other forces to be implemented in the model are drag, lift, wall lubrication and virtual mass force. Turbulent dispersion force was omitted, due to the laminar conditions of the cell flow.

Among the possible expressions of drag force, three of them have been considered in the current study: Schiller-Naumann, Morsi-Alexander and Ishii-Zuber. The first two approaches consider a rigid, spherical shape of the bubbles, coherently with our test case. In fact, the visualization of the flow in [1] shows that the bubbles are not deformed. On the other hand, the formulation of Ishii-Zuber is more complete and suitable for a boiling flow like the one studied. Having conducted simulations with the three forms of drag force without significant difference in the output, the choice has finally fallen on the Ishii-Zuber expression. To enable the use of this model, it is necessary to indicate the surface tension, considered equal to the one of water at room temperature, 72 mN/m.

Coming to the lift force, the solver's guidelines suggest that its inclusion can be helpful when having large bubbles [60]. Since in our case only small bubbles have been considered, lift force can be neglected so as not to put extra complications to the system.

As for the wall lubrication force, Tomiyama and Frank approaches are suitable for flows inside pipes [60], whereas Hosokawa takes by default the wall lubrication coefficient of Tomiyama and its manual characterization is not straightforward and adds complexity to the model. On the other hand, the study case is not a pipe flow, thus the only possible choice was the Antal formulation. Wall lubrication coefficients, C_{w1} and C_{w2}, default values, namely 0.01 and 0.05, were used.

Coming finally to the virtual-mass force, a constant coefficient of 0.5 was chosen to simplify the CFD code, corresponding to spherical shape of bubbles.

5.2.2 Gas introduction approaches

The three methods described in Section 3.1.2 for introducing the gas were evaluated for validating the model. The first approach involved applying a mass source term within a thin layer adjacent to the electrode. The three different values of current density employed for the experimental setup were considered,

i.e. 65, 130, and 260 A/m². The oxygen gas introduced depends on the current density as for Eq.3.3.

The second approach used mass-flow inlets at the electrodes. Given the minimal gas production, the mass flux impact on the velocity field perpendicular to the electrode was negligible, making this approach valid.

Finally, the third method consisted in defining the electrochemical reactions at the electrodes, oxygen evolution reactions in this case as in Eq. 1.2, with a constant current density. Due to the low volume fraction of gas, applying a law to account for bubble coverage, as with Eq. 3.10, was considered unnecessary in this case.

5.3 Results

The results of Sections 5.3.1 and 5.3.2 were obtained by using the mass source approach. The bubbles were introduced as a mass source term inside two narrow mesh regions, defined as two near wall layers of 0.4 mm of thickness in correspondence with anodes. Concerning Section 5.3.3, mass source term was used and the layer size was varied for the evaluation of its impact. Finally, in Section 5.3.4 the three gas introduction methods described in Section 5.2.2 were tested against the experimental output.

5.3.1 Current density

To evaluate the accuracy of the model, the main parameter considered was the mean bubbles y-velocity field in the mid-section, that is the velocity of the gas flow in the vertical direction. This output was compared with the gas velocity fields that Hreiz et al. [1] were able to obtain by use of a PIV algorithm. Three different cases of current density have been studied: Figure 5.4, Figure 5.5 and Figure 5.6 show the velocity fields with current densities of 65, 130 and 260 A/m², respectively.

Qualitatively speaking, the bubbles curtain with growing thickness was reproduced numerically. However, the gas spreading to the central part of the cell is less evident than the experimental measurements. Quantitatively speaking, instead, the maximum values of velocity are close to the ones obtained experimentally. The applied current densities of 65, 130 and 260 A/m² gave maximum y-velocities of 16, 22, 29 mm/s, respectively. These numbers are consistent with the ones obtained by Hreiz *et al.* with PIV method [1] apart from

the third case (260 A/m²) which gave higher velocities than the experimental results.

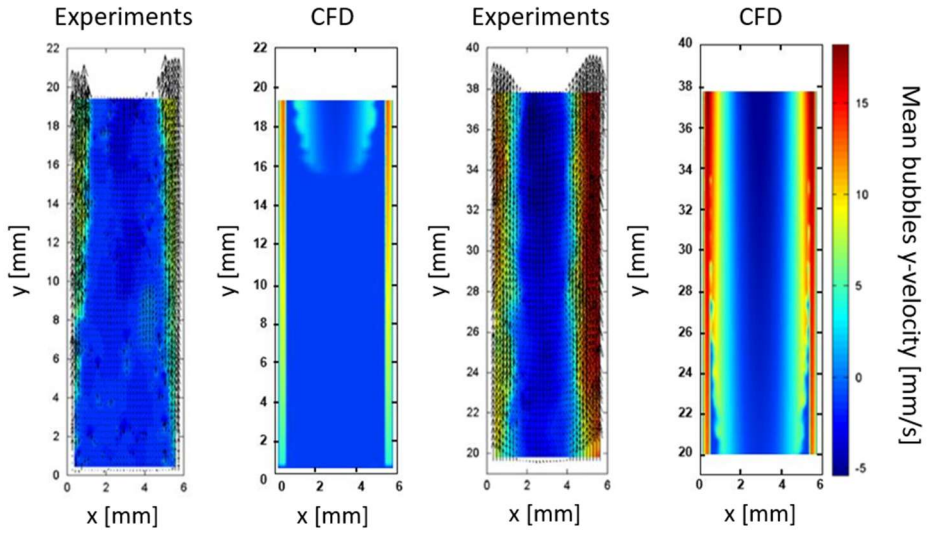

Figure 5.4: Mean y-velocity contour plots: on the left PIV output [1], on the right numerical results, 65 A/m^2. **(a)** Bottom half of the cell, for 0 ≤ y ≤ 19 mm. **(b)** Top half of the cell, for 19 ≤ y ≤ 38 mm.

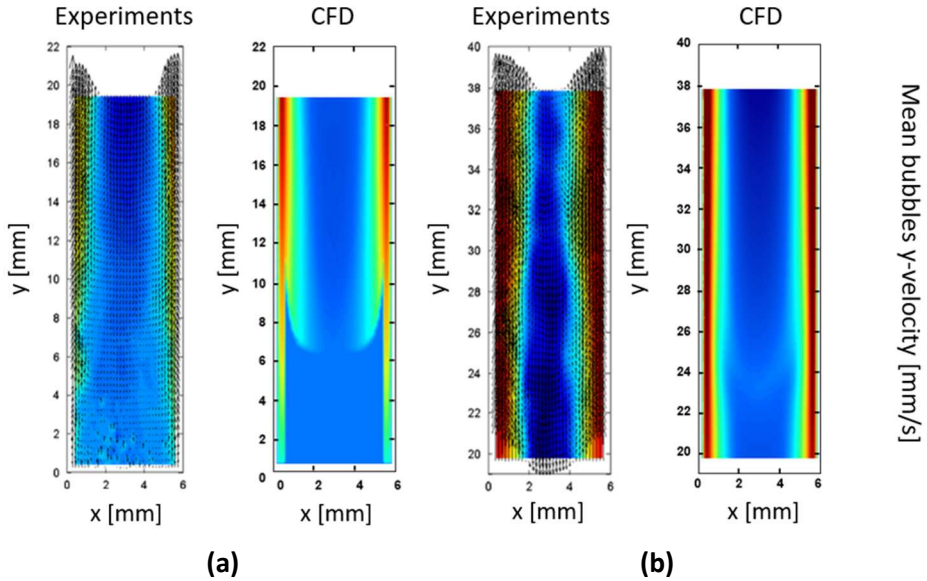

Figure 5.5: Mean y-velocity contour plots: on the left PIV output [1], on the right numerical results, 130 A/m^2. **(a)** Bottom half of the cell, for 0 ≤ y ≤ 19 mm. **(b)** Top half of the cell, for 19 ≤ y ≤ 38 mm.

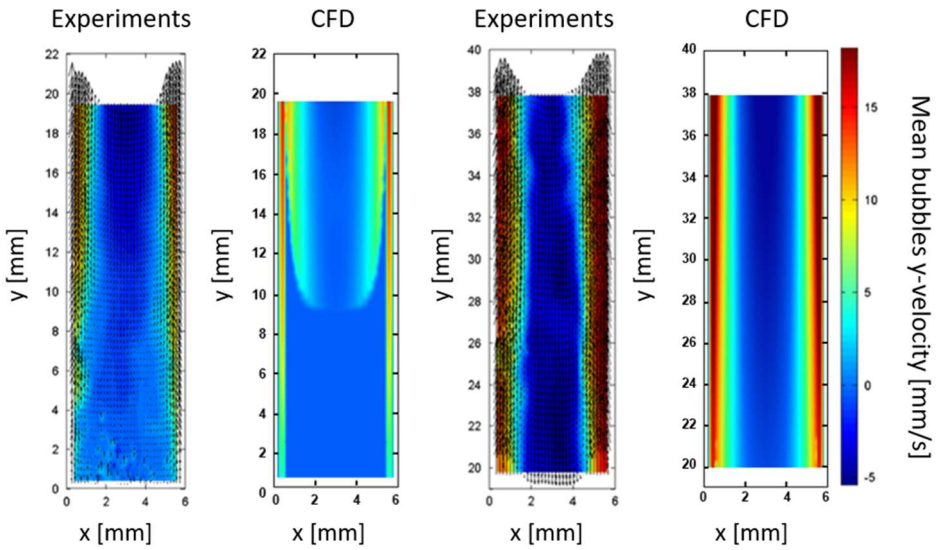

(a) **(b)**

Figure 5.6: Mean y-velocity contour plots: on the left PIV output [1], on the right numerical results, 260 A/m^2. **(a)** Bottom half of the cell, for 0 ≤ y ≤ 19 mm. **(b)** Top half of the cell, for 19 ≤ y ≤ 38 mm.

5.3.2 Bubble diameter

The effect of varying the bubble size was examined for the condition of 130 A/m². Two smaller bubble diameters, 60 µm and 75 µm, were initially tested, both smaller than the experimentally measured average of 100 µm. As already discussed in

The results showed that the flow behavior depended on the bubble size, with the length of the recirculating cells being proportional to the bubble diameter. For the 60-µm case, six shorter vortices were observed (Figure 5.7 (a)). In the 75-µm case, three intermediate-length vortices were present (Figure 5.7 (b)), while the 100-µm case resulted in a single, elongated recirculating cell (Figure 5.7 (c)). This pattern can be attributed to the maximum vertical velocity (y-velocity), which increased with bubble size: 15 mm/s for 60-µm bubbles, 18 mm/s for 75-µm bubbles, and 22 mm/s for 100-µm bubbles. As expected, larger bubbles

generated higher velocities due to increased buoyancy forces, whereas lower velocities were associated with more frequent recirculating flows.

The impact of larger bubbles was then analyzed by increasing the diameter from 100 µm to 150 µm. This change aimed to approximate the influence of Very Large Bubbles (VLBs), about 1 mm in size, which significantly affect gas curtain spreading toward the cell's interior. However, as observed experimentally [1], VLBs are relatively rare. Consequently, the bubble diameter was increased by 50%, resulting in bubbles with a volume 3.3 times larger than the default model setting. Notably, the model assumes uniform bubble shapes.

The results for 150-µm bubbles are shown in Figure 5.7 (d), alongside the other diameter cases. Larger bubbles enhanced the vertical spreading and thickening of the gas curtain. However, they failed to produce the characteristic recirculation patterns seen in PIV measurements, highlighting a limitation of the uniform bubble shape assumption in accurately simulating flow dynamics.

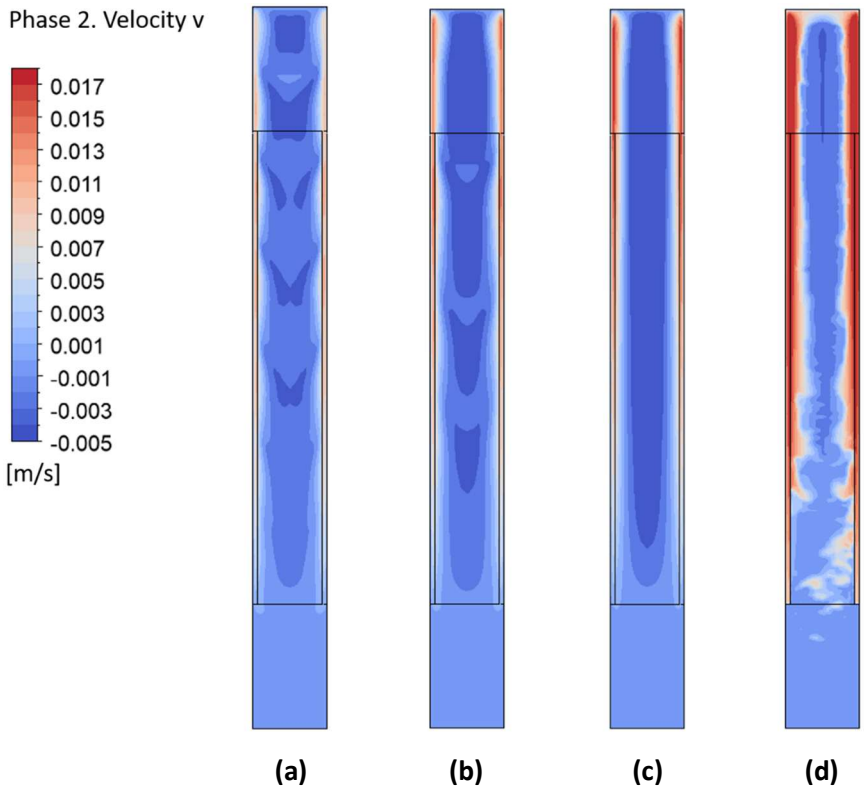

Figure 5.7: Gas vertical velocity in the cell mid-plane. Bubbles diameter: **(a)** 60 µm, **(b)** 75 µm, **(c)** 100 µm, **(d)** 150 µm

In conclusion, the 100-µm case represents the best trade-off for the present model, allowing a gas diffusion and a downward recirculation consistent with experimental results. As a matter of fact, this value is in-line with the measurements of the bubble diameter, as described above.

5.3.3 Source layer thickness

A sensitivity analysis was then conducted to determine the optimal thickness of the layer where the mass source term is introduced. Four configurations were tested with a fixed current density of 130 A/m², using source layer thicknesses of 0.1, 0.2, 0.4 and 0.8 mm. Figure 5.8 presents the resulting y-velocity fields across the computational domain.

The 0.1-mm case exhibited more instability compared to the others, with frequent vortices within the gas flow. Additionally, the bubble curtain achieved lower y-velocity values than those observed in experimental measurements [1]. The negative velocities associated with the recirculating electrolyte were also lower than expected, leading to the exclusion of this configuration. For the 0.2-mm case the recirculation pattern in the lower half of the cell appeared weaker than the PIV results Specifically, the downward flow stalled at a height of 15 mm rather than extending further down.

The 0.4-mm and 0.8-mm cases provided better alignment with experimental data in terms of recirculation patterns. However, the 0.8-mm configuration deviated in the upper part of the cell, where the gas curtain induced a stronger recirculation than the one observed experimentally. Consequently, this configuration was also deemed unsuitable.

The 0.4-mm case showed the best overall agreement with experimental data, confirming its validity. This analysis underscores the significance of selecting an appropriate geometry for the source layer to accurately simulate the flow dynamics. Having for the present case a constant bubble diameter of 0.1 mm, we can conclude that a source layer around four times the bubble size can be considered as the most appropriate to simulate the two-phase flow inside electrolyzer cells.

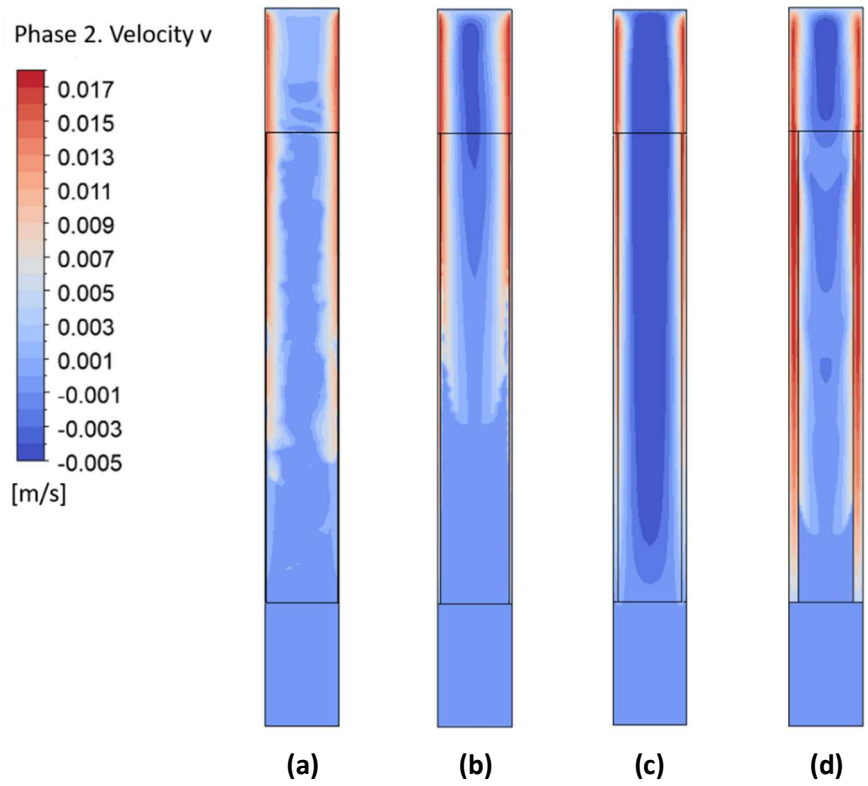

Figure 5.8: Gas vertical velocity in the cell mid-plane. Source layer thickness: **(a)** 0.1 mm, **(b)** 0.2 mm, **(c)** 0.4 mm, **(d)** 0.8 mm

5.3.4 Gas introduction methods

The three gas introduction methods described in Section 5.2.2 were tested against the experimental output obtained by Hreiz *et al.* [1] at a current density of 130 A/m², as shown in Figure 5.9.

Among the tested approaches, the mass-flow inlet method produced the highest maximum velocities compared to experiments, which recorded a peak velocity of approximately 0.018 m/s. Gas introduction via a source term resulted in a maximum velocity closer to the experimental values, while the electrochemical module yielded slightly lower velocity magnitudes. Despite the smaller alignment of the electrochemical method with experimental measurements, its application is deemed more physically representative.

It is also worth noting that larger bubbles, which were excluded from the simulations, can significantly influence local turbulence and velocity diffusion. Experimental observations by Hreiz *et al.* [1] indicate the presence of bubbles up

to 1 mm in size near the electrodes, which likely contribute to these effects, as evident from their images and video recordings.

The findings are also reported in the chart of Figure 5.10 where the gas vertical velocity at a cell height of 30 mm are displayed. In the chart three points regarding the experimental output are also shown. The overall measurement trend could not be obtained, since precise data are not available from [1]. However, the velocities corresponding to the maximum and minimum values are indicated. The volumetric source approach performed better regarding the maximum velocity values. However, the electrochemical method appears to better align with the minimum velocity, which is associated with recirculation. Again, mass flow inlets approach gave an exaggerated fluid velocity, compared with measurements.

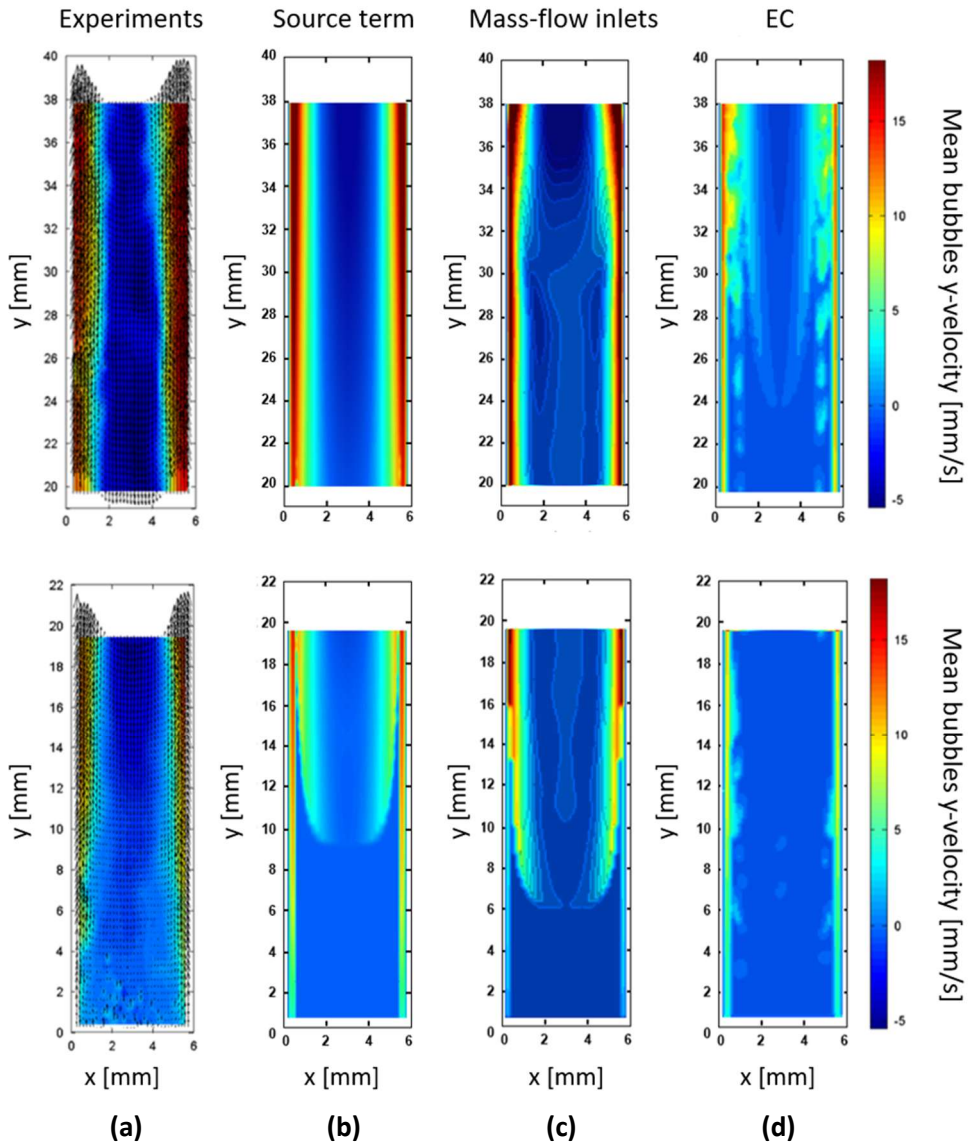

Figure 5.9: Mean gas y-velocity contour plots of test-case cell for i=130 A/m^2. **(a)** PIV output from experimental results [1]. Introduction of gas by means of **(b)** source term, **(c)** mass-flow inlets and **(d)** electrochemical (EC) reactions.

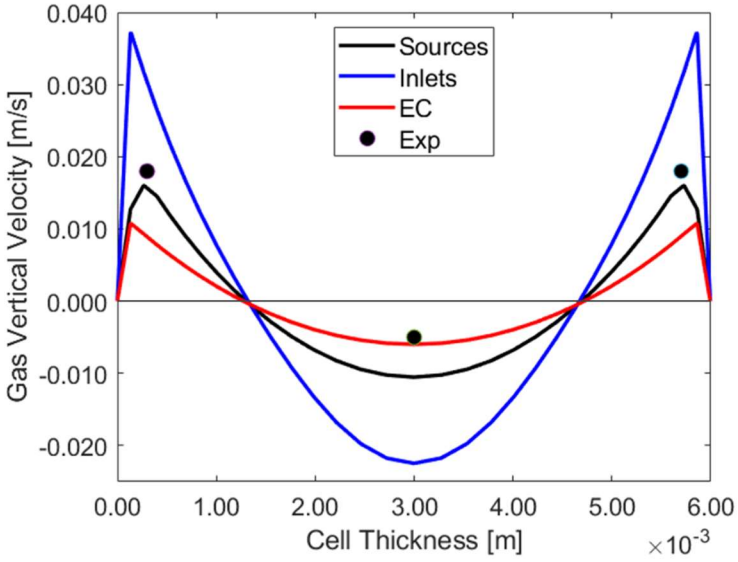

Figure 5.10: Gas vertical velocity for the three gas introduction methods at 30 mm cell height for *i*=130 A/m^2, compared with experiments

5.4 Discussion

A sensitivity analysis on the main modeling choices was performed. Starting from the introduction of the gas as a source term, the output was compared to PIV measurements of the vertical mean bubbles velocity showing good agreement in maximum values, for the three conditions in terms of current density.

The influence of the bubble dimension on the model was then evaluated. In addition to the 100-µm case, two smaller and a larger diameter were chosen, namely 60, 75 and 150 µm. A growing number of recirculating cells was noticed as the bubble diameter decreases, likely due to the lower velocities of the gas. The bigger size of the bubbles showed instead a noticeable influence with respect to the diffusion of the gas towards the inner part of the cell. On the other hand, downward velocities differed from experimental measurements and the 100-µm case was assessed to be the most consistent with PIV results.

The impact of the source layer size was studied, considering four different cases of thickness, namely 0.1, 0.2, 0.4 and 0.8 mm. The conclusion of this analysis is that the definition of the source layer size is crucial and needs to be calibrated depending on the expected gas volume fraction. A comparison with the experimental results confirmed the suitability of a 0.4-mm layer thickness

for the present model, indicating that, in general, a layer size approximately four times the bubble diameter is appropriate.

Finally, the three gas introduction methods were evaluated and compared to the experimental output. The best fit by comparison to the experimental results from literature was obtained for the case of gas introduction through source term. Use of gas fluxes at the electrodes determined instead higher vertical velocities, while the use of the electrochemical module had a lower resemblance to measurements. However, the physical significance of the last approach was considered noteworthy, together with the possibility of evaluating electrical parameters, otherwise absent. Furthermore, the minor gas dispersion found for the electrochemical case was considered valid, as expected to be more significant for real-case electrolyzers. Qualitatively speaking, the thickening of the bubbles curtain was in general slightly underestimated by the numerical setup and future research may need to include the turbulent dispersion effect on the bubbles and a proper population balance modeling (PDM) to account for different bubble dimensions.

6 SIMPLIFIED 1-MW EZ CATHODIC CELL: SIMULATION AND SENSITIVIY ANALYSIS

The first study regarding a real-cell geometry focused on applying the multi-physics numerical setup on a cathodic half-cell. To further lower the computational costs, a 2.5D sector of a 1-MW electrolyzer real-scale cell, described in Section 4.2, was modeled. The velocity and volume fraction behaviors at the cathode for various current density values, ranging from 1000 to 10,000 A/m² were studied. Finally, sensitivity analyses were conducted to identify which is the impact of different electrolyte mass flow rates and current densities on the cell. Special attention was dedicated to the impact of gas accumulation on the electrode, by introducing the new current density function (Eq. 2.58), with dependence on the local volume fraction.

6.1 Geometry

The simplified cathodic cell geometry considered for the analysis is illustrated schematically in Figure 6.1. It was built using Design Modeler software program, which is part of ANSYS suite. As can be seen from Figure 6.1, the numerical domain is included in the cell section ranging from the bipolar plate to the cathode.

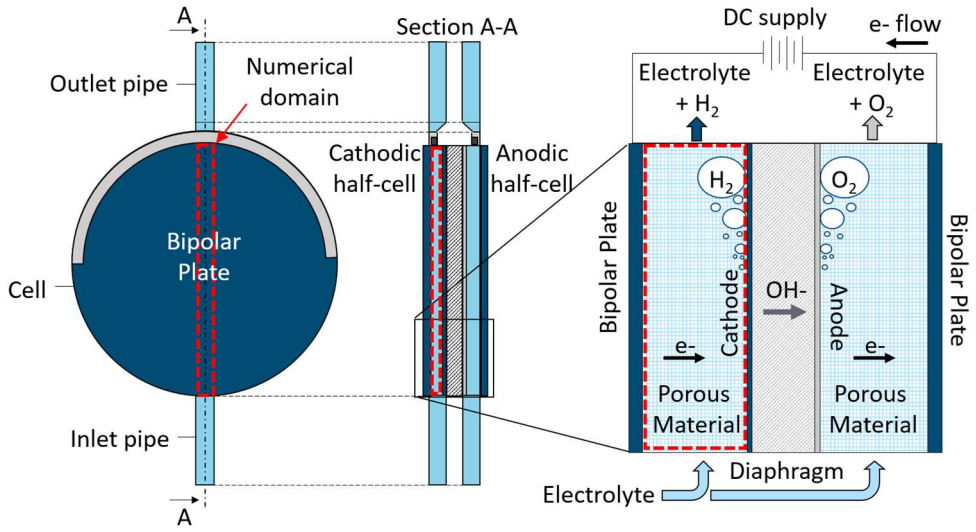

Figure 6.1: 1-MW EZ cell scheme and numerical domain.

6.2 Mesh

A hexahedral mesh of the domain was developed with significant refinement near the cathode, and a grid independence test was conducted, following the approach described in Section 5.1. The bubble diameter in this scenario was set to 10 µm, as explained in Section 6.3, whereas a calculation of the local gas volume revealed that a minimum mesh size of 40 µm was necessary to ensure that the cell volume was not smaller than the amount of gas generated at the electrode. Therefore, four mesh refinement cases, ranging from a 75-µm to a 200-µm minimum cell size at the electrode, were selected, as detailed in Table 6.1, which summarizes the layer thickness and total number of cells for each refinement scenario.

Table 6.1: Features of the selected mesh sensitivity cases.

Mesh features	Mesh 1	Mesh 2	Mesh 3	Mesh 4
Layer size [µm]	75	100	150	200
Number of cells [-]	3E5	2E5	2E5	1.5E5

Figure 6.2 shows the results for gas volume fraction (VF) and vertical velocity across the four mesh sensitivity cases. The 75-µm case, i.e. “Mesh 1”, showed a strong discrepancy of flow behaviour compared to the others, maybe because of a too severe refinement, whereas the coarser cases exhibited nearly identical results regarding volume fraction and velocity. Thus, “Mesh 2” was ultimately chosen as it provided sufficient accuracy.

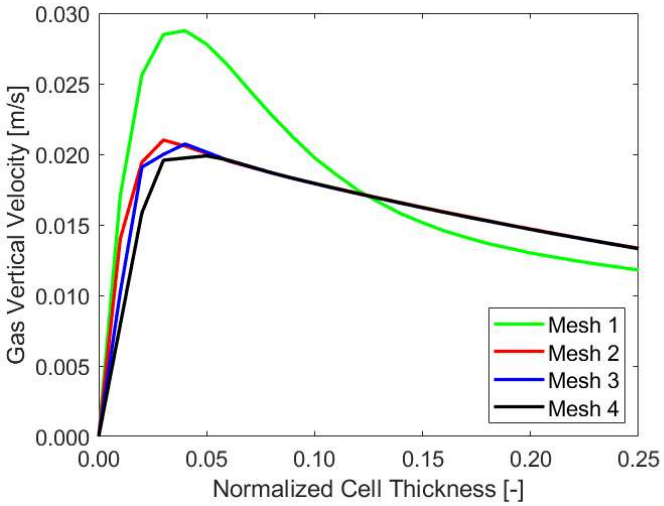

(a)

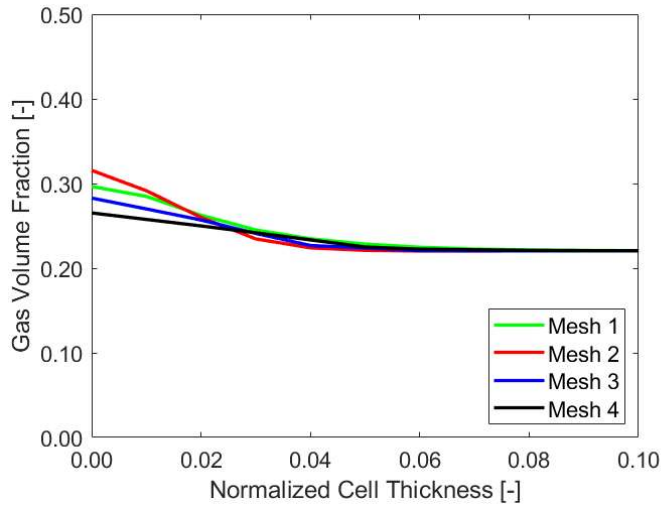

(b)

Figure 6.2: Mesh sensitivity analysis: **(a)** gas vertical velocity and **(b)** *VF* along the cell thickness.

Figure 6.3 shows a detailed view of the mesh in the cathodic cell section, providing insight into the mesh refinement applied at the cathode.

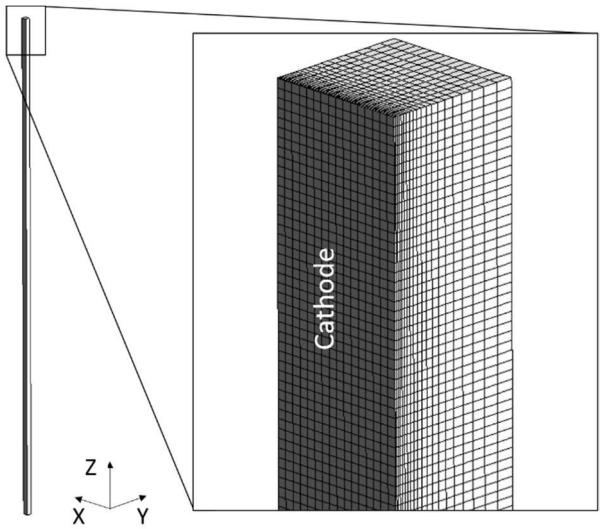

Figure 6.3: 1-MW EZ cathodic half-cell section mesh detail.

6.3 Modeling hypotheses

The general two-phase and electrochemical numerical modeling follows the setup described in Chapter 3, with the following specific assumptions for the case-study:

- Inlet temperature and operating pressure were set to 60 °C and 30 bar, in alignment with the actual operating conditions of the system. Isothermal conditions were chosen and the thermal modeling not applied, for simplification purposes.
- Primary phase is a 28 wt% KOH solution in water, and the secondary phase is hydrogen.
- The flow regime was defined as turbulent, using the $k-\omega$ SST model with low Reynolds number correction, as the flow velocities are higher compared to the no-net flow cell, given the recirculating electrolyte.
- The bubble diameter for hydrogen was set to 10 µm, ten times smaller than the diameter in the validation case, due to the higher operating pressure, and obtained making use of Eq. 3.4.
- The same forces described in Section 5.2.1 were employed for the model.

- Surface tension was taken as 60 mN/m, corresponding to water's surface tension at the specified pressure and temperature.
- Turbulent dispersion force was not considered, since its inclusion could not be validated within the test-case cell and therefore calibration of such force is absent in the present thesis.

Concerning the boundary conditions, a pressure-outlet condition was applied at the outlet, while at the inlet an electrolyte mass flow was imposed, calibrated to match the gas volume fraction observed at the outlet for the real cell. Both constant and variable current densities were employed, with the latter governed by Eq. 3.10.

6.4 Results

The CFD model, incorporating the electrochemical approach, was applied to the 2.5D sector, enabling a sensitivity analysis of the key variables. Initially, the novel equation for current density, outlined in Eq. 3.10, was compared with a constant current density case. This was done for three different current density values: 1000, 5000, and 10,000 A/m^2, to assess their impact on gas vertical velocity and volume fraction. Next, the 5000-A/m^2 case was used to investigate the effects of varying the electrolyte flux at the inlet. This involved analyzing scenarios with half and double the nominal mass flow rates.

6.4.1 Impact of constant and variable current densities

With the implementation of Eq. 3.10, the current density imposed at the electrode is not uniform and equal to the average current density, but it locally depends on the gas VF at the electrode. Based on this function, the overall average current density and gas production remain the same, as the ones desired and expected for the applied current.

Thus, following the Eq. 3.10, the local current density decreases with height, with a behavior opposite to the volume fraction, which increases with height, as illustrated by the contours of Figure 6.4. Instead of being imposed as a constant value, current density is in fact calculated by the software, iteration after iteration for each cell.

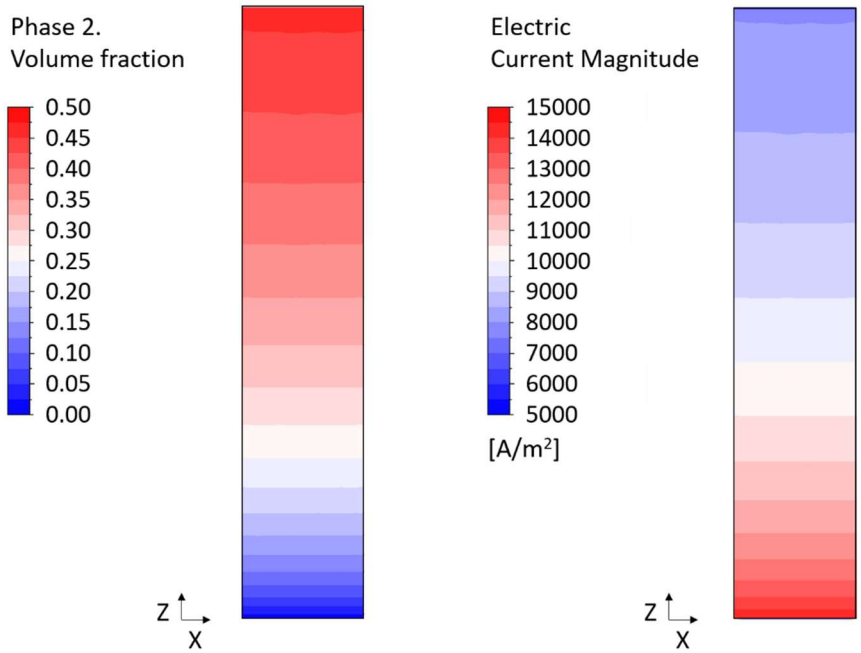

Figure 6.4: Gas **(a)** *VF* and **(b)** current density at electrode, i_{ave}=10,000 A/m^2.

The influence of this new current density expression was compared to a constant current density scenario, and the values along the cell height are reported in the graphs of Figure 6.5 (a). Gas VF and vertical velocity at the cathode are reported in Figure 6.5 (b), where it is highlighted the difference of using a constant or a variable current density. A line 100 µm away from the electrode, was used to evaluate the velocity profile.

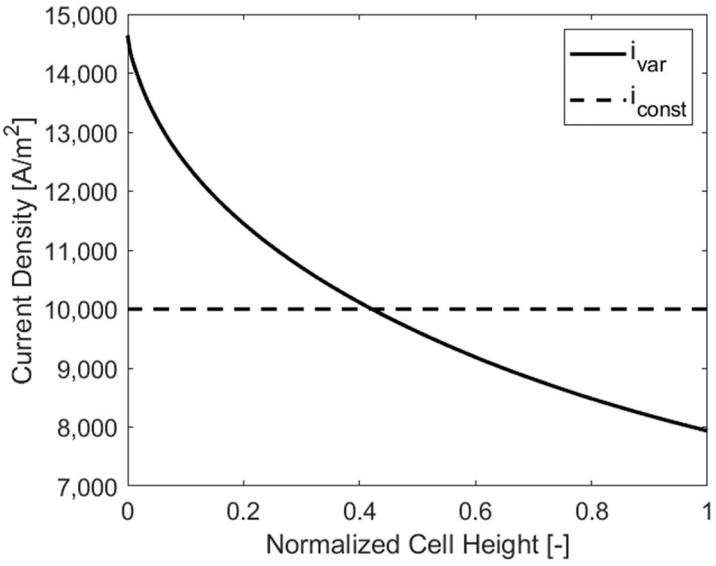

(a)

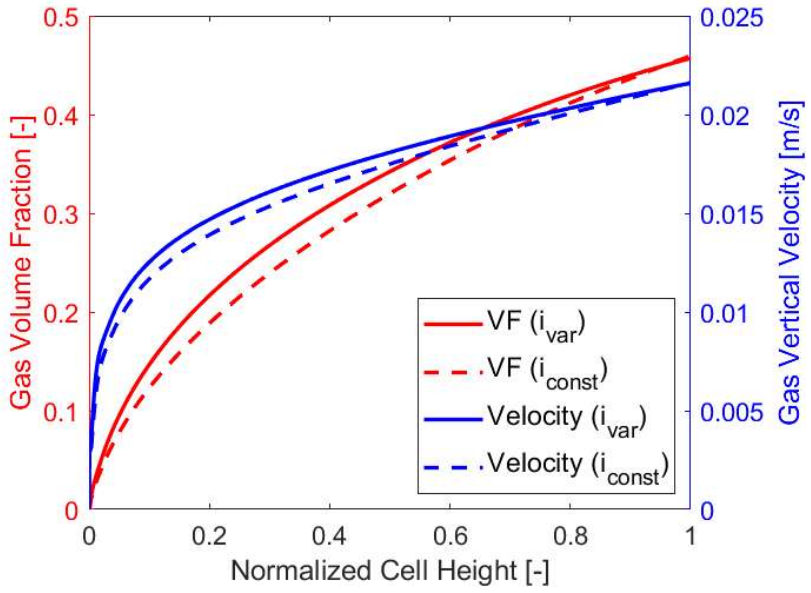

(b)

Figure 6.5: **(a)** Electrode current density along the cell height for constant (i_{const}) and variable (i_{var}) current densities, i_{ave}=10,000 A/m^2. **(b)** Gas *VF* and vertical velocity along the cell height for constant (i_{const}) and variable (i_{var}) current densities, i_{ave}=10,000 A/m^2.

The effect of the variable current density, in contrast to the constant current density, is evident in the gas vertical velocity and VF profiles, particularly in the lower portion of the cell. In the first quarter of the cell height, both gas velocity

and volume fraction are, on average, approximately 10% and 20% higher, respectively, compared to the constant current density case. The output is physically consistent, since it indicates increased hydrogen production in the bottom part of the cell due to higher absorbed current density, where the bubble coverage is lower, leading to local larger gas VF and vertical velocities.

These findings confirm that using a variable current density approach is numerically more accurate than applying a constant current density, as it accounts for the mutual influence of the gas volume fraction on the local current density.

6.4.2 Current density sensitivity analysis

In this section, the average current density is changed, aiming to show how the distributions of current density and gas VF vary with changes in the average current value. In the previous paragraph, it was noted that the distribution obtained as the output of the calculation depends on the local resulting distribution of gas VF, which in turn depends on the current density, due to Faraday's Law.

The use of three different average current densities resulted in the graph shown in Figure 6.6, illustrating the relationship between current density and gas volume fraction. These quantities were normalized by the average electrode gas volume fraction and electrode current density to better highlight the relative trend variations when hydrogen production decreases. The chart clearly shows that the variable current density function has a greater impact when the average current density is higher. Table 6.2 reports the average gas volume fractions at the outlet and electrode for the three cases studied. The ratio between these values can serve as a key performance indicator for the cell design based on CFD simulations. A ratio greater than 1 indicates a higher amount of gas accumulation, as the average gas volume fraction at the outlet is lower than at the electrode.

Table 6.2: Outlet and electrode average gas volume fraction values and their ratio.

i_{ave} [A/m²]	VF_{ave} [-]	VF_{out} [-]	VF_{ave}/VF_{out} [-]
1000	0.08	0.05	1.60
5000	0.21	0.22	0.95
10,000	0.32	0.37	0.86

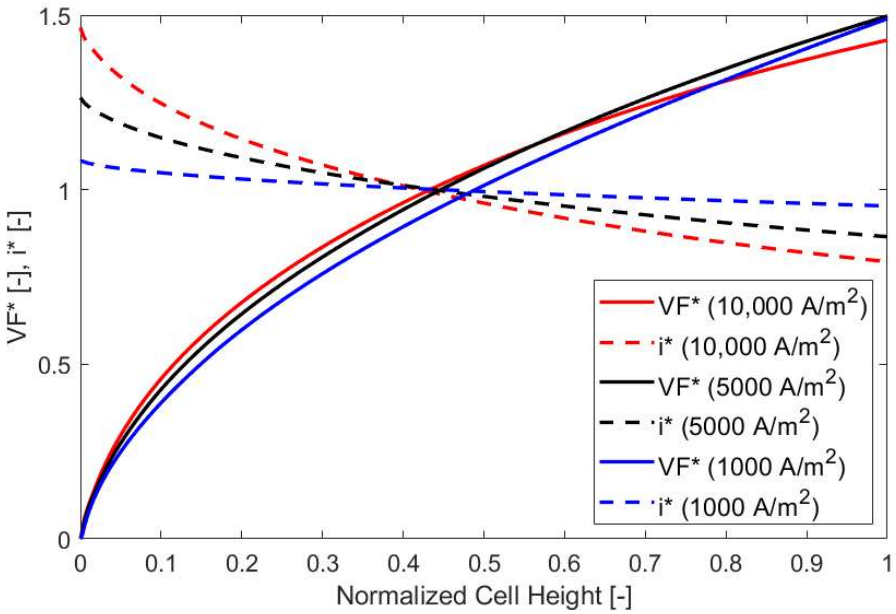

Figure 6.6: Normalized values of current density (*i**) and volume fraction (*VF**) for i_{ave}=1000/5000/10,000 A/m², as a function of cell height.

To give an idea of the gas VF and velocities inside the cell, the contours of such variables for a section perpendicular to the electrode (YZ in Figure 6.3) are reported in Figure 6.7. The case with average current density of 10,000 A/m² was chosen for this analysis. The gas velocity, displayed in Figure 6.7 (a) clearly decreases away from the electrode, on the left, whereas the volume fraction, in Figure 6.7 (b), remains constant after a first abrupt decline. The peaks of velocity correspond to the buoyancy effect given by the gas production.

Two locations were selected for a more precise characterization of the variables, i.e., two central lines at a quarter and three quarters of cell height, marked in black in the contours of Figure 6.7. The trends of gas vertical velocity

and volume fraction for the three values of average current density along the two lines are reported in the charts of Figure 6.8. Both VF and velocities clearly increase with the current density.

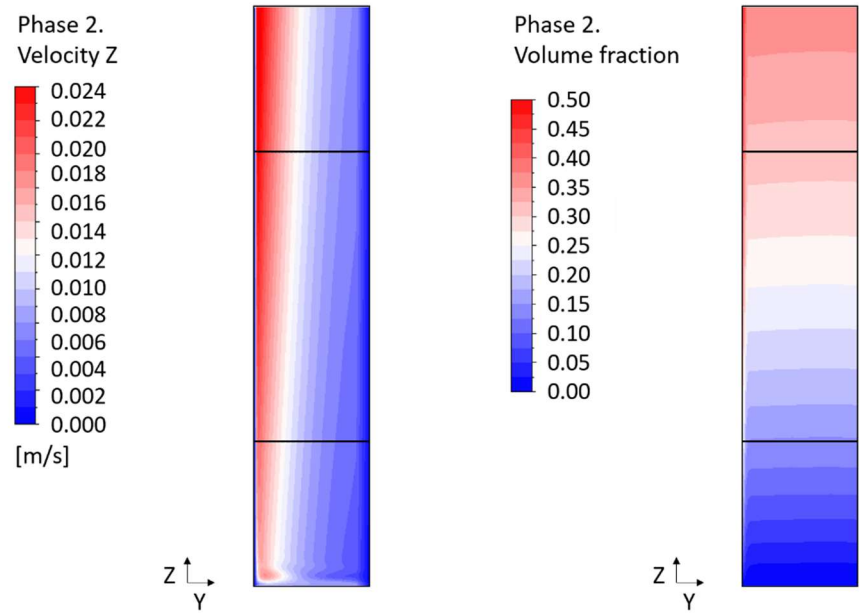

(a) **(b)**

Figure 6.7: Gas **(a)** vertical velocity and **(b)** *VF* at YZ section, i_{ave}=10,000 A/m^2.

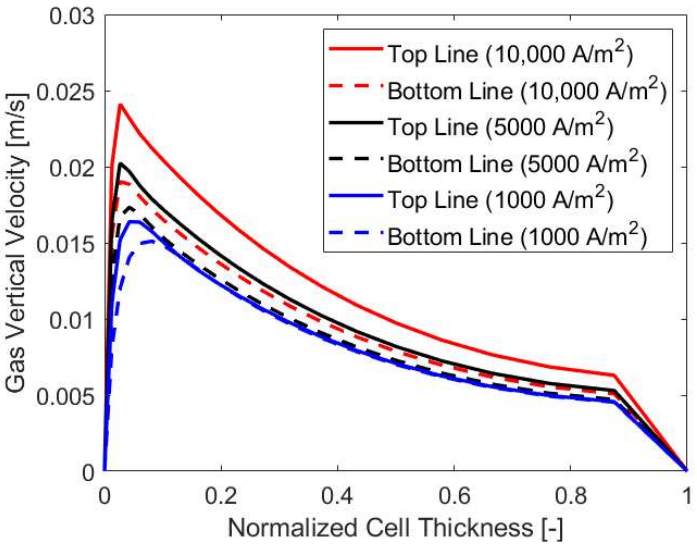

(a)

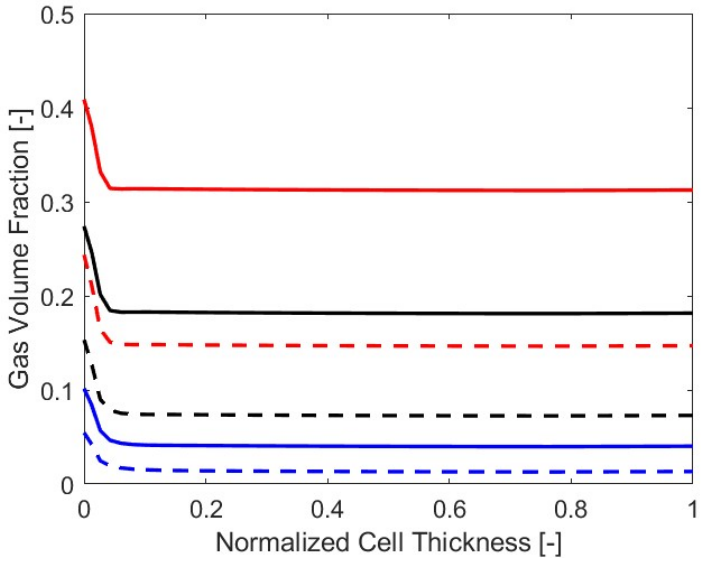

(b)

Figure 6.8: Gas **(a)** vertical velocity and **(b)** volume fraction along the thickness of the cell for i_{ave}=1000/5000/10,000 A/m², at a quarter and three quarters of cell height.

6.4.3 Electrolyte mass flow rate sensitivity analysis

For the sensitivity analysis of the electrolyte mass flow rate, three different fluxes were tested: one at half the nominal flow rate, one at double, and one at the nominal value. The trends for gas vertical velocity and volume fraction at an average current density of 5000 A/m² are shown in Figure 6.9 and Figure 6.10. As it can be seen from the contours and the charts, increasing the mass flow rate leads to a higher flow velocity, which in turn causes a reduction in the volume fraction. As previously discussed, gas accumulation at the electrode should be minimized, as gas bubbles contribute to electrical resistance. Thus, higher mass flow rates may be preferable from this perspective.

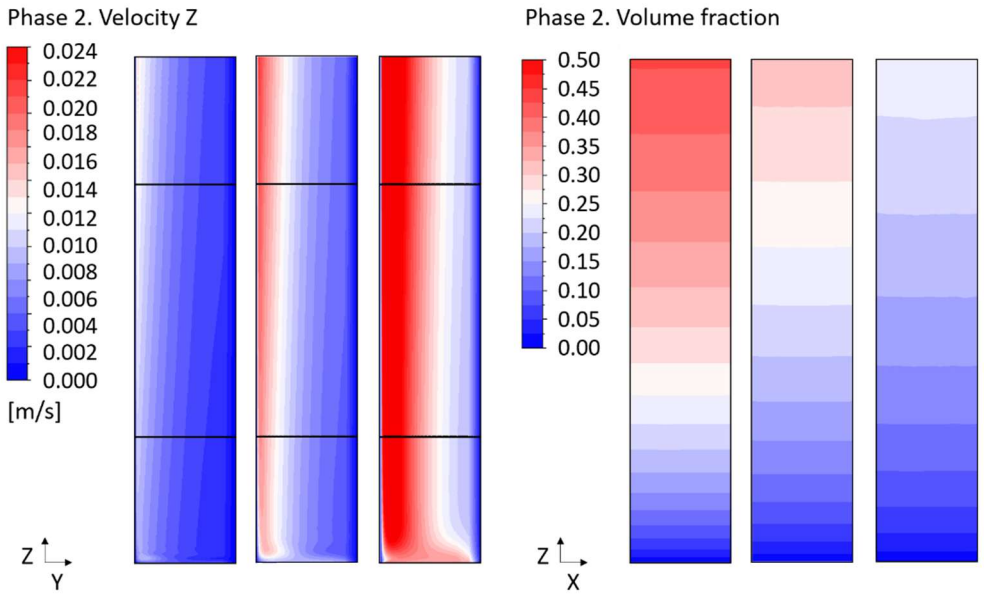

Figure 6.9: Gas vertical velocity close to the electrode for **(a)** half, **(b)** design and **(c)** double electrolyte mass flow rates and electrode gas *VF* for **(d)** half, **(e)** design and **(f)** double electrolyte mass flow rates, i_{ave}=5000 A/m².

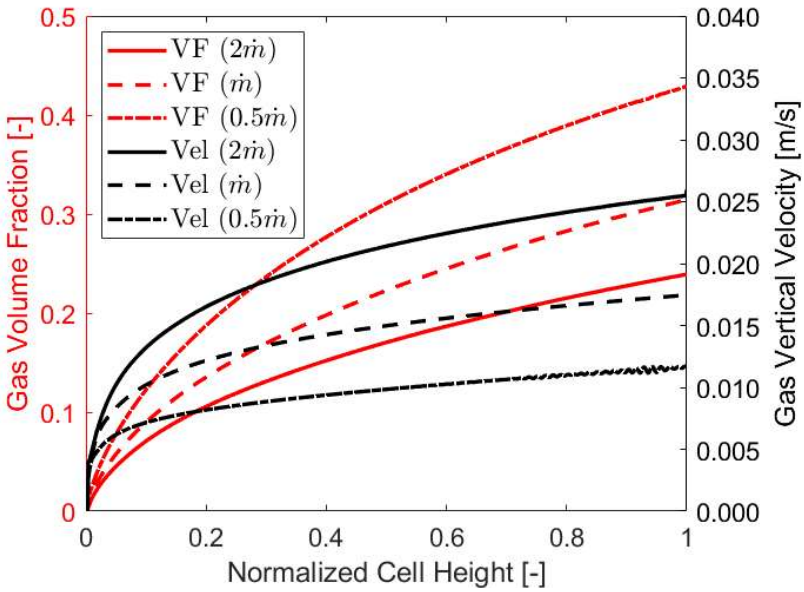

(a)

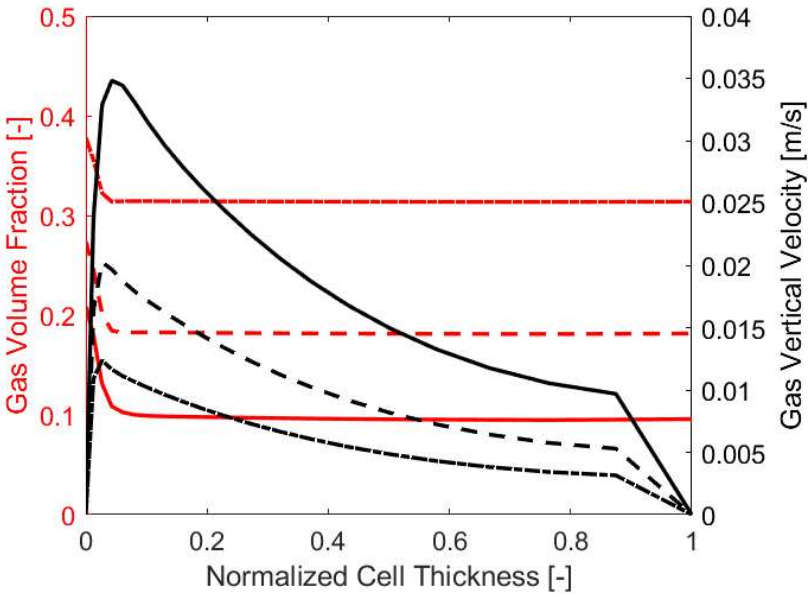

(b)

Figure 6.10: Gas vertical velocity and volume fraction along the cell **(a)** height and **(b)** thickness at three quarters of cell height for the three mass flow rates, i_{ave}=5000 A/m².

As additional analyses, the average gas VF at the outlet for different electrolyte flow rates and current densities is shown in Figure 6.11 (a). Furthermore, the ratio between the outlet and electrode average gas VF, as an indicator of gas accumulation inside the cell, is presented in Figure 6.11 (b).

The analysis reveals that when the mass flow rate is doubled, the average outlet gas volume fraction decreases by approximately 40%, while halving the mass flow rate increases it by 60%. This demonstrates that the mass flow rate significantly affects cell performance, even though overall hydrogen production remains constant for all i_{ave} values. Additionally, the ratio of VF_{ave}/VF_{out} grows with the mass flow rate, indicating more substantial gas accumulation at the electrode. As VF_{out} increases, the ratio tends to decrease, signifying that more hydrogen production encourages greater diffusion toward the center of the cell. Conversely, when hydrogen production is lower, gas tends to remain closer to the electrode without diffusing throughout the cell. Higher current densities allow for a greater potential for the gas to disperse within the cell, mixing with the electrolyte farther from the electrode.

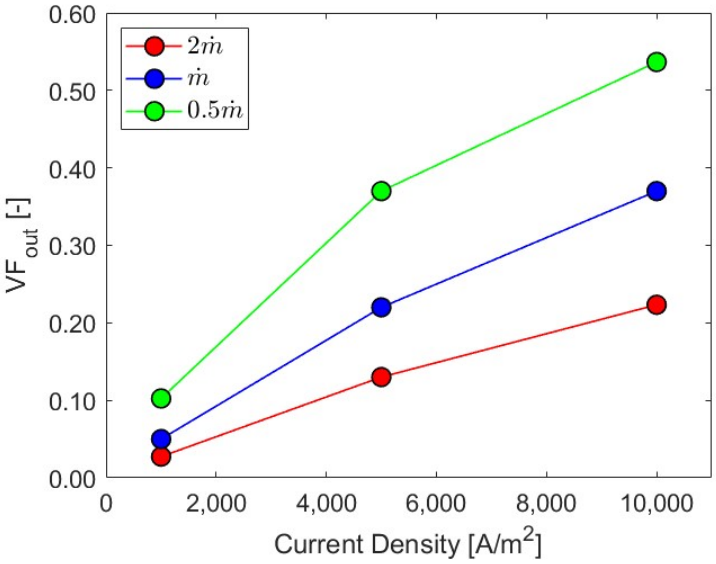

(a)

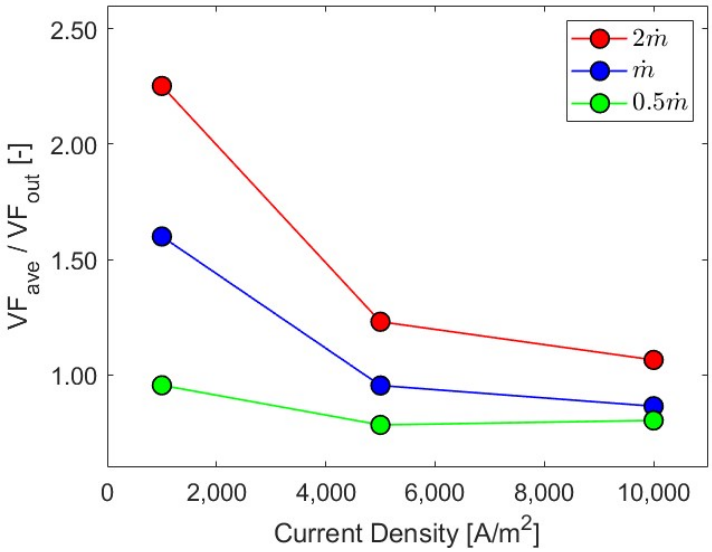

(b)

Figure 6.11: **(a)** Outlet average gas *VF* values and **(b)** ratio VF_{ave}/VF_{out} for the cases studied.

6.5 Discussion

The model application to the quasi-2D sector of the real-case cathodic cell revealed the impact of possible changes in operational parameters, such as the average current density and electrolyte mass flow. The ratio between electrode and outlet average gas volume fraction, VF_{ave}/VF_{out}, was employed as key performance indicator to account for gas accumulation. It could be observed that higher current densities mean a relative lower gas accumulation at the electrode surface, since the gas tends to spread towards the centre of the cell. Doubling or halving the electrolyte flow rate has a noticeable impact on the gas volume fraction. For instance, a sensitivity analysis showed that a double mass-flow rate at the inlet determines a reduction of about 40 % for the average outlet volume fraction, that is in turn raised by 60 % when the mass flow rate is halved. Conversely, when the mass flow rate is increased, a higher VF_{ave}/VF_{out} ratio can be detected, indicating a relatively more substantial accumulation of gas at the electrode. The main limit of the simulations described is represented by the lack of direct validation, due to both absence of data and confidentiality reasons. As already pointed out, the CFD modeling framework developed for the study comes, with the necessary modifications, from the validated test-case cell model of Chapter 5. However, this simplified application of the CFD model establishes a foundation for studying more advanced configurations and gives an idea of how fluid-dynamic and electrochemical variables interact.

7 COMPLETE 1-MW EZ CATHODIC CELL: SIMULATION AND PERFORMANCE ANALYSIS

The analysis presented in this chapter aims at providing the results obtained when applying the numerical model setup to the real-geometry cathodic cell of the 1-MW electrolyzer described in Section 4.2.

Six performance indicators, involving gas accumulation, bubble coverage, and flow uniformity, were defined and applied to the 3D CFD model, and possible optimizations of the cell geometry were evaluated. Filling the gaps in the literature, the definition of key metrics parameters can be of paramount importance for the fluid-dynamic assessment of the cell using CFD.

7.1 Geometry

The geometry of the electrolyzer cell was developed using Design Modeler software of ANSYS suite, focusing on the cathodic section of the alkaline cell, specifically the region between the cathode and the bipolar plate. The numerical domain is highlighted in Figure 7.1.

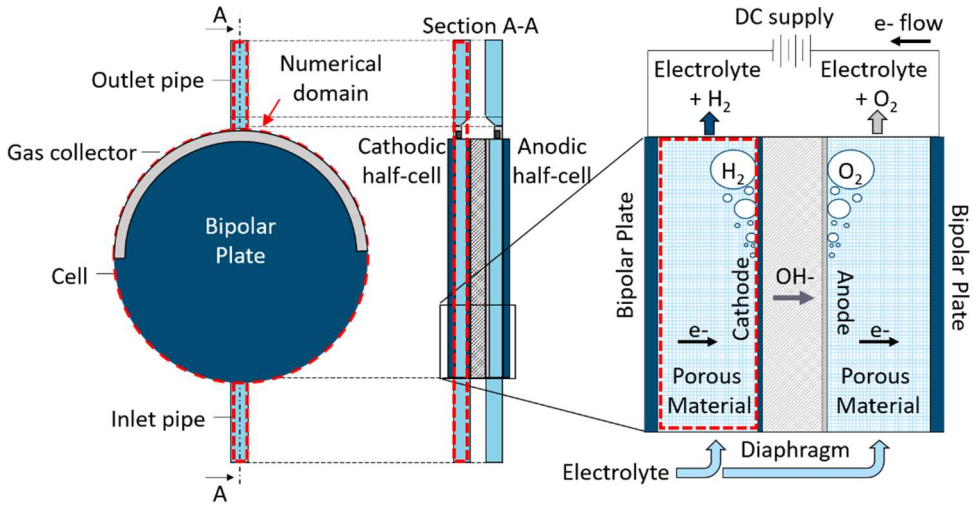

Figure 7.1: 1-MW EZ cell scheme and numerical domain

Starting with the original configuration, designated as “Case 1,” alternative designs were explored to address potential inefficiencies in gas flow management. The primary focus was on the gas collector located at the top of the cell.

In the standard configuration, the gas collector includes orifices that accelerate the flow toward the outlet. However, the solid structures between these orifices were hypothesized to obstruct gas movement. To test this, the first modification involved removing these obstructions, resulting in “Case 2.” Next, to further enhance flow dynamics, a sloped design for the gas collector was introduced, referred to as “Case 2-slope.” Finally, a scenario without any gas collector was considered. This approach was prompted by observations during CFD simulations that the gas collector’s geometry hindered the upward movement of gas toward the outlet pipe, particularly due to the electrode’s placement within the cell.

Figure 7.2 provides insights into gas behavior in the collector area, with contours of gas volume fraction displayed on a vertical section. The electrode, positioned on the right, shows a notably higher gas volume fraction. The narrowed section leading to the gas collector in the upper part of the cell was found to impede gas ascent, causing unwanted gas accumulation.

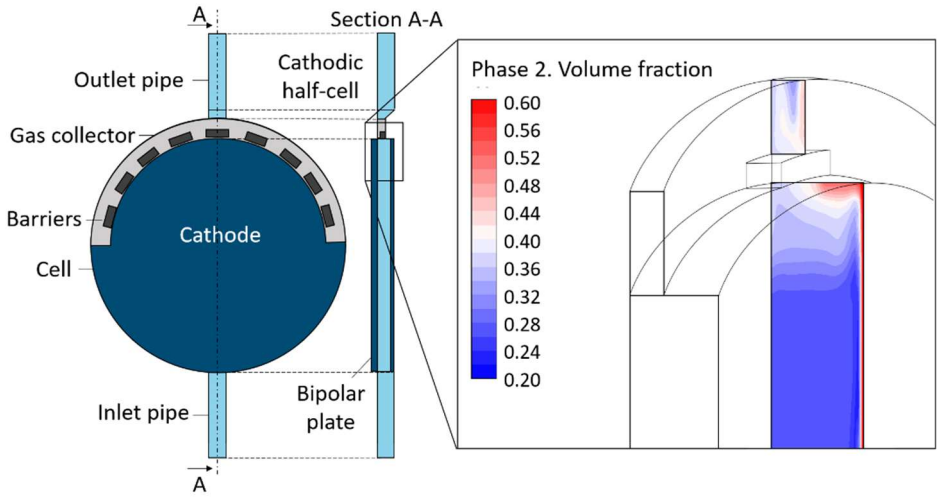

Figure 7.2: Gas volume fraction contour in the upper part of the cathodic half-cell.

The removal of the gas collector led to the development of three case studies. “Case 3” retained the original electrode surface, while “Case 4” and “Case 5” expanded the electrode area to include the region previously occupied by the gas collector. In “Case 4,” the current density remained unchanged, resulting in higher hydrogen production. Conversely, in “Case 5,” the current density was reduced to maintain the same hydrogen production as the original design.

Although specific cell details remain proprietary information of the company, Figure 7.3 illustrates the general layout of the original and modified geometries. The gas collector is shown in grey, while the electrode area is represented in dark blue. All cases, except “Case 5,” were designed with the same average current density as the original geometry. In “Case 5,” the current density was reduced by 7%, corresponding to the proportion of the collector area relative to the electrode surface. This adjustment ensured the total current was consistent with the original design. Table 7.1 provides an overview of the main operating parameters, with “Design” indicating the nominal one.

Table 7.1: Operating parameters for the six cases.

Operating parameters	Case 1	Case 2	Case 2-slope	Case 3	Case 4	Case 5
Electrode area		Design			+7%	+7%
Current density		Design			Design	−7%
Total current		Design			+7%	Design
Hydrogen production		Design			+7%	Design

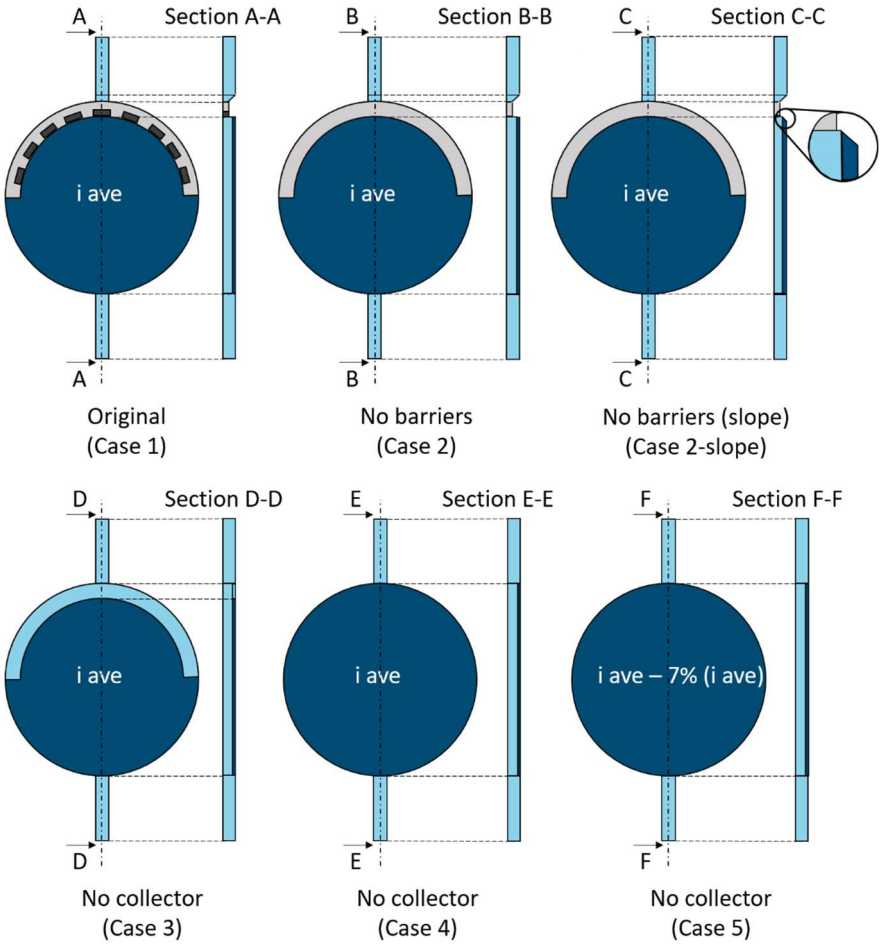

Figure 7.3: Original (Case 1) and modified geometries (Case 2-Case 5), with respective sections.

7.2 Mesh

A hexahedral mesh was created using the ANSYS meshing environment, followed by a grid independence test to ensure accurate modeling. As discussed in Section 5.1, simulations involving two-phase flows require a careful balance between the gas bubble size and the thickness of the gas production layer. This balance is essential for achieving a minimum grid thickness, L_{min}, at the electrode, ensuring the simulations remain stable and physically meaningful. For this study, the minimum required layer size at the electrode was calculated to be 110 µm, based on a chosen bubble diameter of 10 µm, as further explained in Section 7.3.

To meet these criteria, a minimum cell size of 150 µm was selected. Starting from this baseline, four different mesh configurations were tested, two with a minimum cell thickness of 150 µm at the electrode and two with a minimum size of 225 µm. The primary distinction among these configurations lay in the cell size perpendicular to the electrode, as this direction represents the largest variable gradient. The number of elements varied significantly, with “Mesh 1” and “Mesh 2” containing approximately 8 million and 4 million elements, respectively, while “Mesh 3” and “Mesh 4” had 2 million and 1 million elements, as detailed in Table 7.2, which summarizes the layer thickness and total number of cells for each refinement scenario.

Table 7.2: Features of the selected mesh sensitivity cases.

Mesh features	Mesh 1	Mesh 2	Mesh 3	Mesh 4
Layer size [µm]	150	150	225	225
Number of cells [-]	8E6	4E6	2E6	1E6

The results of these configurations, shown in Figure 7.4 compare gas volume fraction (VF) and vertical velocity across the four cases. The analysis revealed that the finest mesh, “Mesh 1,” produced results very similar to those of “Mesh 2.” Similarly, the coarser meshes, “Mesh 3” and “Mesh 4,” yielded comparable outcomes between each other but differed significantly from the finer meshes. Based on these findings, “Mesh 2” was selected as the optimal choice, balancing precision with computational efficiency. In Figure 7.5 some mesh details are displayed.

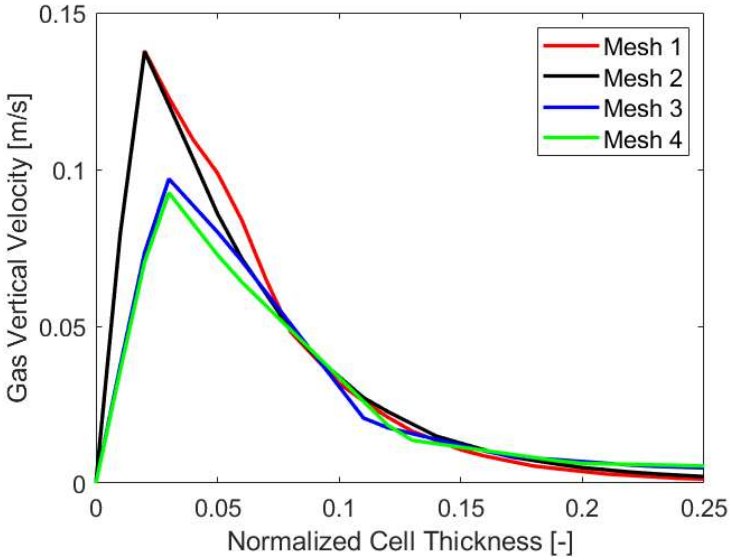

(a)

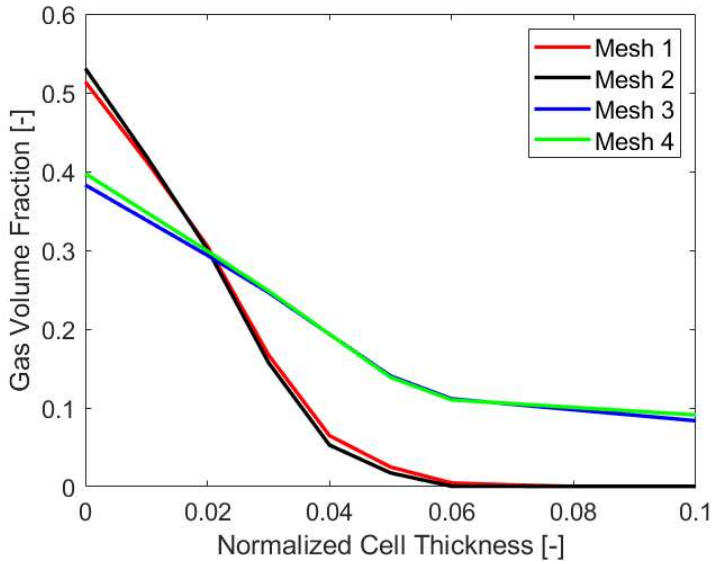

(b)

Figure 7.4: Mesh sensitivity analysis: **(a)** gas vertical velocity and **(b)** *VF* along the cell thickness.

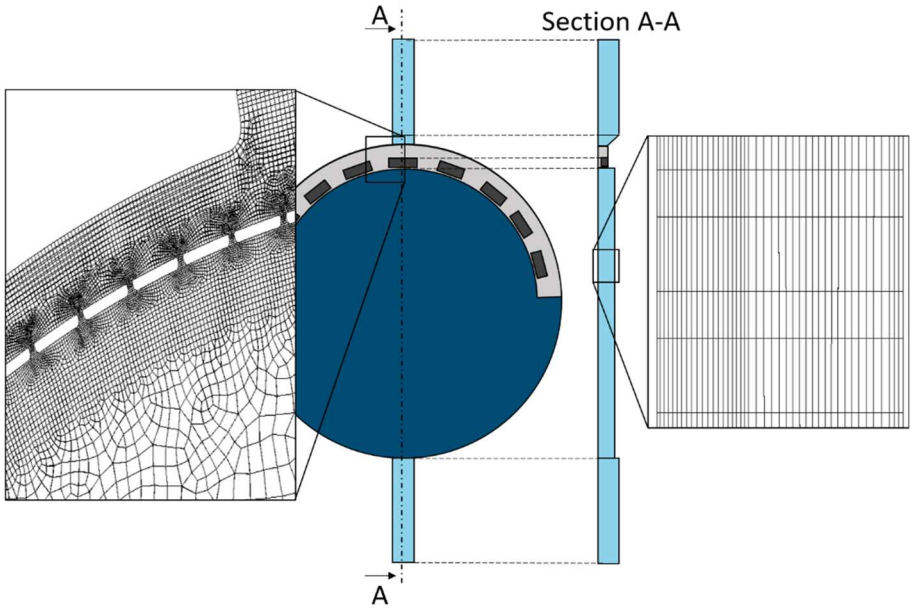

Figure 7.5: 1-MW EZ cathodic half-cell mesh details.

7.3 Modeling hypotheses

The Eulerian two-phase model described in Chapters 2 and 3 was employed with the following assumptions:

- The inlet temperature and operating pressure were set to 60 °C and 30 bar, respectively, reflecting real application conditions.
- The primary phase was modeled as a 28 wt% solution of KOH in water, while hydrogen was considered as the secondary phase.
- A turbulent flow regime was assumed, employing the $k-\omega$ SST model with low Reynolds correction. As part of the model setup, $y+$ values were maintained below 1 within the boundary layer.
- The hydrogen gas bubbles were assumed to have a constant diameter of 10 µm. This value was determined based on the empirical findings presented in [83], which characterized the mean bubble diameter as a function of working pressures ranging from 1 to 200 bar using the empirical Eq. 3.4 and 3.5.
- Bubble coalescence and breakage were neglected due to the high current densities.
- The cell is porous with viscous and inertial resistance coefficients of Eq. 3.7, obtained through calibration of Davies correlation (Eq. 3.8).

- The same forces described in Section 5.2.1 were employed for the model.
- Surface tension was taken as 60 mN/m, corresponding to water's surface tension at the specified pressure and temperature.
- Turbulent dispersion force was not considered for the reasons explained in 6.3.

The electrochemical model was integrated in the setup through hydrogen evolution reaction (Eq. 1.1) and variable current density at the cathode, by means of Eq. 3.10.

As for the boundary conditions, a specified pressure gauge value was set at the outlet and a mass flow rate was imposed at the inlet. No-slip conditions were applied at the cathode and bipolar plate walls for both the liquid and gas phases.

7.4 Key performance indicators

The authors employed six key performance indicators (KPIs) to evaluate the cell's fluid dynamics performance:

- Gas volume inside the cell (V_{gas}): this metric measures the volume of gas present in the region of the cell adjacent to the electrode. A smaller gas volume is preferred as dispersed gas increases electrolyte resistivity, thereby raising the overall cell potential. To facilitate comparison, the values for "Case 4" and "Case 5" were normalized by multiplying them by the ratio of the original to the extended active cell volume.
- Average gas volume fraction at the electrode (VF_{ave}): reflecting the concept of bubble coverage, this KPI is critical as it directly influences electrode functionality.
- Maximum gas volume fraction at the electrode (VF_{max}): this parameter helps identify potential hot spots that may lead to material degradation. High local gas concentrations can impact the temperature distribution on the electrode, particularly on the anode, where oxygen's specific heat is generally lower than that of the electrolyte under typical operating conditions.
- Ratio of gas volume fraction at the electrode to gas volume fraction at the outlet (VF_{ratio}): this ratio indicates the extent of gas accumulation at the electrode compared to the gas exiting the cell. It corresponds to the VF_{ave}/VF_{out} ratio, already employed for the results of Chapter 6. It is particularly useful for comparing various current density cases within the same geometry.

- Velocity uniformity (Γ): as defined in Eq. 7.1 [48], this metric evaluates the uniformity of the flow field.

$$\Gamma = 1 - \frac{1}{2n}\sum_{i=1}^{n}\frac{|u_i - \bar{u}|}{\bar{u}}, \qquad 7.1$$

The velocity uniformity indicator, Γ, is determined using an arbitrary number of n points in a specified section for analysis. $\bar{u}$ represents the average fluid velocity across the selected points, and u_i is the velocity at a specific point. This parameter provides insight into how uniform the flow velocity is compared to the average velocity within a given section. Γ ranges between 0 and 1, where $\Gamma = 1$ signifies completely uniform velocity. However, in this study, uniform velocity across the section is unlikely due to higher flow velocities near the cathode.

- Liquid recirculation $\bar{V}_{rec}$: this metric is the ratio of the maximum downward to upward liquid velocities measured at the midsection of the cell. Downward velocities are caused by recirculation effects, while upward velocities result from electrolyte flow and gas buoyancy. While reduced recirculation generally improves efficiency, literature lacks extensive studies on this phenomenon. Some local turbulence might benefit gas removal, as highlighted by Zarghami *et al.* [37].

For the current analysis, the horizontal midsection of the cell, perpendicular to the flow streamlines, was identified as the most suitable location for calculating Γ and $\bar{V}_{rec}$. Specifically, 500 points were selected along five lines within this section, as illustrated in Figure 7.6.

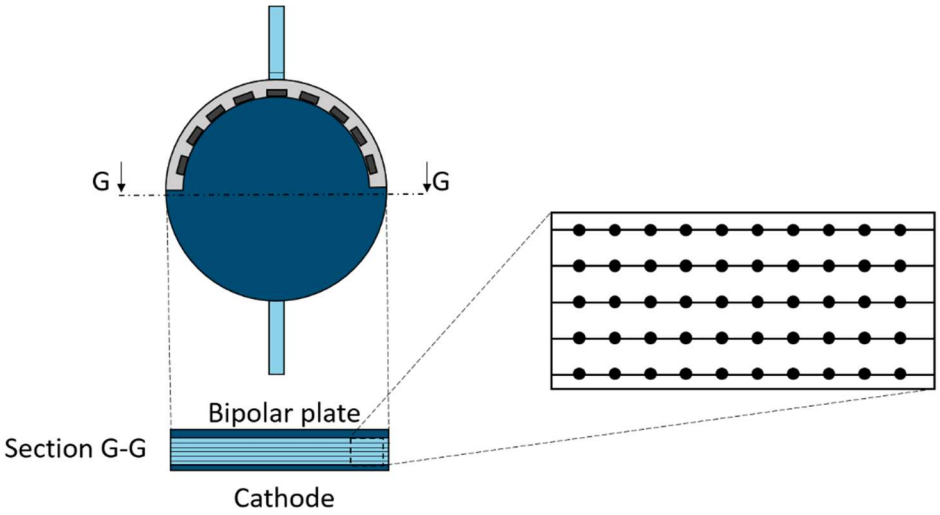

Figure 7.6: Mid-section detail with the point distribution for Γ calculation.

7.5 Results: geometry optimization analysis

The application of the multi-physics model to the cathodic half-cell first aimed at optimizing the cell design, through the use of the parameters described in Section 7.4 for the different cases outlined in Section 7.1. As further analyses, the gas vertical velocities and volume fraction are reported case by case.

7.5.1 Cell optimization through KPIs

The six parameters outlined in Section 7.4 were utilized in the converged CFD simulations of the alkaline cathodic half-cell. Table 7.3 summarizes the simulation results for each scenario, ranking performance from worst to best. The color gradient transitions from red (indicating the poorest performance) to green (representing the highest performance) according to the chosen parameters.

Table 7.3: Performance parameters for the six cases.

Parameters	Case 1	Case 2	Case 2-slope	Case 3	Case 4	Case 5
V_{gas} [m³]	2.11 × 10⁻4	1.75 × 10⁻4	1.37 × 10⁻4	2.04 × 10⁻4	2.58 × 10⁻4	2.27 × 10⁻4
VF_{ave} [-]	0.47	0.44	0.51	0.47	0.47	0.46
VF_{max} [-]	0.65	0.65	0.69	0.63	0.64	0.63
VF_{ratio} [-]	1.34	1.33	1.53	1.49	1.42	1.47
Γ [-]	0.129	0.120	0.123	0.124	0.135	0.113
$\bar{V}_{rec}$ [-]	5.32%	3.34%	4.11%	5.12%	5.37%	4.85%

Regarding the gas volume within the cell, eliminating gas obstacles, as seen in "Case 2," or introducing a slope on the gas collector proves advantageous. Notably, "Case 2-slope" demonstrates the lowest gas volume inside the cell. The reduced gas accumulation observed in "Case 5," compared to "Case 4," can be attributed to a broader surface area for hydrogen production and a lower current density. In contrast, the gas volume in "Case 3" is lower than in other configurations lacking a collector, as gas predominantly accumulates at the top, where the electrode is absent in this geometry.

For VF_{ave}, the various geometries show similar performance, except for "Case 2," which produces a lower output. Interestingly, "Case 2-slope" yields a higher VF_{ave} value, contradicting the trend observed for gas volume. Simulations indicate undesired gas accumulation beneath the slope, contributing to the elevated VF_{ave} value at the electrode. Consequently, "Case 2-slope" also exhibits the highest maximum gas VF at the electrode, whereas other cases are more comparable.

"Case 1" and "Case 2" report the lowest ratios between gas VF at the electrode and at the outlet. Further analysis suggests that the gas collector increases flow velocity in the cell's upper region, locally reducing gas VF. However, the outlet gas volume fraction remains consistent across geometries. Cases lacking a collector perform worse in this aspect, with lower values under higher current density conditions, as seen in "Case 4." This may be linked to higher velocities resulting from increased hydrogen production. Conversely, "Case 2-slope" is affected by higher average gas VF at the electrode, as previously discussed.

The parameter Γ shows minimal variation between geometries. However, "Case 5" exhibits reduced flow uniformity due to diminished gas buoyancy associated with lower current density. This reduction in vertical velocity creates localized vortices that impact Γ. In contrast, "Case 4," with its higher hydrogen production and vertical velocities, achieves the highest velocity uniformity. Notably, Γ is sensitive to the selected locations for velocity calculations.

The final parameter, liquid recirculation ($\bar{V}_{rec}$), shows lower values when the collector is present but obstacles are absent, likely due to increased velocities in the cell's upper region, which reduce recirculation. "Case 4," however, exhibits enhanced recirculation, driven by higher velocities within the cell. A comparison with Γ reveals no strict correlation between these two parameters.

Gas accumulation parameters can also be evaluated by analyzing the gas volume fraction contours in a vertical section of the cell's upper region, as shown in Figure 7.7.

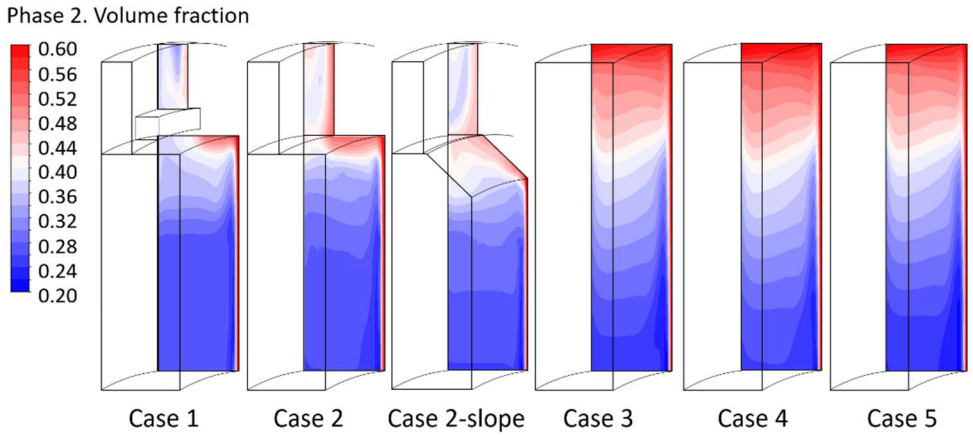

Figure 7.7: Gas volume fraction contour in a vertical section in the upper part of the cell, case by case.

The analysis shows that gas faces greater challenges in escaping the cell in scenarios without the collector. This adversely affects the gas accumulation indicator, particularly in “Case 4” and “Case 5,” where the electrode extends to the top of the cell, as previously discussed. Furthermore, a detailed examination of the volume fraction contours on the electrode offers valuable insights into bubble coverage parameters, as depicted in Figure 7.8.

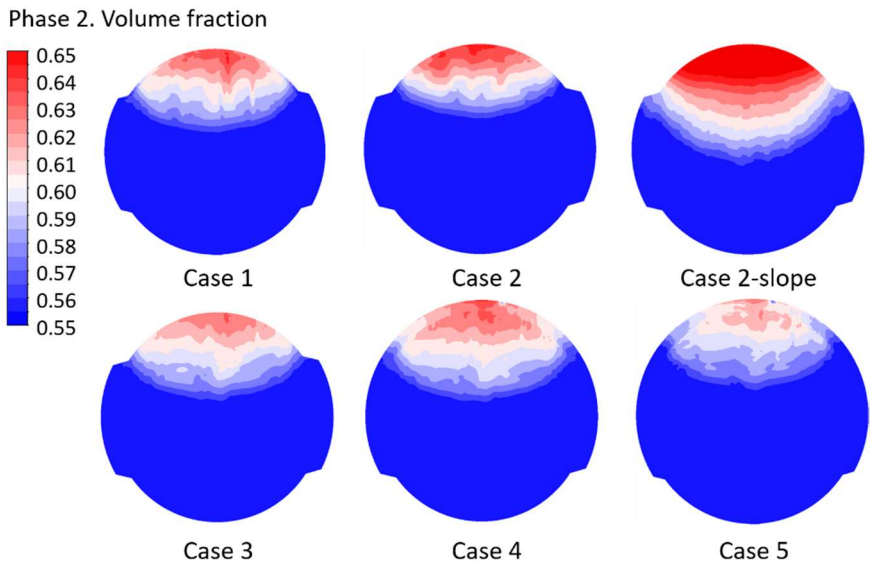

Figure 7.8: Gas volume fraction contour at the electrode, case by case.

The average and maximum gas VF values for "Case 2-slope" can be directly interpreted from the contours, confirming that this geometry is ineffective at removing gas. In contrast, lower maximum gas volume fraction values are observed in Cases 3 to 5, particularly for Case 5, which is associated with lower current density.

The flow uniformity parameter (Γ) was also evaluated at various sections of the cell: at one-quarter height, three-quarters height, and at the outlet pipe section, to provide a more comprehensive analysis. The case-by-case results are presented in the chart of Figure 7.9.

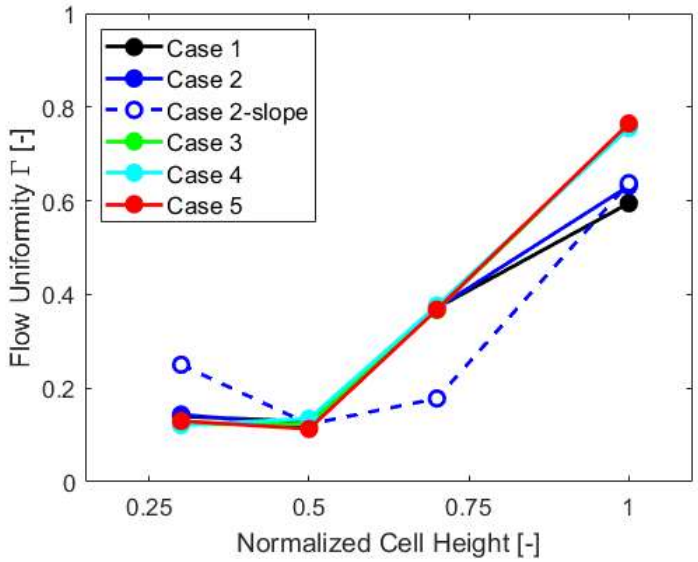

Figure 7.9: Flow uniformity at different sections of the cell, case by case.

The flow uniformity analysis reveals that "Case 2-slope" differs significantly from the other cases. It exhibits greater non-uniformity in the upper part of the cell and improved uniformity in the lower part. This behavior is primarily influenced by the VF distribution, with higher values observed near the top of the cell (as shown in Figure 7.8), which affects the velocity field. The Γ values in the lower part of the cell are influenced by the inlet components, which remain consistent across all geometries, displaying similar behavior up to three-quarters of the cell height. However, the outlet Γ values are affected by the presence of the gas collector, resulting in higher flow uniformity in cases where this component is absent.

7.5.2 Gas vertical velocity and volume fraction

To expand the analysis further, Figure 7.10 presents gas VF and velocity trends along the cell thickness at the mid-section, while Figure 7.11 displays these trends along the electrode for each case analyzed.

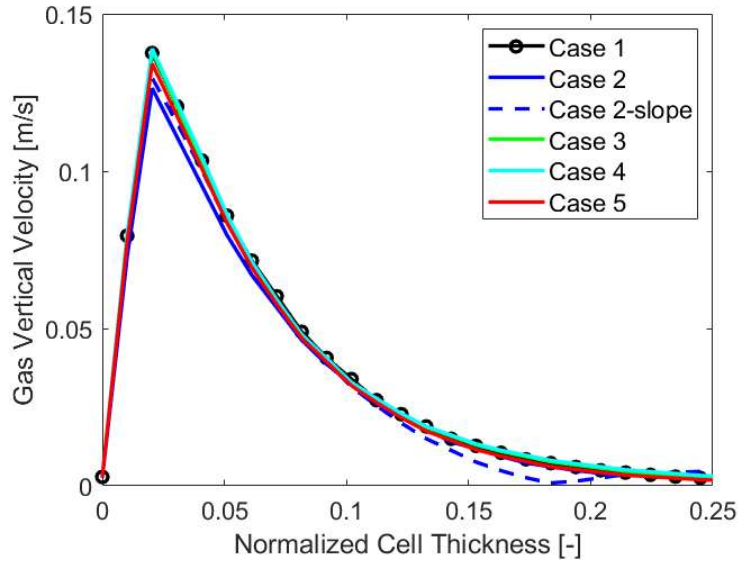

(a)

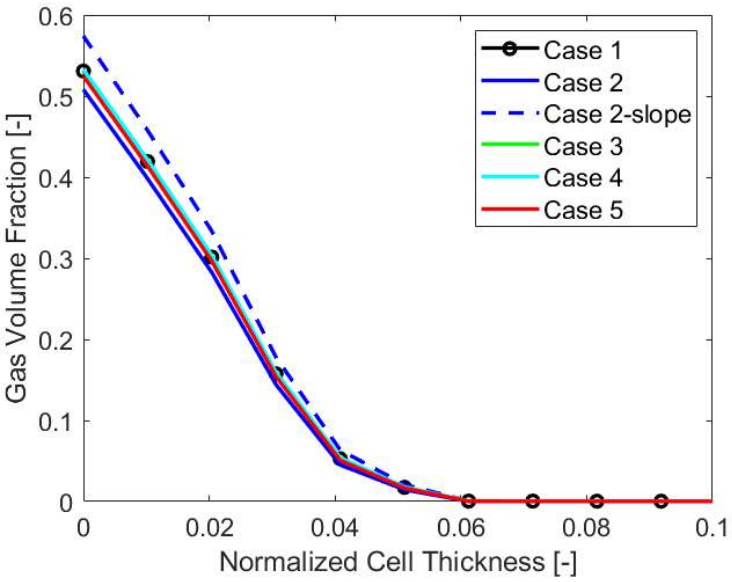

(b)

Figure 7.10: (a) Gas vertical velocity and **(b)** gas volume fraction along the cell thickness, case by case.

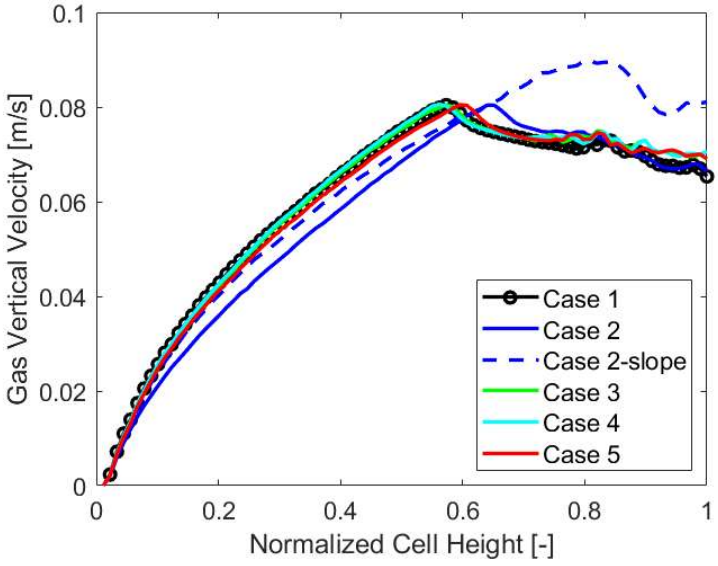

(a)

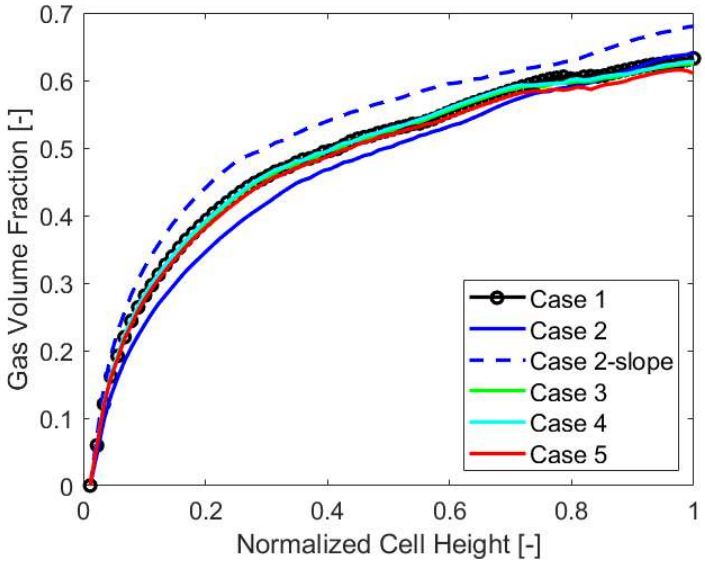

(b)

Figure 7.11: (a) Gas vertical velocity and **(b)** gas volume fraction along the electrode, case by case.

The key observation from these charts is the generally lower gas vertical velocity and volume fraction in "Case 2," which demonstrates better performance when assessed using the selected parameters. Conversely, "Case

2-slope" shows a higher gas volume fraction both along the cell thickness and the electrode, resulting in distinctive velocity behavior along the electrode, as corroborated by the Γ parameter analysis. The other cases exhibit comparable trends for gas VF and velocity.

7.6 Results: original-cell sensitivity analysis

After assessing the performance of various optimized geometries under design conditions, sensitivity analysis of the original geometry ("Case 1") to changes in electrolyte mass flow rate and current density was analyzed. Three inlet mass flow rates were tested, i.e. half, design and double mass flow rates of the electrolyte. Additionally, five average current densities (1000, 2500, 5000, 7500, and 10,000 A/m²) were considered, covering the typical operating range, including part-load conditions, of commercial electrolyzers as determined through market analysis.

Figure 7.12, Figure 7.13 and Figure 7.14 illustrate the variations of the six performance indicators with respect to current density and inlet mass flow rate.

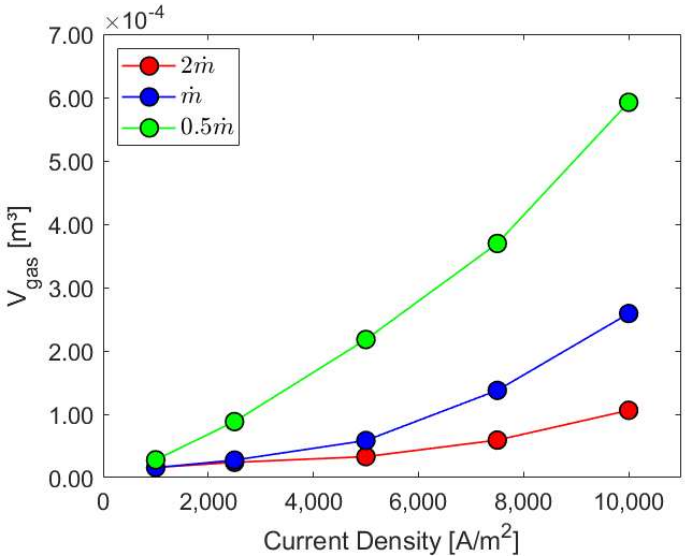

(a)

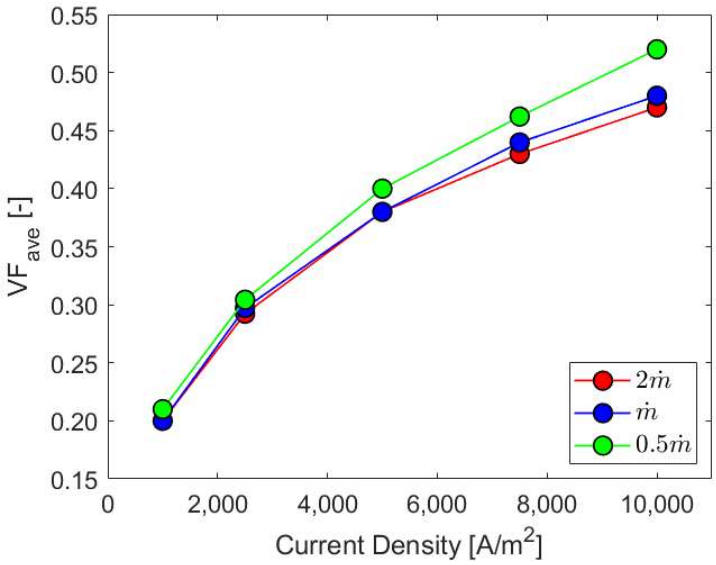

(b)

Figure 7.12: Sensitivity analysis: **(a)** gas volume inside the cell and **(b)** average gas *VF* at the electrode.

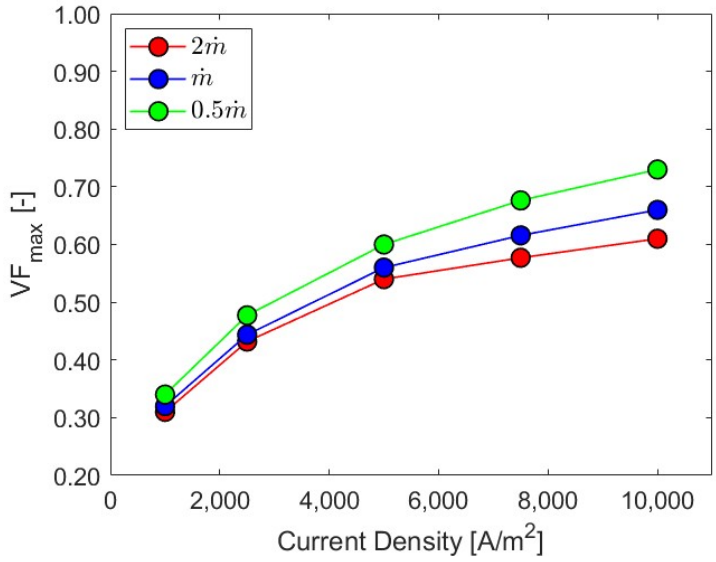

(a)

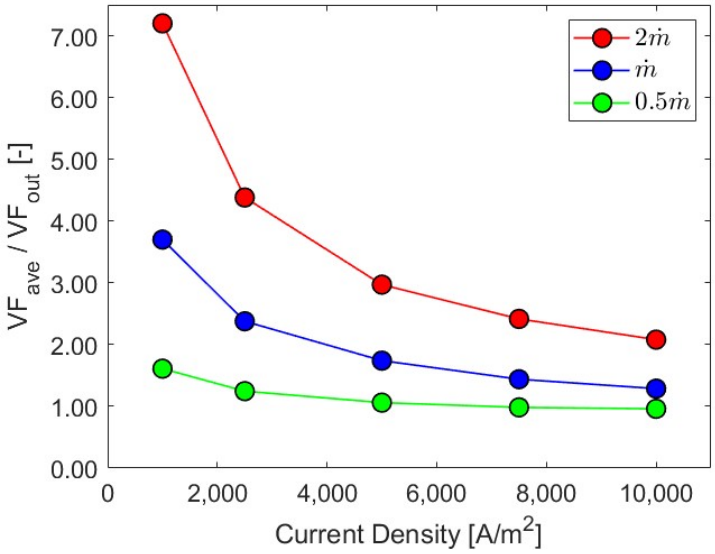

(b)

Figure 7.13: Sensitivity analysis: **(a)** maximum gas *VF* at the electrode and **(b)** ratio VF_{ave}/VF_{out}.

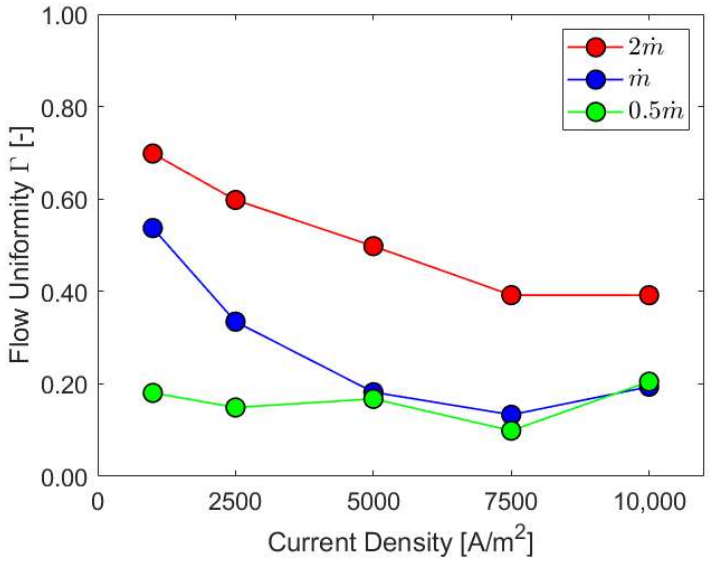

(a)

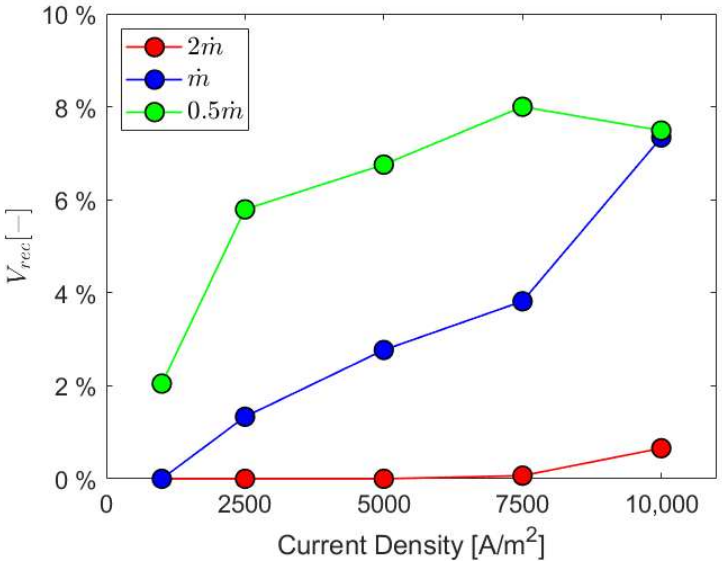

(b)

Figure 7.14: Sensitivity analysis: **(a)** flow uniformity (*Γ*) and **(b)** liquid recirculation ($\bar{V}_{rec}$).

Higher inlet mass flow rates enhance cell performance for the first three parameters, especially at higher current densities. As expected, gas volume and electrode gas presence increase with current density, which correlates with hydrogen production. Conversely, the VF_{ave}/VF_{out} ratio decreases with lower mass flows and increases at higher current densities due to their impact on outlet gas VF. The Γ parameter at the mid-section improves with higher inlet mass flow rates but slightly decreases with increasing current density. Higher flow rates, however, hinder electrolyte recirculation within the cell, as shown in Figure 7.14 (b). Elevated current densities contribute to increased turbulence, promoting vortices and recirculation within the cell.

The Γ parameter was also evaluated for different sections of the cell under two conditions: constant current density of 5000 A/m² and the design inlet mass flow rate. The results are shown in Figure 7.15.

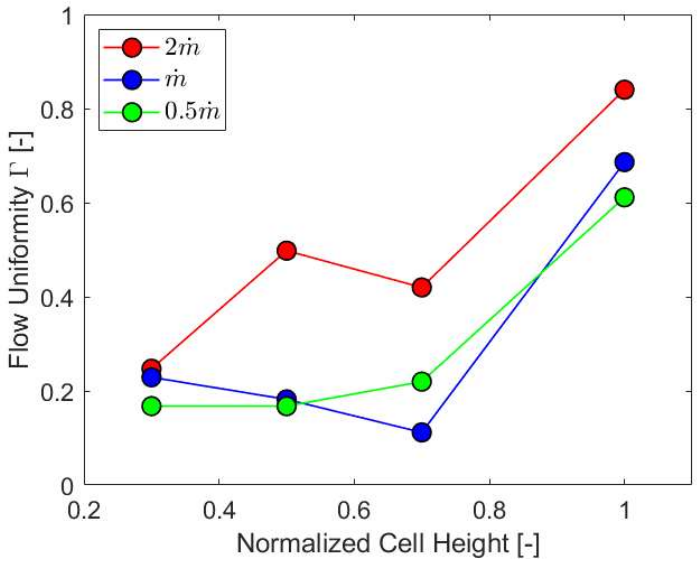

(a)

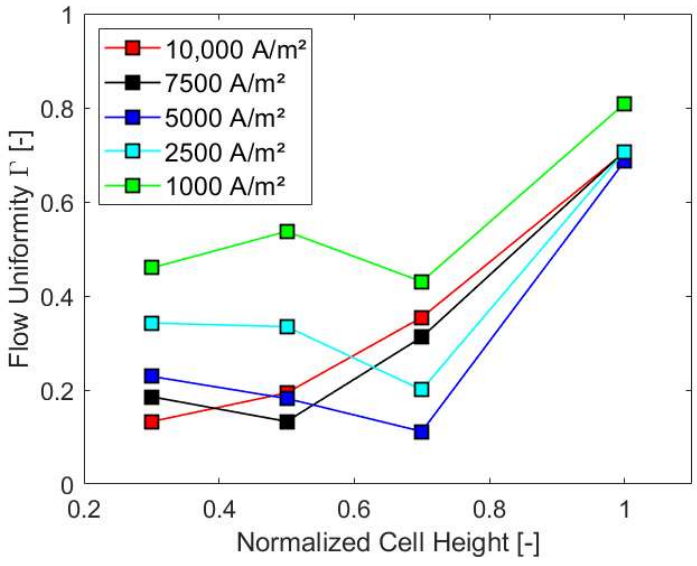

(b)

Figure 7.15: *Γ* in different sections for **(a)** *i*= 5000 A/m² and **(b)** design inlet mass flow rate.

As expected, higher inlet mass flow rates and lower current densities result in greater flow uniformity throughout the cell. The downward Γ trend between half and three-quarters of the cell height for higher mass flows (Figure 7.15 (a)) is due to vortices caused by the section reduction at the top and the presence of

the gas collector, which more significantly impacts these cases. This trend is more pronounced at lower current densities (Figure 7.15(b)), where reduced gas production leads to lower velocities along the electrode. Across all cases, Γ increases between three-quarters and the top of the cell, where the flow becomes more uniform as it accelerates toward the outlet pipe.

7.7 Discussion

The results of the 3D CFD model for the cathodic cell provided valuable insights into its fluid dynamics, particularly regarding gas accumulation and overall efficiency. Six key performance indicators were analyzed, with an emphasis on parameters directly influencing overpotentials, such as gas volume fraction and flow characteristics.

The most critical factors for efficiency in zero-gap cells, where gas directly affects ohmic resistance, are the average gas volume fraction at the electrode (VF_{ave}) and the VF_{ratio} parameter (the ratio of the average gas volume fraction at the electrode to that at the outlet). In contrast, the total gas volume inside the cell (V_{gas}) is more impactful in traditional cells with greater electrode spacing. Although less critical for efficiency, VF_{max} remains significant for identifying hot spots, making it secondary but still essential for understanding cell behavior.

Flow uniformity (Γ) and recirculation require a different evaluation approach. While linked to cell efficiency, since stagnation and uneven reactant distribution reduce reaction rates and increase overpotentials, as noted in [48], the regular geometry of the studied cell reduces their importance. In the mid-section, velocity gradients primarily occur along the cell thickness, with higher velocities near the electrode and negligible lateral variations. As a result, flow uniformity is less critical for this specific geometry.

For velocity recirculation, although it was not positively evaluated in this study, it could potentially enhance performance by promoting turbulence, which may improve reaction rates and bubble removal. This warrants further investigation in future studies.

Optimizing the cell geometry revealed important links between design characteristics and performance parameters. The gas collector component does not appear to negatively affect gas accumulation or bubble coverage on the electrode, likely due to the higher velocities caused by the section reduction. “Case 2,” without flow obstacles, performed better than the other designs, particularly when prioritizing the key indicators. Both gas volume fraction and velocity contours, as well as their trends, confirm the underperformance of

"Case 2-slope," which experiences higher gas accumulation under the gas collector.

The sensitivity analysis yielded the following conclusions: higher VF_{ave} values are associated with higher current densities, as expected from Faraday's law, but are less influenced by the electrolyte mass flow rate. VF_{ratio} is a more suitable efficiency indicator at lower current densities, where lower mass flow rates are preferable. At higher current densities, increased mass flow rates benefit gas volume inside the cell, as gas accumulation grows with current density. To prevent hot spots associated with VF_{max} , higher mass flow rates are recommended. Flow uniformity (Γ) improves with increased mass flow rates and decreases with higher current densities. Flow recirculation is more pronounced at lower mass flow rates and higher current densities.

These findings align with the observations of Mat *et al.* [46], who noted that higher electrolyte flow velocities increase the gas release rate due to reduced bubble residence time.

The primary limitation of the simulations presented is the lack of direct validation, due to both the absence of data and confidentiality concerns. As already pointed out, the CFD modeling framework developed for the study comes, with the necessary modifications, from the validated test-case cell model of Chapter 5. Nevertheless, this first application of the 3D CFD model to a cathodic cell can be considered as highly valuable for the scientific literature on the topic.

8 COMPLETE 50-kW EZ CELL AND STACK: MULTI-PHYSICS MODEL APPLICATION

The last research step presents the application of the full multi-physics 3D model to a complete alkaline electrolyzer cell, anode-to-cathode. In particular, for this last analysis, PIEL H15 electrolyzer, outlined in Section 4.3, was considered.

The model is capable of simulating any cell within the stack through tailored boundary conditions. Advancing beyond the current state-of-the-art, the model integrates all relevant physical processes involved in electrolysis, including two-phase flow, electrochemistry, and thermal dynamics. To account for the effects of hydrogen and oxygen bubble coverage, the model incorporates the variable current density definition described in Section 3.3, based on gas presence at the electrodes.

Heat generation within the cell, arising from electrical resistances and electrochemical reactions, is modeled using the three distinct source terms, Faraday, chemical reactions and Joule heating as discussed in Section 3.4. The semi-permeable, porous diaphragm is designed to allow only electrolyte flow while blocking generated gases, while also facilitating thermal communication between the two half-cells.

The model realistically accounts for pressure drops and mass flow conditions experienced by individual cells, from the first to the last in the stack, compared to theoretical scenarios.

8.1 Geometry

The geometry of the electrolyzer cell described in Section 4.3 was developed using the Design Modeler software from the ANSYS suite. The numerical domain represents the section of the alkaline electrolyzer cell spanning from the cathode to the anode, as shown in Figure 8.1. The area of the electrode enclosed between a quarter and three-quarters of the cell height was selected to be shown in the results section, reported in green in Figure 8.1. In fact, for confidentiality regarding the exact cell geometry, no full pictures can be provided. This geometry includes the entire cell, a feature rarely seen in state-of-the-art CFD models for electrolysis, comprising both half-cells and the diaphragm that separates them, with a porosity of 0.6. The full-cell configuration was designed to simulate any of the 115 cells in the stack by applying specific boundary conditions, as outlined in Section 8.3.1.

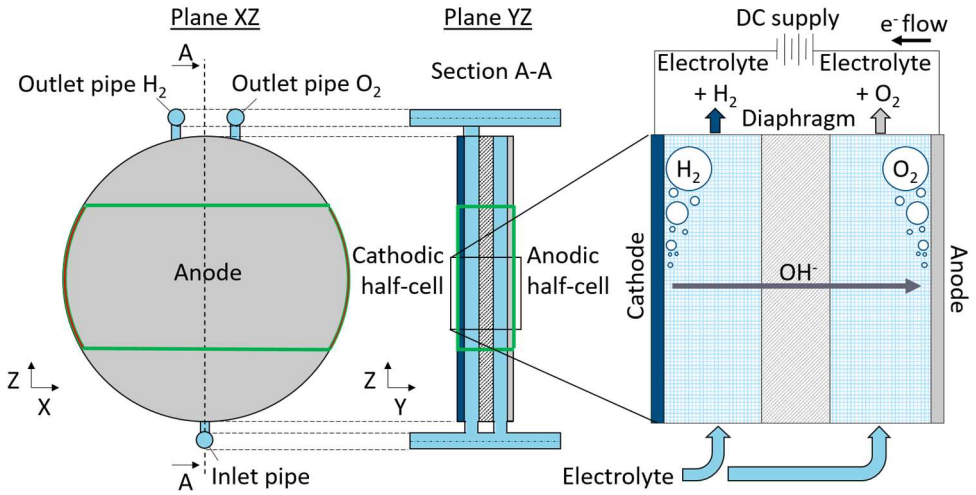

Figure 8.1: 50-kW EZ cell numerical domain and results area.

To evaluate the diaphragm's influence, a case excluding this component was also analyzed. Its high porosity results in minimal liquid velocity within the diaphragm region, suggesting that it could be omitted for analyses focused solely on fluid dynamics. However, the diaphragm proved essential for accurately modeling thermal distribution within the cell.

Two full-cell geometries were created to represent individual cells within the stack, with simulations performed for first, central (58^{th}) and the last cell (115^{th}). One geometry was tailored to the 115^{th} cell, featuring a single inlet at the bottom and two outlets at the top. The second geometry represents the remaining

114 cells, having one inlet and one outlet at both the bottom and top channels, as schematically illustrated in Figure 8.2.

Additional cells were not simulated as their inclusion was unlikely to yield significant new insights. Furthermore, the computational expense of simulating individual cells and the need for precise boundary condition adjustments justified limiting the analysis to these representative cases.

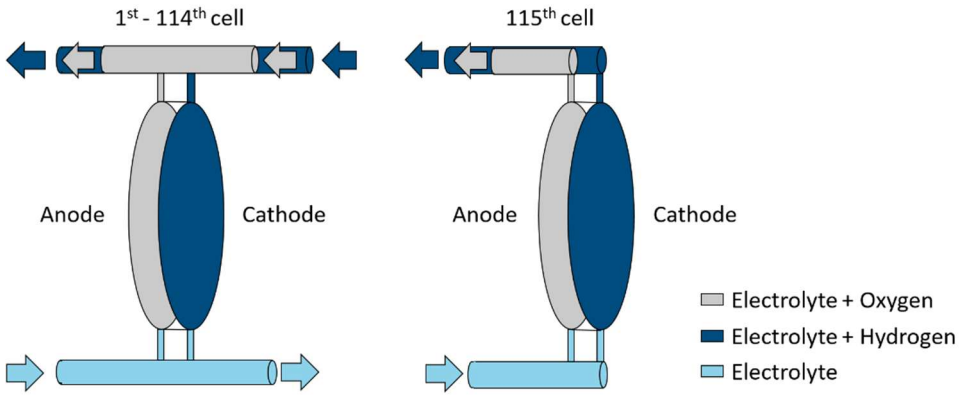

Figure 8.2: Scheme of the two different geometries for the stack modeling.

8.2 Mesh

A hexahedral mesh was generated using the ANSYS Meshing environment, followed by a grid independence test to ensure accurate modeling. As highlighted in Section 5.1, modeling two-phase flows requires a careful balance between the gas bubble size and the gas production layer thickness to determine the minimum grid thickness. For the case-study cell, the calculated minimum layer thickness at the electrode was 60 µm, based on a chosen bubble diameter of 20 µm.

In Eulerian simulations, using cell sizes smaller than the bubble diameter can result in physically irrelevant results. Therefore, various levels of mesh refinement were tested, as detailed in Table 8.1, which summarizes the layer thickness and total number of cells for each refinement scenario.

Table 8.1: Features of the selected mesh sensitivity cases.

Mesh features	Mesh 1	Mesh 2	Mesh 3	Mesh 4
Layer size [µm]	100	120	200	240
Number of cells [-]	2.3E6	2E6	1E6	7.5E5

Figure 8.3 shows the results for gas volume fraction (VF) and vertical velocity across the four mesh sensitivity cases. "Mesh 2" was ultimately chosen as it provided sufficient accuracy.

The results demonstrate that thinner layers at the electrode result in higher local gas volume fractions and consequently greater velocities. The two halves of the cell, the cathodic side on the left and the anodic side on the right, are distinctly separated by the diaphragm in the center. As specified in the simulations, both the gas vertical velocity and VF are zero within the diaphragm region. Mesh details of the full cell are displayed in Figure 8.4.

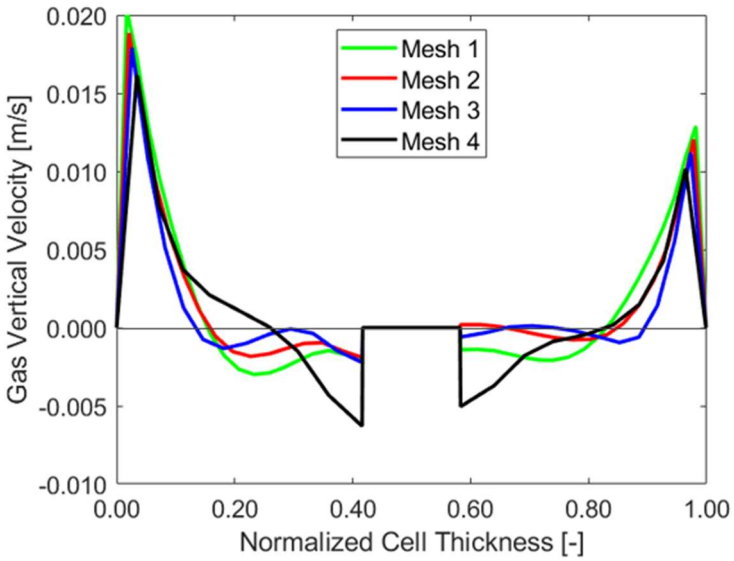

(a)

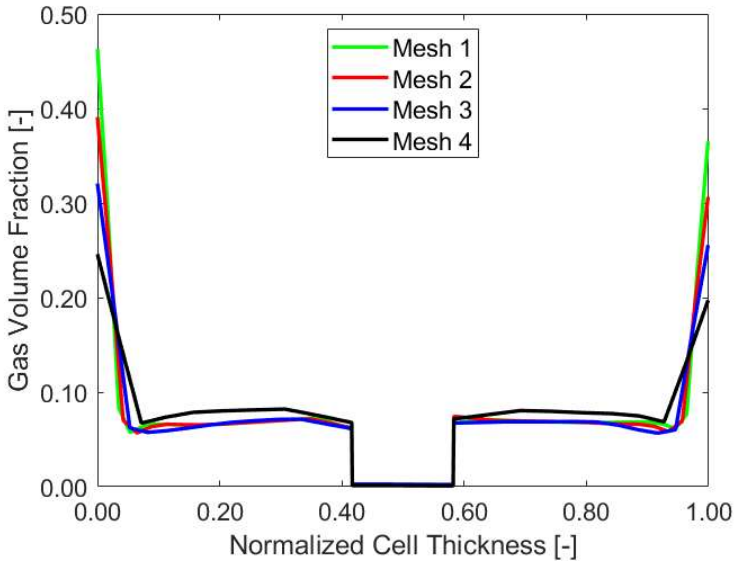

(b)

Figure 8.3: Mesh sensitivity analysis: **(a)** gas vertical velocity and **(b)** *VF* along the cell thickness.

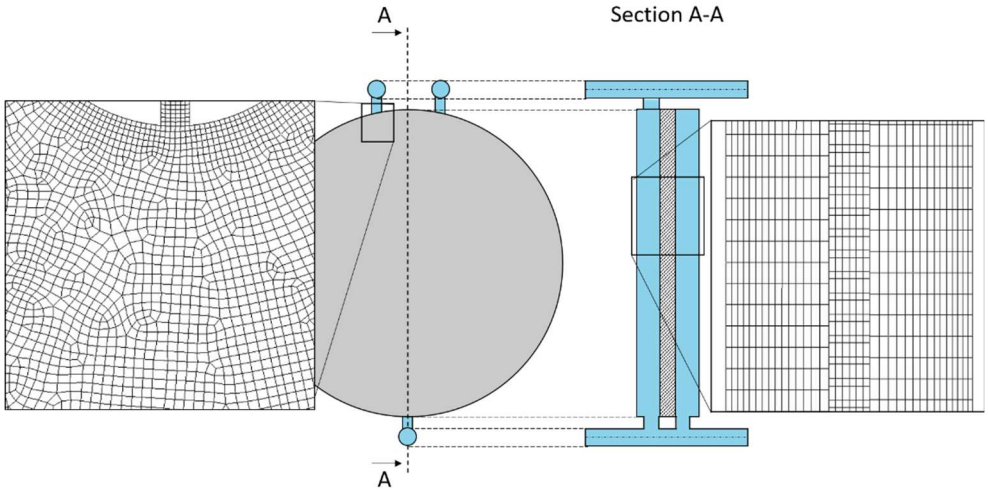

Figure 8.4: 50-kW EZ cell mesh details.

8.3 Modeling hypotheses

The following assumptions were made for the multi-physics modeling:

- The inlet temperature and operating pressure were set to 52 °C and 9 bar, respectively, to reflect real application conditions. A boundary condition of 70 °C was applied at the inlet for the channels above the cell to simulate the heated electrolyte and gas entering from preceding cells.
- The primary phase was modeled as a 20 wt% NaOH solution in water, while the secondary phase comprised a mixture of hydrogen and oxygen gases. This gas mixture was chosen to enable two-phase modeling in ANSYS Fluent. By calibrating boundary conditions, the model ensured that hydrogen was generated exclusively in the cathodic chamber and oxygen in the anodic chamber.
- The flow within the cell was assumed to be laminar due to the low velocities involved, with a calculated Reynolds number (Re) of less than 1000.
- The hydrogen bubble diameter was set to a constant value of 20 µm, derived from empirical equations that correlate bubble size with working pressure (ranging from 1 to 200 bar) as presented in Eq. 3.5 and 2.50 [83]. While the calculated average bubble diameters were approximately 15 µm for hydrogen and 22 µm for oxygen, a uniform bubble size of 20 µm was chosen for the gas mixture.
- Bubble coalescence and breakage were neglected due to the high current densities involved, compared to the laboratory test-case cell, for the reasons explained in Section 3.1.3.
- The same forces described in Section 5.2.1 were employed for the model.
- Surface tension was taken as 60 mN/m, corresponding to water's surface tension at the specified pressure and temperature.
- Turbulent dispersion force was not considered, due to the laminar conditions of the flow.
- The electrochemical model was integrated in the numerical setup by applying the hydrogen evolution reaction of Eq. 1.1 at the cathode and the oxygen evolution reaction of Eq. 1.2 at the anode. Furthermore, the current density Eq. 3.10 was imposed at the electrodes to further refine the modeling and include the bubble coverage effect.
- The thermal model presented in Section 2.4, was included in the modeling, making use of the heat sources described in Section 3.4.

8.3.1 Boundary conditions

Regarding the boundary conditions, they were tailored to capture the distinct fluid-dynamic and thermal behaviors of the cells under various configurations.

The inlet mass flow rates were calculated individually for the three selected cells in the simulated stack to maintain a coherent electrolyte flow within the cell and channels. To accurately represent realistic operating conditions, gas volume fraction was prescribed at the inlets of the top channels for the 1st and 58th cells, simulating the fraction of hydrogen or oxygen carried over from preceding cells in the stack.

Outlet pressures were meticulously calibrated to ensure the desired flow rates and maintain operational stability across the cells. More specifically, calibration was conducted by monitoring the outlet mass flow rates and gas volume fractions.

No-slip boundary conditions were applied to the walls of both the cathode and anode compartments, ensuring that the liquid and gas phases adhered to the surfaces. For the diaphragm, a zero-gas-velocity condition was imposed, effectively modeling its semi-permeable nature and restricting gas flow through this component.

In the no-diaphragm configuration, the absence of the diaphragm was accounted for by imposing separate no-slip wall conditions for each half-cell.

8.4 Results

8.4.1 Full-cell and separate half-cells geometry comparison

The multi-physics model was applied to the central cell of the stack, specifically the 58th cell, as it represents the average behavior of the stack. The initial analysis evaluated the significance of incorporating the diaphragm within the cell geometry, focusing on its impact on the temperature distribution. Scenarios with and without the diaphragm were compared, with results visualized in Figure 8.5 (a) and (b), showing temperature contours on the vertical transversal YZ plane for the cell's central section, as defined in Figure 8.1. These contours reveal that the anodic cell temperature on the left is higher than the cathodic cell temperature on the right, corroborated by the data in Figure 8.6. This disparity is primarily due to the differences in specific heat capacities: oxygen (~1000 J/kg K) and hydrogen (~14,000 J/kg K) compared to the electrolyte (~3300 J/kg K). Consequently, temperature increases more in the anodic half-cell than in the cathodic one.

The inclusion of the diaphragm was shown to promote a more uniform temperature distribution across the cell. Maximum temperatures at the anode reached 353 K without the diaphragm, compared to 343 K with it. Gas volume

fraction analysis further highlighted the diaphragm's role, as excluding it led to higher gas accumulation, particularly visible in Figure 8.5 (c) and (d). This variation arises from minor gas intrusion into the diaphragm, especially in the cathodic half-cell, where hydrogen's higher permeability results in around 1% hydrogen impurity in oxygen, according to industrial observations. Oxygen, being less permeable, has reduced intrusion into the cathodic chamber. As a result, gas stagnation is higher in the no-diaphragm configuration, contributing to the elevated temperatures.

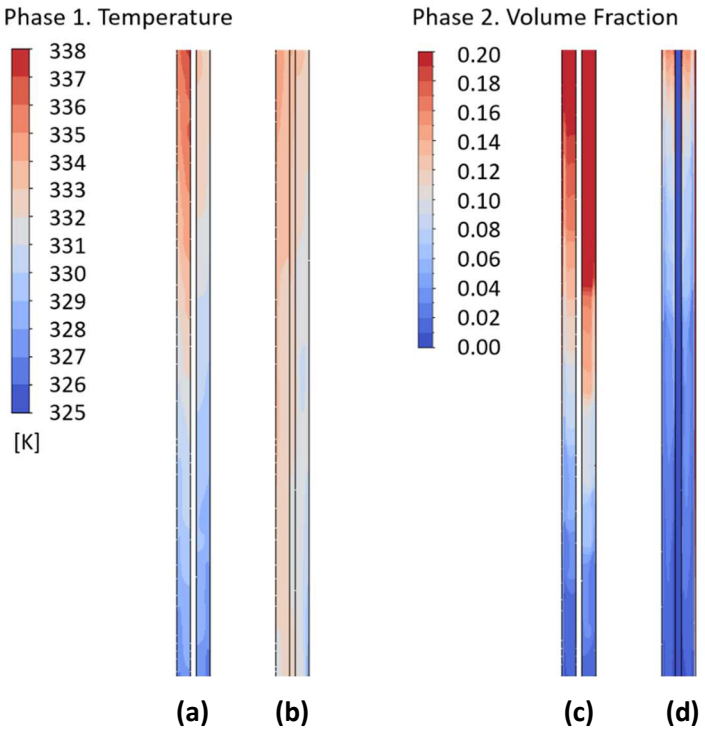

Figure 8.5: Temperature contours, **(a)** without and **(b)** with diaphragm, and *VF* contours, **(c)** without and **(d)** with diaphragm, in 58th cell YZ mid-section.

Temperature and vertical velocity trends for both phases, with and without the diaphragm, are detailed in Figure 8.6, Figure 8.7 and Figure 8.8, respectively referring to a quarter, half and three-quarters cell height YZ mid-sections of the central cell. For the liquid phase, higher temperatures were observed with the diaphragm configuration in the lower section of the cell, as visible in Figure 8.6. For the gas phase, the diaphragm case exhibited sharper temperature increases, indicating its impact on both phases. At the cell's midpoint, Figure 8.7 highlights higher temperatures for both phases than those at the bottom, with an average

increase of 7 K above the inlet electrolyte temperature of 325.15 K. At the top, overall temperatures rose further, reflecting heat accumulation as fluids ascended. Here, the diaphragm configuration maintained higher temperatures in the cathodic chamber, while the anodic half-cell was 3 K warmer in the no-diaphragm case, as clear from Figure 8.8.

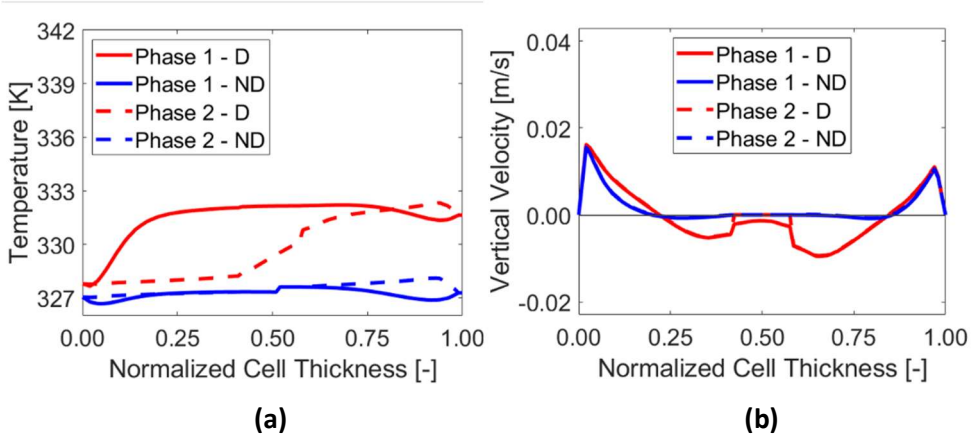

Figure 8.6: **(a)** Temperature and **(b)** vertical velocity trends inside the central cell, with (D) and without (ND) diaphragm for the two phases evaluated at a quarter cell height YZ mid-section.

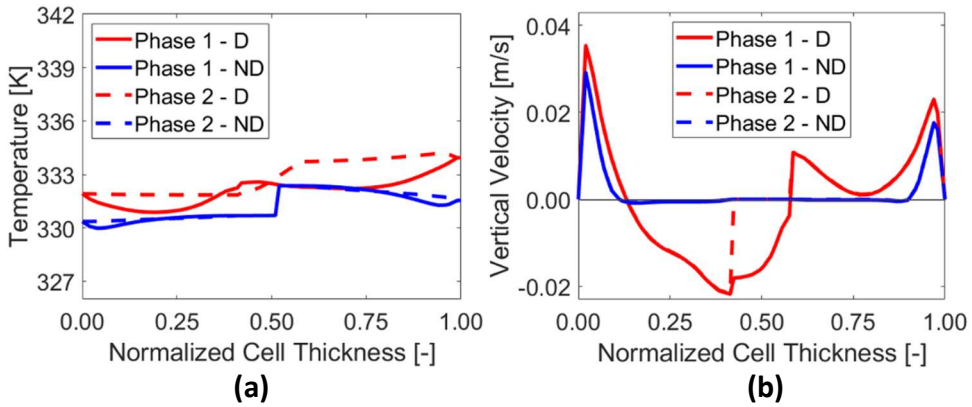

Figure 8.7: **(a)** Temperature and **(b)** vertical velocity trends inside the central cell, with (D) and without (ND) diaphragm for the two phases evaluated at half cell height YZ mid-section.

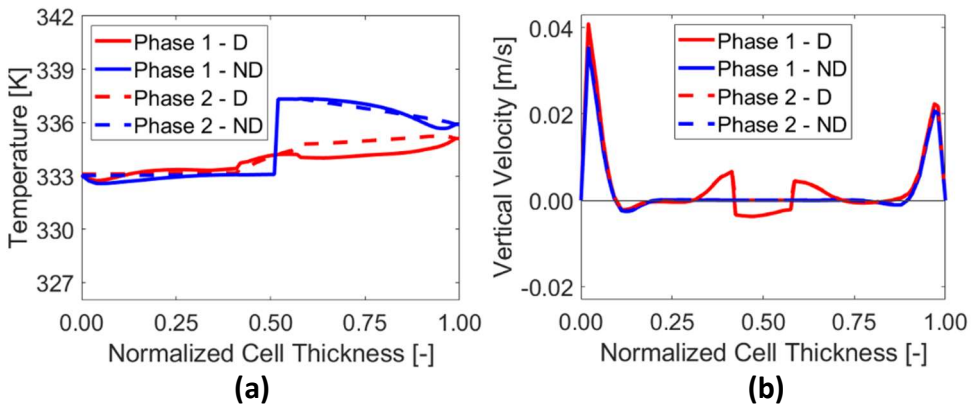

Figure 8.8: **(a)** Temperature and **(b)** vertical velocity trends inside the central cell, with (D) and without (ND) diaphragm for the two phases evaluated at three-quarters cell height YZ mid-section.

Vertical velocity patterns, as reported in Figure 8.6 (b), Figure 8.7 (b) and Figure 8.8 (b), revealed enhanced recirculation for the diaphragm case, with pronounced downward velocity peaks promoting mixing and temperature uniformity, as evident from Figure 8.6 (a), Figure 8.7 (a) and Figure 8.8 (a). These results underscore the physical accuracy of full-cell modeling over isolated half-cell simulations, particularly for thermal analysis. Consequently, subsequent results incorporate the diaphragm component.

8.4.2 Fluid-dynamic and thermal analyses along the stack

The nominal conditions of the first, central, and last cells in the stack were modeled by applying the CFD framework to such cells. The results in terms of gas volume fractions at the anode and cathode for the first, central and last cell are presented respectively in Figure 8.9, Figure 8.10 and Figure 8.11. Average gas volume fractions, summarized in Table 8.2, show a consistent ~30% higher gas volume fraction at the cathode compared to the anode across all cells. This is due to hydrogen's lower density and higher buoyancy compared to oxygen, despite higher oxygen molar flows at the anode per Faraday's law. The increased buoyancy near the cathode enhances recirculation and gas accumulation at the top, potentially creating hotspots and material damage risks.

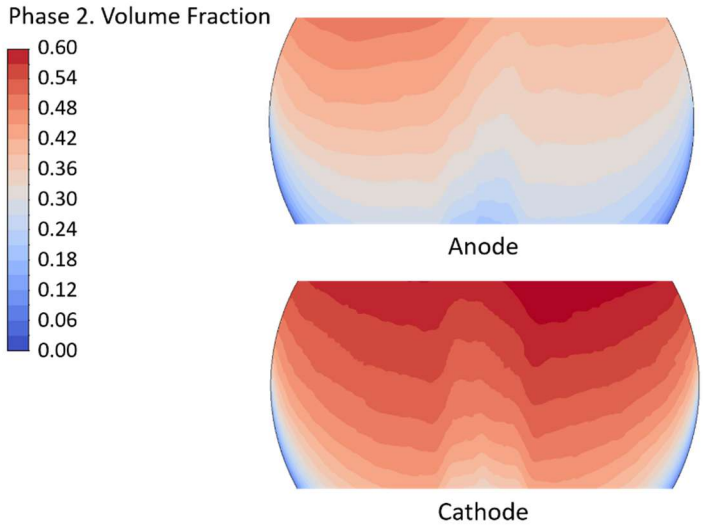

Figure 8.9: First cell anode and cathode gas *VF*.

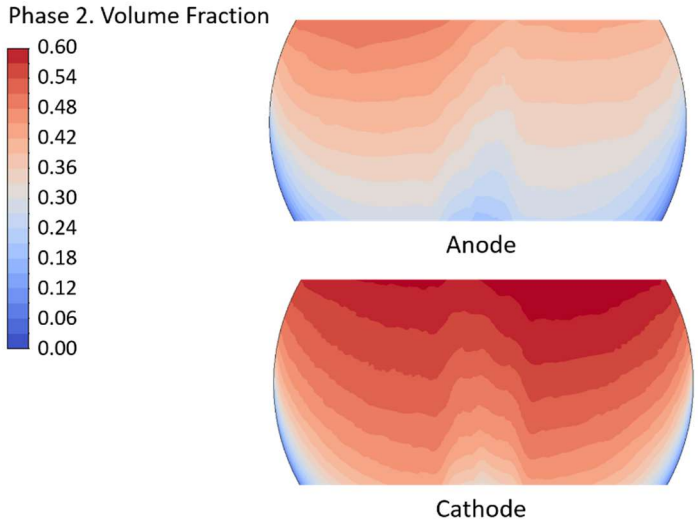

Figure 8.10: Central cell anode and cathode gas *VF*.

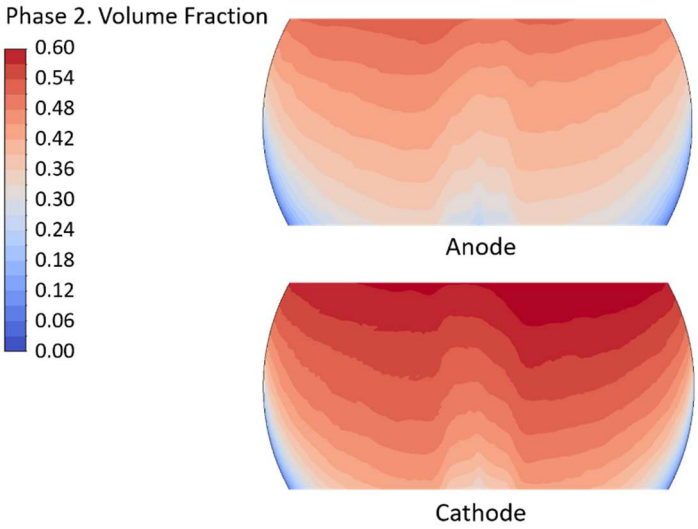

Figure 8.11: Last cell anode and cathode gas *VF*.

Table 8.2: Average gas *VF* values at the electrodes for the different cells.

Variables	1st cell	58th cell	115th cell
Average gas *VF* at the anode [-]	0.34	0.34	0.39
Average gas *VF* at the cathode [-]	0.48	0.48	0.48

To understand the reason behind the gas volume fraction difference between cathodic and anodic half-cells, several factors must be considered. First, hydrogen's lower density compared to oxygen results in greater buoyancy forces and velocities in the cathodic cell, even though the total molar flow, based on Faraday's law, is higher for oxygen at the anode. This is consistent with the elevated velocities near the cathode observed in Figure 8.6 (b), Figure 8.7 (b) and Figure 8.8 (b). These higher velocities enhance recirculation as the flow reaches the cell top, generating vorticity. The simulations reveal greater downward velocities in the cathodic half-cell compared to the anodic one, particularly evident in Figure 8.7 (b). This vorticity and recirculation lead to a higher gas volume fraction at the cathode, as the gas faces greater difficulty escaping compared to the anodic chamber, where velocities and recirculation are more moderate.

The gas volume fraction also varies slightly between the first and central cells. This variation can be attributed to electrolyte flow dynamics. Simulations show minimal electrolyte flow through the central cell, likely due to a weaker Venturi effect compared to the first cell, where more electrolyte flows through the top channels. In contrast, the last cell has a distinct geometry with a single inlet and two half-cell outlets, resulting in different flow dynamics that directly influence the gas volume fraction distribution.

A more detailed examination of the gas volume fraction trends along a central line at the anode and cathode, presented in Figure 8.12 (a), shows that the first and central cells exhibit similar behavior. In Figure 8.12 (b), the normalized current density trend is shown, aligning with the gas volume fraction trends as described by Eq. 3.10, which accounts for the impact of bubble coverage. Higher values of VF correspond to lower values of current density and vice versa. Notably, while the cathode gas volume fraction pattern in the last cell closely resembles that of the other two cells, a significant divergence is observed at the anode. This difference is attributed to the distinct flow dynamics at the half-cell inlets for each case.

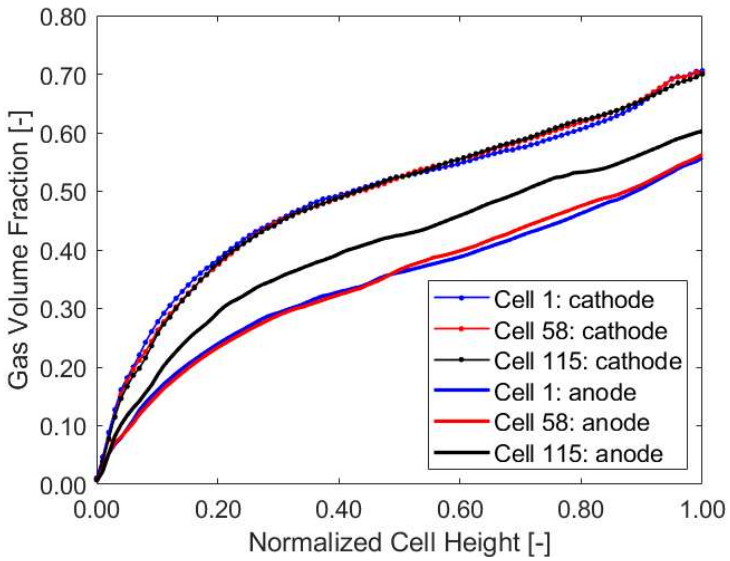

(a)

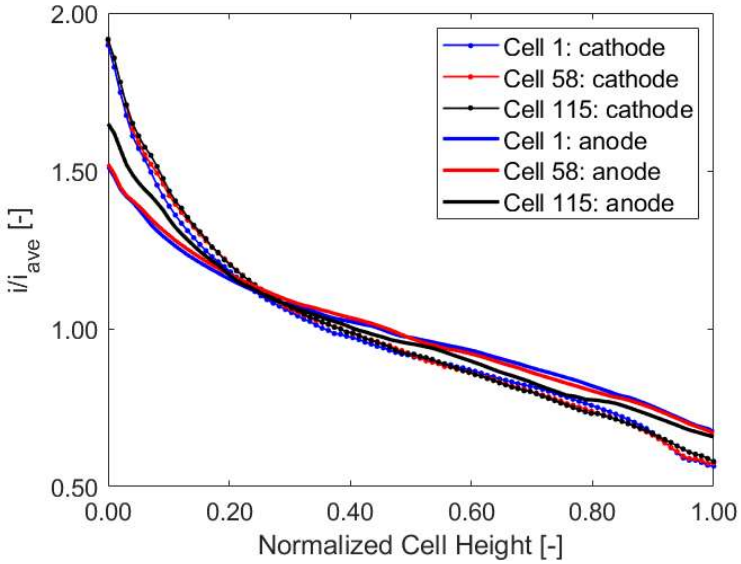

(b)

Figure 8.12: Anode and cathode **(a)** gas *VF* and **(b)** relative current density for first, central and last cell.

Figure 8.13 presents the liquid vertical velocity contours for the three cells on the vertical transversal YZ plane in the central section of the cell, as defined in Figure 8.1. The contours highlight an asymmetrical flow entry into the anodic chamber in the 1st and 58th cells, in contrast to the more balanced flow observed in the 115th cell. This asymmetry in the first and central cells results from their open inlet channels, where liquid motion is predominantly driven by buoyancy forces due to the generated gas. In comparison, the last cell's geometry, with a sealed inlet channel, directs the flow more effectively into the anodic chamber, resulting in higher flow rates. This design difference significantly influences the fluid and gas distribution, particularly at the anode, and is regarded as the primary factor behind the variation in anodic gas volume fraction among the cells.

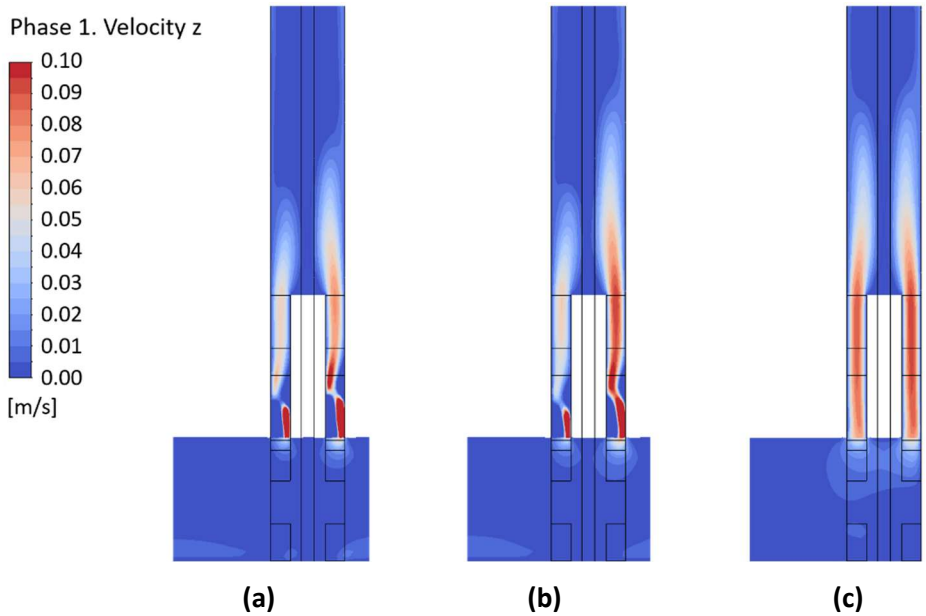

Figure 8.13: Liquid vertical velocity contour in the low part of the cell: first **(a)**, central **(b)**, and last **(c)** cell, taken at YZ mid-section.

Focusing on the thermal analysis, the contours in Figure 8.14, Figure 8.15 and Figure 8.16 show the average temperature distribution for the anode and cathode, respectively for the first, central and last cell, on a plane parallel to the XZ plane, as defined in Figure 8.1. Corresponding average and maximum temperature values are provided in Figure 8.17. Despite the application of identical heating sources across all three cases and both electrodes, the anode consistently exhibits higher temperatures on average, with even greater values observed in the first cells. This temperature disparity is likely due to the velocity non-uniformity discussed in Figure 8.13: reduced fluid flow leads to lower velocities, resulting in localized heating and higher temperatures. Notably, the maximum temperature in the first cell is approximately 15 °C higher than expected, with distinct hot spots forming at the cell edges where flow stagnation occurs. Maximum values are higher at the cathode than at the anode and this appears to go against what has already been said. However, this anomaly is strictly linked to the higher gas volume fraction at the cathode, since gas accumulation leads to local peaks of temperature, in specific areas of the electrode which are not visible in the displayed regions.

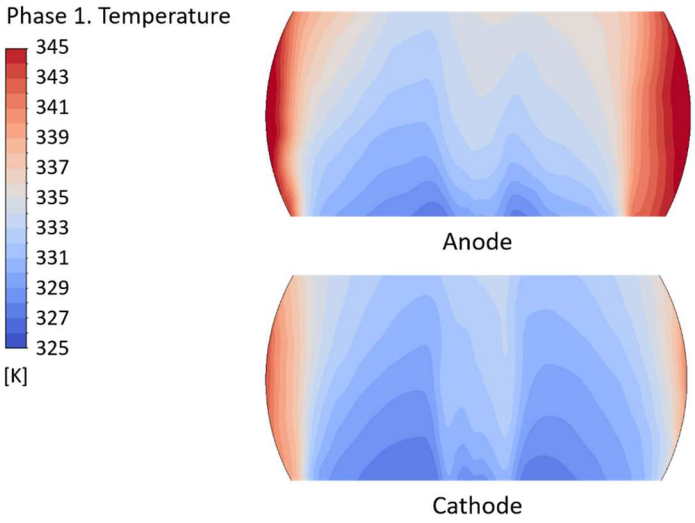

Figure 8.14: First cell anode and cathode temperature.

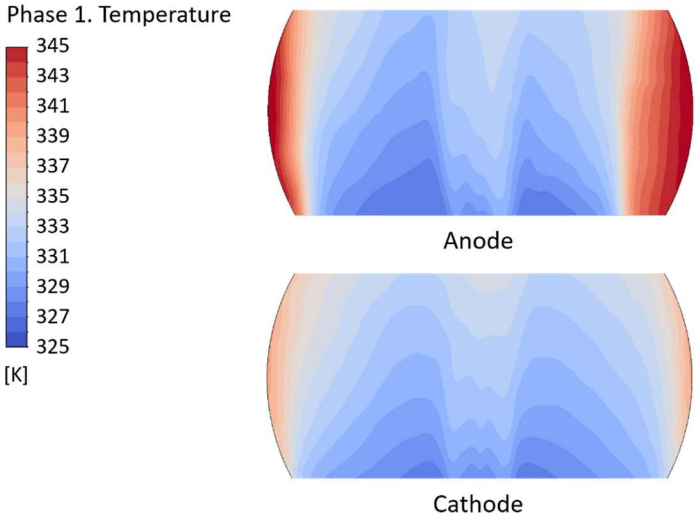

Figure 8.15: Central cell anode and cathode temperature.

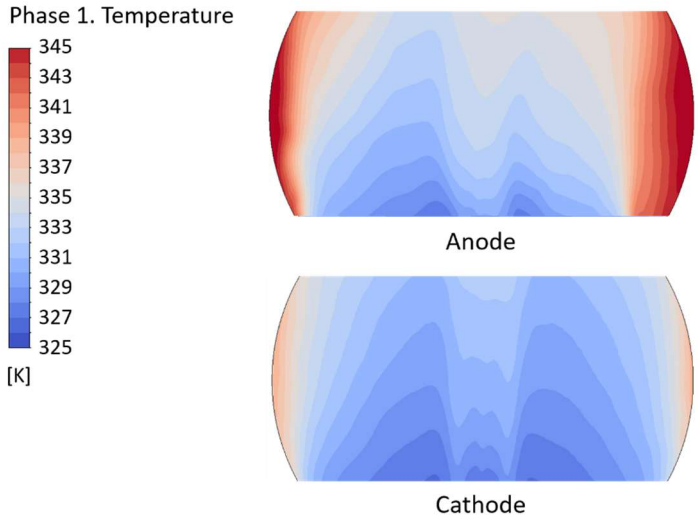

Figure 8.16: Last cell anode and cathode temperature.

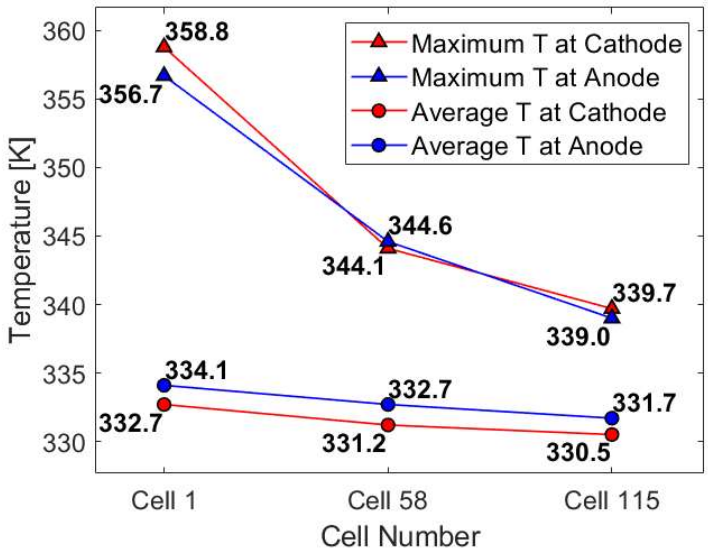

Figure 8.17: Average and maximum temperature values at the electrodes for the different cells.

The chart in Figure 8.18 depicts the temperature profile along a central line on the electrodes, reaffirming the higher average temperatures observed at the anode. Comparing this to earlier findings, it can be concluded that reduced velocities at the entrance of the half-cells contribute to elevated electrode

temperatures. This temperature trend aligns with the chart in Figure 8.12 (b), where higher current densities in the lower part of the cell were identified, correlating with localized increases in heating.

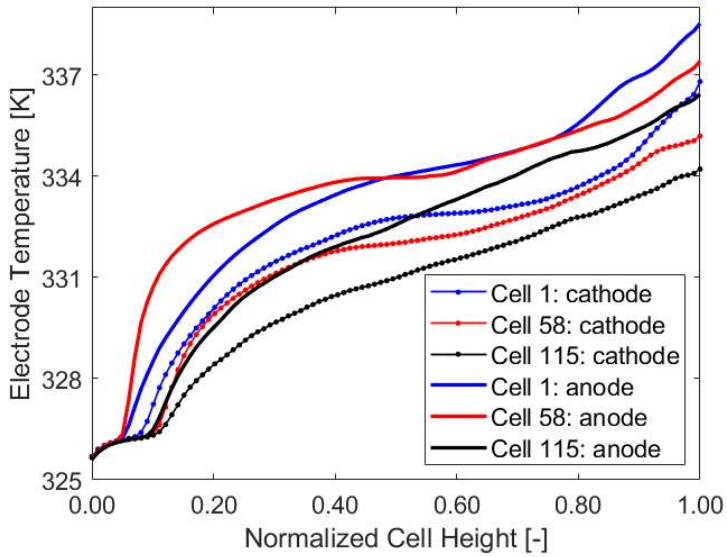

Figure 8.18: Anode and cathode temperature for first, central and last cell.

The charts in Figure 8.19, Figure 8.20 and Figure 8.21 illustrate the electrolyte temperature and vertical velocity trends respectively referring to a quarter, half and three-quarters cell height YZ mid-sections of the central cell. Lower temperature values for the 115th cell are evident from the charts Figure 8.19 (a), Figure 8.20 (a) and Figure 8.21 (a), indicating that these reduced temperatures are not limited to the electrodes, as shown in Figure 8.18, but extend across the entire cell domain. This behavior can be attributed to the lower maximum velocities and reduced recirculation observed in the last cell, as displayed in charts Figure 8.19 (b), Figure 8.20 (b) and Figure 8.21 (b), which hinder effective thermal mixing. Enhanced recirculation is particularly notable in the cathodic half-cell of the 58th cell, as shown in Figure 8.20 (b), and to a lesser extent in Figure 8.19 (b). The simulations underscore how varying boundary conditions across cells influence flow distribution within the half-cells, impacting overall electrolyte movement and contributing to variability in vertical velocity trends. The temperature at the bottom of the 58th cell is significantly higher than in the other cells, as can be observed in Figure 8.19 (a), likely due to the pronounced recirculation in this region.

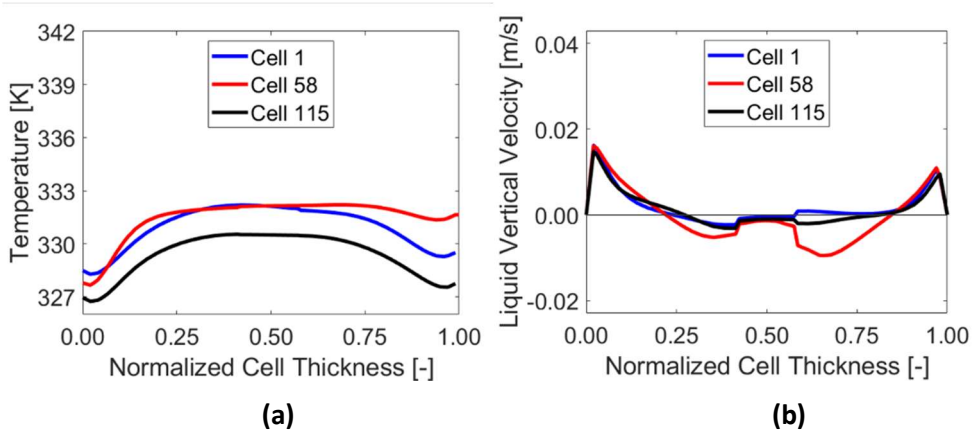

(a) **(b)**

Figure 8.19: Electrolyte **(a)** temperature **(b)** and vertical velocity trends inside the cell for 1st, 58th and 115th cells evaluated at a quarter cell height YZ mid-section.

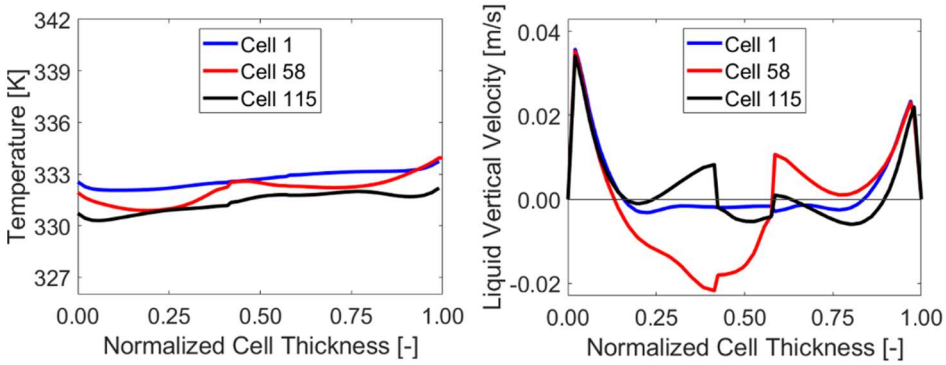

(a) **(b)**

Figure 8.20: Electrolyte **(a)** temperature **(b)** and vertical velocity trends inside the cell for 1st, 58th and 115th cells evaluated at half cell height YZ mid-section.

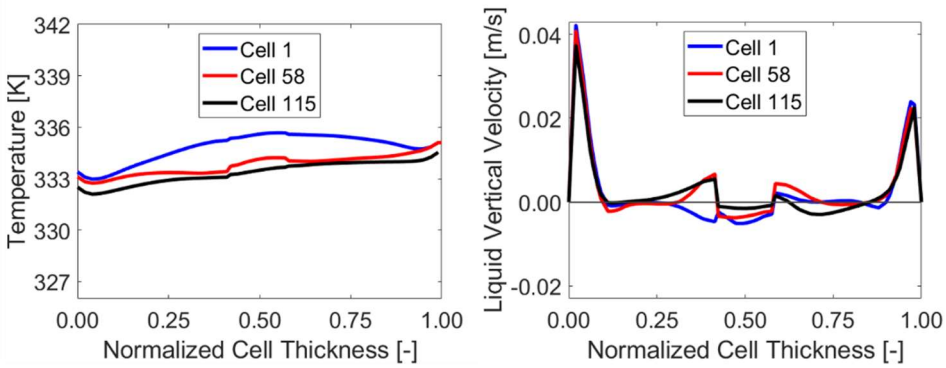

(a) **(b)**

Figure 8.21: Electrolyte **(a)** temperature **(b)** and vertical velocity trends inside the cell for 1st, 58th and 115th cells evaluated at three-quarters cell height YZ mid-section.

The significant difference in peak temperature between the last cell and the other cells can also be attributed to the influence of the top channel temperature. In the simulation, a top channel temperature of 343.15 K (70 °C) was applied to cells 1 and 58, reflecting the anticipated heat generation from the preceding cells, as discussed in Section 8.3. However, when the top channel temperature was adjusted to 325.15 K (52 °C), representing the expected inlet temperature at startup, the maximum temperature values decreased. This effect is illustrated in Figure 8.22, which shows the temperature trends for the anode and cathode of the central cell.

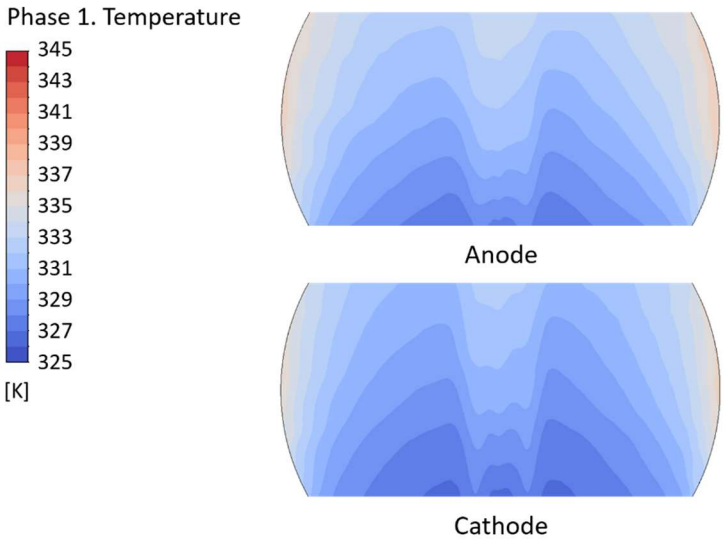

Figure 8.22: Central cell anode and cathode temperature contours: start-up conditions.

The results presented can be interpreted by considering that even a small amount of top flow reaching the cell can lead to a temperature increase in areas where stagnation occurs. During start-up, if this undesired recirculation does not take place, the maximum temperature values for both the anode and cathode are approximately 337 K (64 °C). This scenario highlights once again that hot spots form at the sides of the cell, where fluid velocity is lower. In this case, the temperature values are more similar to those of the 115th cell, in contrast to the significant variations observed across cells in Figure 8.17.

Figure 8.23 displays the temperature trend for both electrodes during the start-up phase, comparing it to the operating case. During start-up, temperatures are on average 3 K lower for the anode and 1.5 K lower for the cathode. Additionally, the temperature increase is more gradual and linear with cell height during start-up, in contrast to the trend observed under operating conditions.

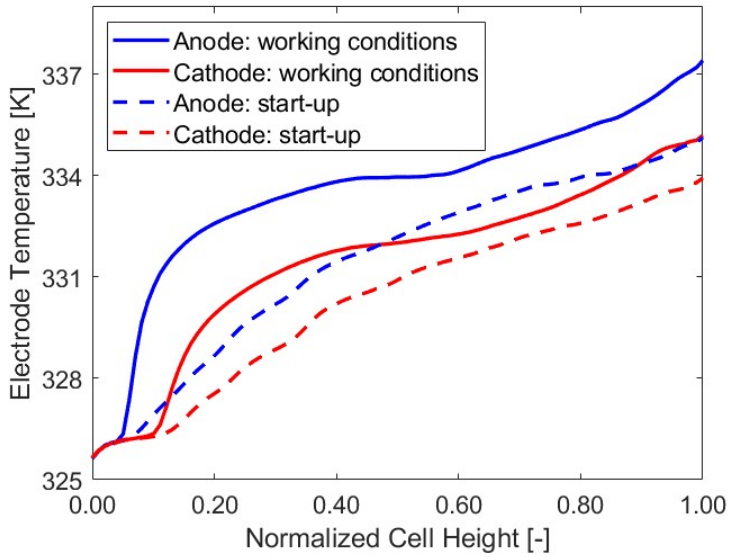

Figure 8.23: Anode and cathode temperature for the central cell at start-up and during operation.

8.5 Discussion

A high-fidelity, multi-physics CFD model for alkaline water electrolyzers was developed, addressing key limitations in existing literature and offering valuable insights into the main variables of interest. The model integrates two-phase flow, electrochemical reactions, and thermal dynamics, including Joule and Faraday heating, allowing for realistic simulations. By incorporating a full-cell geometry with a diaphragm, it overcomes the simplifications commonly found in previous studies, which often ignore geometric and multi-physics complexities.

The model's calibration of boundary conditions enabled accurate simulations of individual cells within a stack, accounting for variations in pressure and mass flows and tailoring conditions to each specific cell. The inclusion of the diaphragm further enhanced the accuracy of thermal predictions by promoting

more uniform temperature distribution. Comparisons between cases with and without the diaphragm revealed that omitting the diaphragm led to higher localized heating, with a maximum temperature difference of 10 K. Additionally, more gas accumulation was observed in the non-diaphragm case, as indicated by the gas volume fraction, confirming the diaphragm's crucial role in ensuring realistic simulations. Higher recirculation, observed when the diaphragm was included, facilitated more uniform temperature distribution by enhancing mixing and reducing thermal gradients within the cell.

Simulations of the first, central, and last cells of the stack demonstrated significant differences in gas volume fractions and thermal behavior. The cathode exhibited a higher average gas volume fraction compared to the anode, with a consistent value of 0.48 across all cathodes. The disparity in gas volume fraction between the cathode and anode can be attributed to the different densities of hydrogen and oxygen, which lead to distinct flow patterns. At the anode, variations in gas volume fraction among cells were observed: the first and central cells had a value of 0.34, while the last cell had a value of 0.39, due to differing flow channelling into the last cell. Vertical velocity analysis showed variable fluid-dynamic patterns in the lower regions of the cells.

Thermal analysis revealed that the anode temperatures were consistently higher than those at the cathode across all cases. Two possible explanations were identified: first, the specific heats of the two gases differ at working temperatures and pressures, with hydrogen at the cathode being less susceptible to temperature increases; second, velocity non-uniformities in the half-cells indicated that slower flows are generally linked to higher temperatures. Hot spots, especially in areas of electrolyte stagnation, were more pronounced, with maximum temperatures at the anode of the first cell being 15 K higher than the expected outlet temperature of 343.15 K. Thermal differences among cells were primarily influenced by top channel effects. Simulations under start-up conditions (with top channel temperatures set at 325.15 K) showed an average reduction of 3 K at the anode and 1.5 K at the cathode compared to operating conditions.

The primary limitation of the simulations described is the lack of direct validation, due to the unavailability of data and confidentiality concerns. As previously mentioned, the CFD modeling framework developed for this study is based on the validated test-case cell model from Chapter 5, with the necessary modifications. However, the use of this 3D multi-physics model lays the groundwork for investigating more advanced configurations and provides insight into the interaction between fluid-dynamic, thermal and electrochemical variables, representing a total novelty to the literature.

CONCLUSIONS

This PhD thesis advances the understanding of alkaline electrolyzers through comprehensive computational fluid dynamics (CFD) modeling, integrating multi-physics approaches to optimize cell performance and address industrial challenges. Alkaline water electrolysis, a key technology for green hydrogen production, requires continuous improvement in design, efficiency, and scalability to meet the growing demand for renewable energy storage and industrial applications. On the hand, mature, multi-physics CFD models are missing from the literature.

To bridge the literature gap, Fluent software program was employed, making use of the Eulerian two-phase model, and the methodology assessed and calibrated based on the available studies on the topic. The novel multi-physics approach was tailored on the specific case cell at hand, accounting for thermal or turbulent analyses where needed. To achieve grid independence during the meshing phase, a new-to-the-literature expression was developed, determining the minimum required first-layer thickness at the electrode.

Making use of the literature test-case for validation, three different gas introduction approaches at the electrodes were evaluated, i.e. a volumetric source, a mass-flow inlet condition and via electrochemical reactions. The volumetric source method demonstrated better alignment with experiments, likely due to better gas dispersion compared to direct gas introduction at the wall. However, electrochemical-driven gas introduction, being more representative of real conditions, was later applied to the actual cell geometries.

The model application to the real-scale electrolyzer cells gave some important and novel results. Findings revealed that higher mass flow rates generally reduce gas volume fraction and gas accumulation, preventing also hot spots. Higher current densities are linked to increased gas volume fraction at the electrode, but they also encourage gas dispersion within the cell. Conversely, at lower hydrogen production rates, gas remains closer to the electrode, limiting diffusion. The model application confirmed that gas production and velocity are greater at the bottom of the cell when the variable current density function is applied.

New performance parameters were employed to assess the fluid-dynamic efficiency of a cell with the conclusion that average gas volume fraction at the

electrode is the best choice, for conducting a geometry optimization. The ratio between electrode and outlet average gas volume fraction, on the other hand, is a more suitable indicator at lower current densities, in which case lower mass flow rates are preferable.

Finally, by applying the complete multi-physics model to a full-cell geometry, it was consistently observed that the anode temperatures were higher than those of the cathode. It was also noticed how the flow entering the cell influences the thermal behavior of the cells.

By introducing the current density function we can have a more precise overview of the gas accumulation effect on the gas production, to assess how the fluid-dynamic variables are affected. No direct efficiency law, based on gas VF at the electrode, was elaborated by the present research work, which mostly shows how the physical parameters characterizing the cell mutually influence each other. Anyway, speaking about the electrolyzer performance, the main thing to consider is whether there are some critical areas due to gas accumulation, which is strictly linked to the gas VF variable, which can be studied applying CFD simulations to the cell geometry. In the literature few studies deal with how gas accumulation affects the damage of the device. Based on such lack of information, the present study does not have a quantitative characterization of the risk related to gas accumulation. On the other hand, the close collaboration with the industrial partner practically gave us the idea on how cell damage occurs more often in areas of elevated gas presence.

The presented multi-physics modeling approach aims at being as comprehensive as possible and it represents a first step towards future advanced CFD modeling and a novelty to the literature. Each area of investigation can be further refined by using more precise equations and accounting for the interactions between the various physical phenomena involved. Specifically, critical areas for future improvement of the present model include the following points: the introduction of a precise population balance model to account for different bubble sizes; the inclusion of a turbulent dispersion model; considering the thermal effect of nearby cells and environment. Also, transient simulations could be considered to analyze dynamic operational scenarios.

In order to have a modeling approach as precise as possible, experimental setups and results of real-scale electrolyzers, under operational conditions, are needed for the calibration and validation of the model.

REFERENCES

[1] Hreiz, R., Abdelouahed, L., Fünfschilling, D., and Lapicque, F., 2015, "Electrogenerated Bubbles Induced Convection in Narrow Vertical Cells: PIV Measurements and Euler–Lagrange CFD Simulation," Chemical Engineering Science, **134**, pp. 138–152. https://doi.org/10.1016/j.ces.2015.04.041.

[2] Wisniak, J., 2002, "Svante Arrhenius and the Greenhouse Effect," IJCT Vol.09(2) [March 2002]. [Online]. Available: http://nopr.niscpr.res.in/handle/123456789/18880. [Accessed: 15-Dec-2024].

[3] "The Paris Agreement, 2015." [Online]. Available: https://unfccc.int/process-and-meetings/the-paris-agreement. [Accessed: 15-Dec-2024].

[4] Ould Amrouche, S., Rekioua, D., Rekioua, T., and Bacha, S., 2016, "Overview of Energy Storage in Renewable Energy Systems," International Journal of Hydrogen Energy, **41**(45), pp. 20914–20927. https://doi.org/10.1016/j.ijhydene.2016.06.243.

[5] Schill, W.-P., 2020, "Electricity Storage and the Renewable Energy Transition," Joule, **4**(10), pp. 2059–2064. https://doi.org/10.1016/j.joule.2020.07.022.

[6] Mayyas, A., Wei, M., and Levis, G., 2020, "Hydrogen as a Long-Term, Large-Scale Energy Storage Solution When Coupled with Renewable Energy Sources or Grids with Dynamic Electricity Pricing Schemes," International Journal of Hydrogen Energy, **45**(33), pp. 16311–16325. https://doi.org/10.1016/j.ijhydene.2020.04.163.

[7] Modisha, P., and Bessarabov, D., 2023, "Aromatic Liquid Organic Hydrogen Carriers for Hydrogen Storage and Release," Current Opinion in Green and Sustainable Chemistry, **42**, p. 100820. https://doi.org/10.1016/j.cogsc.2023.100820.

[8] Andújar, J. M., Segura, F., Rey, J., and Vivas, F. J., 2022, "Batteries and Hydrogen Storage: Technical Analysis and Commercial Revision to Select the Best Option," Energies, **15**(17), p. 6196. https://doi.org/10.3390/en15176196.

[9] Benghanem, M., Almohamadi, H., Haddad, S., Mellit, A., and Chettibi, N., 2024, "The Effect of Voltage and Electrode Types on Hydrogen Production Powered by Photovoltaic System Using Alkaline and PEM Electrolyzers,"

International Journal of Hydrogen Energy, **57**, pp. 625–636. https://doi.org/10.1016/j.ijhydene.2023.12.232.
[10] "IEA, The Future of Hydrogen, 2019." [Online]. Available: https://www.iea.org/reports/the-future-of-hydrogen. [Accessed: 15-Dec-2024].
[11] "IEA (2023) Report IEA: CO2 Emissions in 2022." [Online]. Available: https://www.iea.org/reports/co2-emissions-in-2022.
[12] "Global Hydrogen Review, 2022." [Online]. Available: https://iea.blob.core.windows.net/assets/c5bc75b1-9e4d-460d-9056-6e8e626a11c4/GlobalHydrogenReview2022.pdf. [Accessed: 15-Dec-2024].
[13] 2021, "Net Zero By 2050." [Online]. Available: https://iea.blob.core.windows.net/assets/deebef5d-0c34-4539-9d0c-10b13d840027/NetZeroby2050-ARoadmapfortheGlobalEnergySector_CORR.pdf. [Accessed: 15-Dec-2024].
[14] "Global Hydrogen Review, 2024." [Online]. Available: https://iea.blob.core.windows.net/assets/89c1e382-dc59-46ca-aa47-9f7d41531ab5/GlobalHydrogenReview2024.pdf. [Accessed: 15-Dec-2024].
[15] "IRENA (2021), Making the Breakthrough: Green Hydrogen Policies and Technology Costs, International Renewable Energy Agency, Abu Dhabi." [Online]. Available: https://www.irena.org/-/media/Files/IRENA/Agency/Publication/2020/Nov/IRENA_Green_Hydrogen_breakthrough_2021.pdf. [Accessed: 15-Dec-2024].
[16] Sharma, A., and Arya, S. K., 2017, "Hydrogen from Algal Biomass: A Review of Production Process," Biotechnology Reports, **15**, pp. 63–69. https://doi.org/10.1016/j.btre.2017.06.001.
[17] Song, H., Yang, G., Xue, P., Li, Y., Zou, J., Wang, S., Yang, H., and Chen, H., 2022, "Recent Development of Biomass Gasification for H2 Rich Gas Production," Applications in Energy and Combustion Science, **10**, p. 100059. https://doi.org/10.1016/j.jaecs.2022.100059.
[18] Song, H., Luo, S., Huang, H., Deng, B., and Ye, J., 2022, "Solar-Driven Hydrogen Production: Recent Advances, Challenges, and Future Perspectives," ACS Energy Lett., **7**(3), pp. 1043–1065. https://doi.org/10.1021/acsenergylett.1c02591.
[19] Steinfeld, A., 2005, "Solar Thermochemical Production of Hydrogen—a Review," Solar Energy, **78**(5), pp. 603–615. https://doi.org/10.1016/j.solener.2003.12.012.
[20] Oudejans, D., Offidani, M., Constantinou, A., Albonetti, S., Dimitratos, N., and Bansode, A., 2022, "A Comprehensive Review on Two-Step

Thermochemical Water Splitting for Hydrogen Production in a Redox Cycle," Energies, **15**(9), p. 3044. https://doi.org/10.3390/en15093044.

[21] David, M., Ocampo-Martínez, C., and Sánchez-Peña, R., 2019, "Advances in Alkaline Water Electrolyzers: A Review," Journal of Energy Storage, **23**, pp. 392–403. https://doi.org/10.1016/j.est.2019.03.001.

[22] Chatenet, M., G. Pollet, B., R. Dekel, D., Dionigi, F., Deseure, J., Millet, P., D. Braatz, R., Z. Bazant, M., Eikerling, M., Staffell, I., Balcombe, P., Shao-Horn, Y., and Schäfer, H., 2022, "Water Electrolysis: From Textbook Knowledge to the Latest Scientific Strategies and Industrial Developments," Chemical Society Reviews, **51**(11), pp. 4583–4762. https://doi.org/10.1039/D0CS01079K.

[23] Henkensmeier, D., Cho, W.-C., Jannasch, P., Stojadinovic, J., Li, Q., Aili, D., and Jensen, J. O., 2024, "Separators and Membranes for Advanced Alkaline Water Electrolysis," Chem. Rev., **124**(10), pp. 6393–6443. https://doi.org/10.1021/acs.chemrev.3c00694.

[24] El-Shafie, M., 2023, "Hydrogen Production by Water Electrolysis Technologies: A Review," Results in Engineering, **20**, p. 101426. https://doi.org/10.1016/j.rineng.2023.101426.

[25] Santos, A. L., Cebola, M.-J., and Santos, D. M. F., 2021, "Towards the Hydrogen Economy—A Review of the Parameters That Influence the Efficiency of Alkaline Water Electrolyzers," Energies, **14**(11), p. 3193. https://doi.org/10.3390/en14113193.

[26] Akyüz, E. S., Telli, E., and Farsak, M., 2024, "Hydrogen Generation Electrolyzers: Paving the Way for Sustainable Energy," International Journal of Hydrogen Energy, **81**, pp. 1338–1362. https://doi.org/10.1016/j.ijhydene.2024.07.175.

[27] Rodríguez, J., and Amores, E., 2020, "CFD Modeling and Experimental Validation of an Alkaline Water Electrolysis Cell for Hydrogen Production," Processes, **8**(12), p. 1634. https://doi.org/10.3390/pr8121634.

[28] Wang, T., Wang, J., Wang, P., Wang, F., Liu, L., and Guo, H., 2023, "Non-Uniform Liquid Flow Distribution in an Alkaline Water Electrolyzer with Concave-Convex Bipolar Plate (CCBP): A Numerical Study," International Journal of Hydrogen Energy, **48**(33), pp. 12200–12214. https://doi.org/10.1016/j.ijhydene.2022.12.203.

[29] Rykær Kraglund, M., Carmo, M., Schiller, G., Asif Ansar, S., Aili, D., Christensen, E., and Oluf Jensen, J., 2019, "Ion-Solvating Membranes as a New Approach towards High Rate Alkaline Electrolyzers," Energy & Environmental Science, **12**(11), pp. 3313–3318. https://doi.org/10.1039/C9EE00832B.

[30] Chen, Y., and Li, S., 2024, “Super-Stable Ionic Solvation Membrane: A New Opportunity for Alkaline Water Electrolysis,” TIMS, **2**(2), pp. 100063–2. https://doi.org/10.59717/j.xinn-mater.2024.100063.

[31] Du, N., Roy, C., Peach, R., Turnbull, M., Thiele, S., and Bock, C., 2022, “Anion-Exchange Membrane Water Electrolyzers,” Chem. Rev., **122**(13), pp. 11830–11895. https://doi.org/10.1021/acs.chemrev.1c00854.

[32] Brauns, J., and Turek, T., 2020, “Alkaline Water Electrolysis Powered by Renewable Energy: A Review,” Processes, **8**(2), p. 248. https://doi.org/10.3390/pr8020248.

[33] Poole, C. F., 2020, “Chapter 1 - Milestones in the Development of Liquid-Phase Extraction Techniques,” *Liquid-Phase Extraction*, C.F. Poole, ed., Elsevier, pp. 1–44. https://doi.org/10.1016/B978-0-12-816911-7.00001-3.

[34] Nagai, N., Takeuchi, M., Kimura, T., and Oka, T., 2003, “Existence of Optimum Space between Electrodes on Hydrogen Production by Water Electrolysis,” International Journal of Hydrogen Energy, **28**(1), pp. 35–41. https://doi.org/10.1016/S0360-3199(02)00027-7.

[35] Ulleberg, Ø., 2003, “Modeling of Advanced Alkaline Electrolyzers: A System Simulation Approach,” International Journal of Hydrogen Energy, **28**(1), pp. 21–33. https://doi.org/10.1016/S0360-3199(02)00033-2.

[36] Angulo, A., Linde, P. van der, Gardeniers, H., Modestino, M., and Rivas, D. F., 2020, “Influence of Bubbles on the Energy Conversion Efficiency of Electrochemical Reactors,” Joule, **4**(3), pp. 555–579. https://doi.org/10.1016/j.joule.2020.01.005.

[37] Zarghami, A., Deen, N. G., and Vreman, A. W., 2020, “CFD Modeling of Multiphase Flow in an Alkaline Water Electrolyzer,” Chemical Engineering Science, **227**, p. 115926. https://doi.org/10.1016/j.ces.2020.115926.

[38] Gao, L.-Y., Yang, L., Wang, C.-H., Shan, G.-X., Huo, X.-Y., Zhang, M.-F., Li, W., and Zhang, J.-L., “Three-Dimensional Two-Phase CFD Simulation of Alkaline Electrolyzers.” [Online]. Available: https://jelectrochem.xmu.edu.cn/journal/vol29/iss9/3. [Accessed: 31-Oct-2024].

[39] Rajora, A., and Haverkort, J. W., 2023, “An Analytical Model for the Velocity and Gas Fraction Profiles near Gas-Evolving Electrodes,” International Journal of Hydrogen Energy, **48**(71), pp. 27450–27463. https://doi.org/10.1016/j.ijhydene.2023.03.154.

[40] Aldas, K., Pehlivanoglu, N., and Mat, M. D., 2008, “Numerical and Experimental Investigation of Two-Phase Flow in an Electrochemical Cell,” International Journal of Hydrogen Energy, **33**(14), pp. 3668–3675. https://doi.org/10.1016/j.ijhydene.2008.04.047.

[41] Muhsen, H., Alshawabkeh, M., Al-Mahmodi, M., Ghanem, A., and Al-Halhouli, A., 2024, "Sensitivity Analysis of Electrodes Spacing Media for Evaluating Alkaline Electrolyzer Performance through CFD Modeling," Renewable Energy Focus, **49**, p. 100575. https://doi.org/10.1016/j.ref.2024.100575.

[42] Norazahar, N., Khan, F., Rahmani, N., and Ahmad, A., 2024, "Degradation Modelling and Reliability Analysis of PEM Electrolyzer," International Journal of Hydrogen Energy, **50**, pp. 842–856. https://doi.org/10.1016/j.ijhydene.2023.07.153.

[43] Le Bideau, D., Chocron, O., Mandin, P., Kiener, P., Benbouzid, M., Sellier, M., Kim, M., Ganci, F., and Inguanta, R., 2020, "Evolutionary Design Optimization of an Alkaline Water Electrolysis Cell for Hydrogen Production," Applied Sciences, **10**(23), p. 8425. https://doi.org/10.3390/app10238425.

[44] Abdelouahed, L., Hreiz, R., Poncin, S., Valentin, G., and Lapicque, F., 2014, "Hydrodynamics of Gas Bubbles in the Gap of Lantern Blade Electrodes without Forced Flow of Electrolyte: Experiments and CFD Modelling," Chemical Engineering Science, **111**, pp. 255–265. https://doi.org/10.1016/j.ces.2014.01.028.

[45] El-Askary, W. A., Sakr, I. M., Ibrahim, K. A., and Balabel, A., 2015, "Hydrodynamics Characteristics of Hydrogen Evolution Process through Electrolysis: Numerical and Experimental Studies," Energy, **90**, pp. 722–737. https://doi.org/10.1016/j.energy.2015.07.108.

[46] Mat, M. D., Aldas, K., and Ilegbusi, O. J., 2004, "A Two-Phase Flow Model for Hydrogen Evolution in an Electrochemical Cell," International Journal of Hydrogen Energy, **29**(10), pp. 1015–1023. https://doi.org/10.1016/j.ijhydene.2003.11.007.

[47] Mandin, P., Hamburger, J., Bessou, S., and Picard, G., 2005, "Modelling and Calculation of the Current Density Distribution Evolution at Vertical Gas-Evolving Electrodes," Electrochimica Acta, **51**(6), pp. 1140–1156. https://doi.org/10.1016/j.electacta.2005.06.007.

[48] Xue, L., Song, S., Chen, W., Liu, B., and Wang, X., 2024, "Enhancing Efficiency in Alkaline Electrolysis Cells: Optimizing Flow Channels through Multiphase Computational Fluid Dynamics Modeling," Energies, **17**(2), p. 448. https://doi.org/10.3390/en17020448.

[49] Lee, J., Alam, A., and Ju, H., 2021, "Multidimensional and Transient Modeling of an Alkaline Water Electrolysis Cell," International Journal of Hydrogen Energy, **46**(26), pp. 13678–13690. https://doi.org/10.1016/j.ijhydene.2020.10.133.

[50] Alam, A., Park, C., Lee, J., and Ju, H., 2020, “Comparative Analysis of Performance of Alkaline Water Electrolyzer by Using Porous Separator and Ion-Solvating Polybenzimidazole Membrane,” Renewable Energy, **166**, pp. 222–233. https://doi.org/10.1016/j.renene.2020.11.151.

[51] Hawkes, G., O’Brien, J., Stoots, C., and Hawkes, B., 2009, “3D CFD Model of a Multi-Cell High-Temperature Electrolysis Stack,” International Journal of Hydrogen Energy, **34**(9), pp. 4189–4197. https://doi.org/10.1016/j.ijhydene.2008.11.068.

[52] Olesen, A. C., Frensch, S. H., and Kær, S. K., 2019, “Towards Uniformly Distributed Heat, Mass and Charge: A Flow Field Design Study for High Pressure and High Current Density Operation of PEM Electrolysis Cells,” Electrochimica Acta, **293**, pp. 476–495. https://doi.org/10.1016/j.electacta.2018.10.008.

[53] Muthiah, M., Elnashar, M., Afzal, W., and Tan, H., 2024, “Safety Assessment of Hydrogen Production Using Alkaline Water Electrolysis,” International Journal of Hydrogen Energy, **84**, pp. 803–821. https://doi.org/10.1016/j.ijhydene.2024.08.237.

[54] Haoran, C., Xia, Y., Wei, W., Yongzhi, Z., Bo, Z., and Leiqi, Z., 2024, “Safety and Efficiency Problems of Hydrogen Production from Alkaline Water Electrolyzers Driven by Renewable Energy Sources,” International Journal of Hydrogen Energy, **54**, pp. 700–712. https://doi.org/10.1016/j.ijhydene.2023.08.324.

[55] Muzychka, Y. S., and Awad, M. M., 2010, “Asymptotic Generalizations of the Lockhart–Martinelli Method for Two Phase Flows,” J. Fluids Eng, **132**(3). https://doi.org/10.1115/1.4001157.

[56] Ishii, M., 1977, *One-Dimensional Drift-Flux Model and Constitutive Equations for Relative Motion between Phases in Various Two-Phase Flow Regimes*, ANL-77-47, Argonne National Lab., Ill. (USA). https://doi.org/10.2172/6871478.

[57] Dahlkild, A. A., 2001, “Modelling the Two-Phase Flow and Current Distribution along a Vertical Gas-Evolving Electrode,” Journal of Fluid Mechanics, **428**, pp. 249–272. https://doi.org/10.1017/S0022112000002639.

[58] Wedin, R., and Dahlkild, A. A., 2001, “On the Transport of Small Bubbles under Developing Channel Flow in a Buoyant Gas-Evolving Electrochemical Cell,” Ind. Eng. Chem. Res., **40**(23), pp. 5228–5233. https://doi.org/10.1021/ie001073u.

[59] Schillings, J., Doche, O., and Deseure, J., 2015, “Modeling of Electrochemically Generated Bubbly Flow under Buoyancy-Driven and

Forced Convection," International Journal of Heat and Mass Transfer, **85**, pp. 292–299. https://doi.org/10.1016/j.ijheatmasstransfer.2015.01.121.

[60] "ANSYS Fluent Theory Guide, 2021." [Online]. Available: https://dl.cfdexperts.net/cfd_resources/Ansys_Documentation/Fluent/Ansys_Fluent_Theory_Guide. pdf. [Accessed: 15-Dec-2024].

[61] Garcia-Navarro, J. C., Schulze, M., and Friedrich, K. A., 2019, "Detecting and Modeling Oxygen Bubble Evolution and Detachment in Proton Exchange Membrane Water Electrolyzers," International Journal of Hydrogen Energy, **44**(50), pp. 27190–27203. https://doi.org/10.1016/j.ijhydene.2019.08.253.

[62] Ipek, N., Vynnycky, M., and Cornell, A., 2008, "A Coupled Electrochemical and Hydrodynamical Two-Phase Model for the Electrolytic Pickling of Steel," J. Electrochem. Soc., **155**(4), p. P33. https://doi.org/10.1149/1.2835224.

[63] Boissonneau, P., and Byrne, P., 2000, "An Experimental Investigation of Bubble-Induced Free Convection in a Small Electrochemical Cell," Journal of Applied Electrochemistry, **30**(7), pp. 767–775. https://doi.org/10.1023/A:1004034807331.

[64] Ramirez Gonzalez, L., 2018, "2050: Power-to-Hydrogen Opportunities for Far Offshore Wind Farms." [Online]. Available: https://repository.tudelft.nl/islandora/object/uuid%3Ad10f16e7-d7d3-4b0b-96e5-8cf12c226125. [Accessed: 20-Sep-2022].

[65] Gibson, M., and Launder, B., 1978, "Ground Effects on Pressure Fluctuations in the Atmospheric Boundary Layer," Journal of Fluid Mechanics, **86**, pp. 491–511. https://doi.org/10.1017/S0022112078001251.

[66] Grahn, A., Krepper, E., Alt, S., and Kästner, W., 2008, "Implementation of a Strainer Model for Calculating the Pressure Drop across Beds of Compressible, Fibrous Materials," Nuclear Engineering and Design, **238**(10), pp. 2546–2553. https://doi.org/10.1016/j.nucengdes.2008.04.010.

[67] LeRoy, R. L., Bowen, C. T., and LeRoy, D. J., 1980, "The Thermodynamics of Aqueous Water Electrolysis," J. Electrochem. Soc., **127**(9), p. 1954. https://doi.org/10.1149/1.2130044.

[68] Hammoudi, M., Henao, C., Agbossou, K., Dubé, Y., and Doumbia, M. L., 2012, "New Multi-Physics Approach for Modelling and Design of Alkaline Electrolyzers," International Journal of Hydrogen Energy, **37**(19), pp. 13895–13913. https://doi.org/10.1016/j.ijhydene.2012.07.015.

[69] Zeng, K., and Zhang, D., 2010, "Recent Progress in Alkaline Water Electrolysis for Hydrogen Production and Applications," Progress in Energy and Combustion Science, **36**(3), pp. 307–326. https://doi.org/10.1016/j.pecs.2009.11.002.

[70] Cho, K. M., Deshmukh, P. R., and Shin, W. G., 2021, “Hydrodynamic Behavior of Bubbles at Gas-Evolving Electrode in Ultrasonic Field during Water Electrolysis,” Ultrasonics Sonochemistry, **80**, p. 105796. https://doi.org/10.1016/j.ultsonch.2021.105796.

[71] Vogt, H., 2012, “The Actual Current Density of Gas-Evolving Electrodes—Notes on the Bubble Coverage,” Electrochimica Acta, **78**, pp. 183–187. https://doi.org/10.1016/j.electacta.2012.05.124.

[72] Hine, F., and Murakami, K., 1980, “Bubble Effects on the Solution IR Drop in a Vertical Electrolyzer Under Free and Forced Convection,” J. Electrochem. Soc., **127**(2), p. 292. https://doi.org/10.1149/1.2129658.

[73] Prentice, G., 2003, “Electrochemical Engineering,” *Encyclopedia of Physical Science and Technology*, Academic Press Cambridge, pp. 143–159. [Online]. Available: https://www.academia.edu/download/36277948/encyclopedia_of_physical_science_and_technology_-_chemical_engineering.pdf#page=236. [Accessed: 26-Nov-2024].

[74] Shen, M., Bennett, N., Ding, Y., and Scott, K., 2011, “A Concise Model for Evaluating Water Electrolysis,” International Journal of Hydrogen Energy, **36**(22), pp. 14335–14341. https://doi.org/10.1016/j.ijhydene.2010.12.029.

[75] Diéguez, P. M., Ursúa, A., Sanchis, P., Sopena, C., Guelbenzu, E., and Gandía, L. M., 2008, “Thermal Performance of a Commercial Alkaline Water Electrolyzer: Experimental Study and Mathematical Modeling,” International Journal of Hydrogen Energy, **33**(24), pp. 7338–7354. https://doi.org/10.1016/j.ijhydene.2008.09.051.

[76] Onda, K., Kyakuno, T., Hattori, K., and Ito, K., 2004, “Prediction of Production Power for High-Pressure Hydrogen by High-Pressure Water Electrolysis,” Journal of Power Sources, **132**(1), pp. 64–70. https://doi.org/10.1016/j.jpowsour.2004.01.046.

[77] Marini, S., Salvi, P., Nelli, P., Pesenti, R., Villa, M., Berrettoni, M., Zangari, G., and Kiros, Y., 2012, “Advanced Alkaline Water Electrolysis,” Electrochimica Acta, **82**, pp. 384–391. https://doi.org/10.1016/j.electacta.2012.05.011.

[78] Sakas, G., Ibáñez-Rioja, A., Ruuskanen, V., Kosonen, A., Ahola, J., and Bergmann, O., 2022, “Dynamic Energy and Mass Balance Model for an Industrial Alkaline Water Electrolyzer Plant Process,” International Journal of Hydrogen Energy, **47**(7), pp. 4328–4345. https://doi.org/10.1016/j.ijhydene.2021.11.126.

[79] Khan, I., Wang, M., Zhang, Y., Tian, W., Su, G., and Qiu, S., 2020, “Two-Phase Bubbly Flow Simulation Using CFD Method: A Review of Models for

Interfacial Forces," Progress in Nuclear Energy, **125**, p. 103360. https://doi.org/10.1016/j.pnucene.2020.103360.

[80] Antal, S. P., Lahey, R. T., and Flaherty, J. E., 1991, "Analysis of Phase Distribution in Fully Developed Laminar Bubbly Two-Phase Flow," International Journal of Multiphase Flow, **17**(5), pp. 635–652. https://doi.org/10.1016/0301-9322(91)90029-3.

[81] Haug, P., Kreitz, B., Koj, M., and Turek, T., 2017, "Process Modelling of an Alkaline Water Electrolyzer," International Journal of Hydrogen Energy, **42**(24), pp. 15689–15707. https://doi.org/10.1016/j.ijhydene.2017.05.031.

[82] Mei, X. (梅笑寒), Yuan, S. (袁述), Zhao, C. (赵聪凡), Yan, X. (闫晓辉), Zhao, C. (赵长颖), and Wang, Q. (王倩), 2023, "Measuring Three-Dimensional Bubble Dynamics for Hydrogen Production via Water Electrolysis," Physics of Fluids, **35**(12), p. 123338. https://doi.org/10.1063/5.0173622.

[83] Frey, F., 2016, "Experimental Set-Up for Bubble Behaviour in a High Pressure Alkaline Electrolyte," Master Thesis, Karlsruhe Institute of Technology, Karlsruhe, Germany.

[84] Liu, L., Cai, W., Chen, Y., and Wang, Y., 2018, "Fluid Dynamics and Mass Transfer Study of Electrochemical Oxidation by CFD Prediction and Experimental Validation," Ind. Eng. Chem. Res., **57**(18), pp. 6493–6504. https://doi.org/10.1021/acs.iecr.7b04226.

[85] Picardi, R., Zhao, L., and Battaglia, F., 2016, "On the Ideal Grid Resolution for Two-Dimensional Eulerian Modeling of Gas–Liquid Flows," Journal of Fluids Engineering, **138**(114503). https://doi.org/10.1115/1.4033561.